Lawrence Berkeley Laboratory
UNIVERSITY OF CALIFORNIA

APPLIED SCIENCE DIVISION

Submitted to Science

DISTRIBUTION OF AIRBORNE ^{222}RADON CONCENTRATIONS IN U.S. HOMES

A.V. Nero, M.B. Schwehr, W.W. Nazaroff, and K.L. Revzan

November 1984

APPLIED SCIENCE DIVISION

Prepared for the U.S. Department of Energy under Contract DE-AC03-76SF00098

DISCLAIMER

Submitted to Science.

LBL 18274
EEB-Vent 84-33

DISTRIBUTION OF AIRBORNE ^{222}RADON CONCENTRATIONS IN U.S. HOMES

A.V. Nero, M.B. Schwehr, W.W. Nazaroff, and K.L. Revzan

Building Ventilation and Indoor Air Quality Program
Lawrence Berkeley Laboratory
University of California
Berkeley, California 94720

November 1984

This work was supported by the Director, Office of Energy Research, Office of Health and Environmental Research, Human Health and Assessments Division and Pollutant Characterization and Safety Research Division, and by the Assistant Secretary for Conservation and Renewable Energy, Office of Building Energy Research and Development, Building Systems Division, of the U.S. Department of Energy under Contract No. DE-AC03-76SF00098.

DISTRIBUTION OF AIRBORNE ^{222}RADON CONCENTRATIONS IN U.S. HOMES

A.V. Nero, M.B. Schwehr, W.W. Nazaroff, and K.L. Revzan

ABSTRACT

We have developed a frequency distribution of ^{222}Rn concentrations in U.S. single-family homes by systematically appraising available data using lognormal representations and explicitly considering differences in selection of homes and season of measurements. Results are quite robust, showing a dependence on the specific aggregation approach that is modest and consistent with expectations. Considering the resulting distributions, as well as identifiable sampling uncertainties, the distribution of annual-average ^{222}Rn concentrations in single-family residences can be characterized by a geometric mean of 0.9 $\pm$ 0.1 pCi/l (34$\pm$ 4 Bq/m^3) and a geometric standard deviation of 2.8 $\pm$ 0.2. It appears that concentrations in approximately one million U.S. homes exceed 8 pCi/l, which - for long term occupants - corresponds to an added individual lifetime risk of lung cancer of about 2%.

Author note: A.V. Nero, M.B. Schwehr, and K.L. Revzan are members of the Building Ventilation and Indoor Air Quality Program in the Applied Science Division of Lawrence Berkeley Laboratory, University of California, Berkeley, California 94720. W.W. Nazaroff, until recently in this program, is now in the Department of Environmental Engineering Sciences, California Institute of Technology, Pasadena, California 91125.

Radon 222 and its decay products (or "daughters") are universally present in the air we breathe, typically reaching higher levels indoors than out. Risk estimates based primarily on epidemiology among uranium miners suggest that concentrations in ordinary houses cause thousands of lung cancer cases per year among the U.S. population. A special concern has been the frequent appearance of homes with concentrations an order of magnitude greater than average, implying individual risks of lung cancer exceeding 1%. These risks are very large compared with ordinarily considered environmental risks and have led to diverse studies characterizing indoor concentrations, the factors affecting them, and health implications.[1,2]

The U.S. effort, however, has not directly provided representative information on residential concentrations, largely because relevant studies have varied markedly in scientific objectives, selection of homes, and measurement techniques. Thus the U.S. National Council on Radiation Protection and Measurements (NCRP) could not estimate the number of U.S. homes exceeding its newly recommended remedial action level for ^{222}Rn-daughter exposures, noting only that a postulated average exposure rate of 0.2 WLM[3] per year (suggested by certain U.S. studies) and a geometric standard deviation of 2.5 (based on a large Canadian study) implied that 0.14% of homes exceeded the recommended limit of 2 WLM/yr.[4] However, data from U.S. studies have grown to be substantial. We present here the results of a systematic appraisal of these data, designed to aggregate them in a consistent way - explicitly accounting for their differences - and

thereby to provide a frequency distribution of concentrations in U.S. homes and an estimate of its uncertainties. We also review briefly the factors giving rise to this distribution and note associated risk and regulatory implications.

Scope and origin of the U.S. data

From the literature and from direct communication with researchers, we have accumulated data from 38 U.S. areas (typically urban centers or states), as summarized in Table 1. In few, if any, of the studies were homes selected using statistically-based sampling procedures. On the other hand, virtually all selection processes contained a strong random element, whether by asking for volunteers (e.g., from among employees of a given institution), by selecting from participants in an energy conservation program, or by other means. The data sets - representing 21 of the 48 contiguous states - therefore serve as useful indicators of the distribution in specific geographic areas, and in aggregate can be expected to display the distribution in a substantial subset of U.S. residences.

Two broad incentives give rise to most of these data: sets 23 to 38 were collected because some prior indication suggested the probability of high ^{222}Rn concentrations. In contrast, most of the first 22 sets are from studies ascertaining present concentrations merely as a basis for estimating potential increases due to energy-conserving measures that reduce air infiltration into houses. For none of the data sets in Table 1 is it thought that use of ^{226}Ra-bearing industrial residues or incorporation of unusually effective

infiltration-reduction measures have contributed significantly to ^{222}Rn concentrations.

The studies varied substantially in size: of the 38 sets, 8 have 50 or more homes and an equal number have fewer than 10. Our confidence in utilizing small data sets is bolstered substantially by an awareness that - almost uniformly - the results of measurements in large housing samples yield concentrations that are distributed approximately lognormally. This is demonstrated in Figure 1, where the distribution obtained by directly aggregating data from 19 sets conforms very well to a lognormal distribution. This agreement is expected on fundamental grounds if indoor concentrations are largely determined by factors that are essentially multiplicative, such as radium content and permeability of the soil, understructure type or house tightness, and local temperatures and winds. Applicability of lognormal representations provides us, not only with a means for aggregating data in a systematic way, but also with a framework within which to effectively parameterize even small data sets. For each data set, Table 1 states lognormal characteristics - the geometric mean (GM) and standard deviation (GSD) - either calculated from individual data as part of the present analysis or taken from the original papers. The results of each study are expressed in terms of ^{222}Rn concentration, even for the studies where daughter concentration was measured.[5] GMs range from 0.35 (San Francisco) to 5.7 pCi/l (Fargo), with GSDs ranging from 1.3 to 4. The average concentration (i.e., arithmetic mean) is significantly greater than the GM (e.g., by 52% for a GSD of 2.5) and is the appropriate parameter in considering the population dose.

As indicated in Table 1, measurements were performed using a variety of measurement techniques, raising questions about consistency in overall calibration and about the importance of statistical uncertainty associated with individual measurements. Based on results of interlaboratory calibration efforts of the last several years[6], potential inconsistencies in calibration are likely to be very small compared with the differences in GM seen in Table 1. The effect of statistical uncertainties on our aggregate parameters is noted below.

Table 1 does not include all data sets accumulated in the United States: for a few we were not able to acquire the data; several sets appear unsuitable for present purposes; and we may be unaware of some sets. Moreover, some studies are not unambiguously represented in the literature, e.g., with data represented piecemeal or in contradictory fashion in various reports; for these we have relied on what appears to be the primary reference. Despite several missing or ambiguous sets, Table 1 is a good approximation to a complete representation of results on single-family residences, and - taken together - the data constitute a large and significant body of information on indoor ^{222}Rn concentrations in the United States.

Normalizing and Aggregating the data

Utilizing these data sets is complicated by differences in integrating time and season of measurements. For the purpose of exposure (and risk) assessment, an integrated year-long measurement is

ideal (and practical with track-etched monitors measuring ^{222}Rn concentration[7]). Only a few data sets approach the ideal, but many effectively approximate it by deploying integrating ^{222}Rn or daughter monitors during every season. It is the large number of studies that employed integrated samplers for only one or two seasons that require the most careful consideration.

In four studies of which we are aware, ^{222}Rn measurements have been made in a sample of homes during part of the heating season and again during the summer. Winter concentrations and annual averages (estimated as the average of winter and summer results for each house) are approximately lognormally distributed, with parameters summarized in Table 2. Taking the ratio of annual-average to winter parameters, we find that results differ noticeably from one study to another, reflecting statistical uncertainties and differences in environmental conditions or house operation. The differences are modest, however, so that the averages of the GM and GSD ratios, 0.81 and 0.89, respectively, provide a reasonable basis for inferring an annual-average GM and GSD from results of monitoring conducted only in the heating season. In aggregations where winter data are normalized to annual averages, we have therefore multiplied the winter lognormal parameters by the corresponding ratios. More detailed information would permit refining this simple approach, but we believe it would not change significantly the overall U.S. distribution that we calculate.

Considering the factors discussed above, we have aggregated the data in several fashions, with principal results summarized in Table

3. For these cases, we have used the GMs and GSDs cited in Table 1, rather than aggregating the data directly, since the individual data from some studies are not available and because this approach simplifies adoption of differing weightings and normalizations. The various aggregations are distinguished from one another not only by whether the annual/winter normalization is applied, but also by which data sets are included and how the individual data sets are weighted. We have considered either all 38 sets together (totaling 1377 houses) or merely the 22 sets (totaling 817 homes) that result from studies without prior expectation of high concentrations. We expect the latter grouping to yield results that are more representative of the United States as a whole.

The data sets have been weighted, not only by the number of homes monitored, but also with equal and with subjective weights (independent of number) . Although weighting by number is clearly appropriate when the samples are drawn from the same population, equal weights give an indication of the U.S. distribution if each study taken in itself is considered to represent an area (independently of the number of homes monitored). The subjective weights were employed to consider - on the basis of judgment alone - the population in the study area, the nature of the study, and - perhaps more importantly - whether there were prior indications of high concentrations, a consideration that is also served by limiting aggregation to data sets 1-22. Finally, for the normalized 22-set aggregation, we have also attempted a population-based weighting: with each data set from a city we have associated the approximate population within 50 miles (taking measurements to be indicative of concentrations in the local

area) and with each set from a state, the state's population (less any population already associated with cities).

As seen in Table 3, the distributions resulting from any of these aggregations have GMs in the range of 0.8-1.2 pCi/l (30 - 44 Bq/m^3) and GSDs of 2.6-3.1. Generally, those including all the data sets have larger GMs (about 1 to 30%) than those using the 22-set grouping, confirming the expectation that sets 23-38 tend to have higher concentrations than the others. Those employing the normalization of winter data have lower GMs and GSDs than those using the unadjusted data sets. The effects of using different weightings are more subtle: for the distributions utilizing all 38 sets, number-weighting yields higher GMs, but the same is not true for the 22-set distributions.

Taking important examples, number-weighting of all the data yields a GM of 1.22 pCi/l (GSD 3.1), implying that the average indoor concentration exceeds 2 pCi/l, with about 5% of homes exceeding 8 pCi/l; the winter normalization lowers the mean by 10%. Using all the data with a subjective weighting and winter normalization yields a GM of 0.97 pCi/l (GSD 3.0). The 22-set grouping with winter normalization and equal weighting yields a GM of 0.88 pCi/l (GSD 2.9), implying an average of 1.56 pCi/l and 2% above 8 pCi/l; population weighting yields a lower GSD (2.7), implying an average of 1.45 pCi/l and 1% above 8 pCi/l. We expect the 22-set grouping to be more representative of U.S. housing, particularly with equal or population weighting. (Number-weighted aggregations are dominated by the four sets of approximately 100 homes - Washington, Oregon, Houston, and Pittsburg.) Overall, we find that parameters of the

resulting distribution depend only modestly on the aggregation approach and vary in a way that is understandable in terms of the origin of the various data sets and the nature of the normalizations we have employed. An adequate expression of the range of results for the different aggregations, giving somewhat greater weight to the 22-set grouping with heating season normalization, is a geometric mean ^{222}Rn concentration of 0.9 $\pm$ 0.1 pCi/l (34 $\pm$ 4 Bq/m^3) and a GSD of 2.8 $\pm$ 0.2, with the expectation that 1-3% of single-family houses have average concentrations of 8 pCi/l (300 Bq/m^3) or greater.

Representativeness of the data and uncertainty of the aggregate distributions

These aggregate results imply an average indoor ^{222}Rn concentration in the vicinity of 1.5 pCi/l (55 Bq/m^3) and approximately a million homes with concentrations exceeding 8 pCi/l (which - at 80% occupancy - corresponds to an exposure rate of 1.6 WLM/yr, close to the NCRP limit). In terms of population exposure (and associated estimated population risk), they also imply a substantial proportion of risk among those who are relatively highly exposed. It is useful to examine specific aspects of the data and its aggregation that may affect these conclusions: to what extent are the data representative of the U.S. housing stock? Is the aggregate distribution self consistent and likely to be similar to that expected from a systematic representative survey? What degree of confidence can be placed in the aggregate results?

The total of 38 sets represents 21 states; the 22-set grouping

represents 17 states, still a substantial number. Although the smaller grouping may inadequately represent the U.S. midwest and south, every major area is represented to some extent in both groupings, including a notable number of major metropolitan areas. Regarding representation of the housing stock, the general method of selection - depending primarily on volunteers and participants in energy-conservation programs - probably favors middle-class housing, but the data have a significant component of low-income housing (e.g., 4 sets derived from a multi-city energy-conservation program[8]). The most obvious restriction of the sample is clear: it is representative only of the approximately 60 million single-family residences [9] constituting about 70% of the U.S. housing stock. Despite its shortcomings, the available sample appears to be an approximate representation of this dominant element of the housing stock, subject primarily to the limitation that only 22 (or 38) areas are sampled.

The degree of self-consistency in the data is also reassuring. For example, the implication of the aggregate parameters that about 2% of homes have levels exceeding 8 pCi/l is borne out by the data themselves. The comparison is most direct for unnormalized number-weighted aggregations: for the 22-set grouping, the distribution implies that 2.1% (i.e., 17) of the 817 homes should exceed 8 pCi/l, while the data themselves contain 24 (5 each in Fargo and Pittsburg, and 1 to 3 in each of 8 other sets). Thus the observed number is slightly greater than the estimate (and an order of magnitude higher than the 1 house implied by the NCRP's calculated 0.14%). Moreover, the appearance of such high concentrations among almost half of the data sets allays the fear that the tail of the aggregate distribution

depends to a substantial degree on high values from a single area.

We have also examined the distribution of the GMs of the individual data sets, which - for the 22 winter-normalized sets - themselves have a GSD of about 2.0. Adding this in quadrature to a median GSD from the same data sets, i.e., 2.2, yields an overall GSD of 3.0, consistent with that found by actual aggregation. With respect to the expected results of a truly representative survey including, say, 750 homes, a lognormal distribution with a GSD of approximately 3.0 would have a statistical uncertainty of about 4% in the GM. The uncertainty in an aggregation of the kind considered here is larger, being dominated not by uncertainties associated with the sample size, but by questions of representativeness and monitoring techniques. On the issue of sample selection, probably the more important, we note that - for 22 individual GMs distributed with a GSD of 2.0 - the aggregate mean has a standard error of 15%, corresponding to an uncertainty of 0.13 out of 0.9 pCi/l. Examining the effect of measurement uncertainty on the aggregate parameters, we find the GM and the fraction above 8 pCi/l to be virtually unaffected, while the GSD may be increased by 0.1 or less, depending on the uncertainty associated with the individual data.

Thus, the results of Table 3 are robust in terms of relative independence of aggregation procedure, and the uncertainty due to sampling procedure can be estimated. We therefore suggest that the ranges stated before, i.e., GM = 0.9 $\pm$ 0.1 pCi/l (34 $\pm$ 4 Bq/m^3) and GSD = 2.8 $\pm$ 0.2, be regarded to approximate the standard error, with at least 90% probability that the parent U.S. distribution has

parameters that fall within twice the stated uncertainty range. Similarly, within a factor of 2, 2% of houses are found to exceed 8 pCi/l (300 Bq/m^3), with little dependence on the method of aggregation.

Causes of the observed distribution

The two factors contributing directly to the distribution of concentrations of ^{222}Rn itself are the source strength, i.e., the rate at which ^{222}Rn enters the indoor atmosphere from its various sources, and the ventilation rate, which appears to have less variability than the source strength.[8,10,11] Contributions from the soil (the major U.S. source), domestic water, and building materials are reviewed elsewhere.[11-12] Overall, a fairly consistent picture is forming of the factors affecting entry and removal of ^{222}Rn and of their contribution to the observed distribution in indoor concentrations.[13] A part of this picture is the observation above that the GM itself varies substantially (GSD = 2.0) from one area to another, a variability that probably arises primarily from geographic variability in source strength and that is a principal consideration in developing methods of localizing high concentrations.[11]

A major recent incentive for studying indoor pollutants has been to assess the effect of infiltration-reduction measures designed to lower energy use.[14] Such measures typically effect a modest reduction in infiltration rates (e.g., 10-20%) and a similar increase in indoor concentrations.[15] Ventilation rates appear to be lognormally distributed with a GSD of about 2.0,[8,12] and the first-

order effect of a broad program of infiltration reduction is to shift the entire ^{222}Rn distribution slightly higher; to the extent that any housing class is affected more substantially, it is that with higher infiltration rates, tending to have lower ^{222}Rn concentrations.

Risk and regulatory implications

Several recent papers have applied the current understanding of ^{222}Rn-daughter epidemiology and dosimetry to environmental exposures. These yield estimates of the individual lifetime risk of lung cancer due to annual exposures of 0.2 WLM (the daughter exposure from 80% occupancy at indoor ^{222}Rn concentrations of 1 pCi/l) that cluster around 0.2%, ranging over a factor of 3 in either direction. An average residential concentration of 1.2 pCi/l, based on our result of 1.5 pCi/l in single-family houses and an estimate of 0.5 pCi/l in multi-family dwellings,[17] therefore implies a similar risk. Furthermore, it appears that approximately a million homes have concentrations exceeding 8 pCi/l, which implies an individual lifetime risk of approximately 2% to long-term occupants. Such risk estimates have substantial uncertainties (a factor of two or more), but it is startling to realize that this individual risk of 10^{-2} exceeds by three orders of magnitude the 10^{-5} ordinarily considered to warrant regulatory action by governmental agencies[18]; indeed, the <u>average</u> concentration of ^{222}Rn corresponds to a risk exceeding 100×10^{-5}. This does not, of course, imply that regulatory standards are appropriate to this situation, occurring as it does among 60 million privately-controlled environments. It does warrant serious characterization efforts and certainly provides a new perspective on

governmental actions on other environmental agents, and indeed on ^{222}Rn daughter exposures themselves: e.g., the expenditure of $0.7 billion to neutralize uranium mill tailings that cause perhaps tens - not millions - of individuals to suffer exposures greater than the NCRP remedial action limit.[19]

Turning to population doses and risks, an individual risk of 0.2% corresponds to an estimated incidence of lung cancer among the U.S. population of about 10,000 per year (depending significantly on the population mix and the period of expression for lung cancers induced). A surprisingly large fraction of this incidence (10-30%) is associated with houses having concentrations exceeding 8 pCi/l. Thus any program to reduce the exposures of those presently at high risk would not only reduce individual risk, but could also cause noticeable reduction in total population dose, comparable in size to the potential increase (10-20%) from a reduction in infiltration rates in the entire housing stock.

Finally, explicit consideration both of the average or population risk associated with the ^{222}Rn distribution and of the substantial incidence of high individual risks suggests the efficacy of a two-part approach to controlling ^{222}Rn-daughter exposures. One part would assure that general building practice avoids gross reduction in ventilation rates (except where there are compensating measures for controlling levels of ^{222}Rn and, presumably, other indoor pollutants); the ventilation part of a current industry standard has this objective and serves as an effective control on the average concentration.[20] The second part would provide an explicit exposure limit protecting

the individual, and this corresponds well with the objective of the new NCRP standard. The present scientific challenge is to develop sufficient understanding of the fundamental factors affecting radon source strengths to permit efficient identification of the geographic areas and homes with a substantial probability of high concentrations, as well as to serve as a basis for effective reduction of unacceptable levels.

ACKNOWLEDGEMENTS

This work was supported by the Director, Office of Energy Research, Office of Health and Environmental Research, Human Health and Assessments Division and Pollutant Characterization and Safety Research Division, and by the Assistant Secretary for Conservation and Renewable Energy, Office of Building Energy Research and Development, Building Systems Division, of the U.S. Department of Energy under Contract No. DE-AC03-76SF00098.

REFERENCES AND NOTES

1. A.V. Nero and W.M. Lowder, Eds., Indoor Radon: Health Phys. 45 pp. 273-561 (1983).

2. G.F. Clemente, H. Eriskat, M.C. O'Riordan, J. Sinnaeve, Eds., Indoor Exposure to Natural Radiation and Associated Risk Assessment (Proc. of conf., Anacapri, Italy, Oct. 3-5, 1983): Rad. Prot. Dos. 7 pp. 5-439 (1984).

3. "Working level month", a measure of exposure to daughters; cf. note 5 for discussion of units.

4. Exposures from the Uranium Series with Emphasis on Radon and its Daughters, Report No. 77, NCRP, Washington, 1984.

5. For purposes of Table 1, daughter concentrations are converted to ^{222}Rn concentrations assuming 0.5 equilibrium factor, the ratio of actual daughter concentrations (measured as potential alpha energy emitted) to that found in secular equilibrium with the ^{222}Rn. Equilibrium factors from 0.1 to 0.9 have been observed, but the average is usually close to 0.5 , implying 0.005 WL (working level) ^{222}Rn daughters per pCi/l ^{222}Rn. (If experienced 100% of the time, 0.005 WL causes an exposure of 0.25 WLM per year - 1 WLM results from 1 WL for a "working" month of 173 hours. Similarly, the NCRP's limit of 2 WLM/yr corresponds to continuous exposure to the daughters typically associated with 8 pCi/l ^{222}Rn.) Note that 1 pCi/l equals 37 Bq/m^3, the SI unit. Because the U.S. data are given in traditional units, we use pCi/l in the bulk of the paper to improve traceability, citing only the main results in SI units.

6. See for example I.M. Fisenne, A. George, M. McGahan, p. 555,

ref. 1.

7. H.W. Alter and R.L. Fleischer, Health Phys. 40, 693, (1981).

8. S.M. Doyle, W.W. Nazaroff, A.V. Nero, Health Phys., in press.

9. Energy Information Administration, Housing Characteristics, 1982, U.S. Government Printing Office, report DOE/EIA-0314 (82), Aug. 1984.

10. A.V. Nero, M.L. Boegel, C.D. Hollowell, J.G. Ingersoll, W.W. Nazaroff, p.401, ref. 1; set 27 mainly from solar homes.

11. A.V. Nero and W. W. Nazaroff, p. 23, ref. 2.

12. W.W. Nazaroff, S.M. Doyle, A.V. Nero, submitted to Health Phys.

13. Because equilibrium factors may vary, the daughter distribution may be slightly broader than the ^{222}Rn distribution. The opposite was observed in a Canadian survey that primarily performed grab samples in basements: R.G. McGregor et al., Health Phys. 39, 285, (1980). The ^{222}Rn measurements - effectively instantaneous samples - may have been highly sensitive to local and temporal variability in basement concentrations.

14. A.V. Nero, p. 277, ref. 1.

15. In some circumstances this may not occur; e.g., in houses with crawl-spaces, if infiltration-reduction efforts emphasize the understructure, both the source strength and ventilation rate may be reduced.

16. A.C. James (p. 353), N.H. Harley (p.371), and W. Jacobi (p. 395) in ref. 2; and papers by N.H. Harley and W.H. Ellett in Indoor Air and Human Health, proceedings of the ORNL Life Sciences Symposium, to be published. The highest risk estimate is that of the U.S. Environmental Protection Agency - about 1%

cited by Ellett (see also note 19).

17. The current understanding of ^{222}Rn sources suggests lower concentrations in high-rise apartments, which is confirmed in countries where these dominate the housing stock. As an example of the few U.S. data, the single third-floor apartment examined in ref. 28 was found to have a ^{222}Rn concentration of 0.26 pCi/l, at the bottom of the observed concentration range in the area studied and similar to outdoor concentrations (cf. T.H. Gesell, p. 289, ref. 1).

18. See, for example, C.R. Cothern, W.L. Lappenbusch, J.A. Cotruvo, Health Phys. 44, Suppl. No. 1, 377 (1983), including discussion; see also Federal Register 44, 68703 (Nov. 29, 1979), for discussion of risk assessment associated with control of trihalomethanes in drinking water.

19. Dose to the general public from tailings is indicated in Final Environmental Impact Statement for Standards for the Control of Byproduct Materials from Uranium Ore Processing, U.S. Environmental Protection Agency Report EPA 520/1-83-008-1, Sept. 1983. Appendix C describes the EPA dose-response analysis.

20. Ventilation for Acceptable Indoor Air Quality, American Society of Heating, Refrigerating, and Air-Conditioning Engineers, Standard 62-1981, Atlanta, 1981.

21. P. W. Thor, personal communication.

22. P.C. Nyberg and D.E. Bernhardt, p. 539, ref. 1.

23. J.J. Quackenboss, personal communication.

24. H.M. Prichard, T.F. Gesell, C.T. Hess, C.V. Weiffenbach, P. Nyberg, Environ. Int. 8, 83 (1982); measurements during air-conditioning season.

25. I. Nitschke, personal communication. Measurements spanning various seasons (with fall predominating) are taken here to approximate an annual average. Data also exist for 32 energy-efficient homes.

26. W.W. Nazaroff, F.J. Offermann, A.W. Robb, p. 525, ref.1.

27. R.L. Fleischer, A. Mogro-Campero, L.G. Turner, p. 407, ref.1; also includes data for 14 energy-efficient homes.

28. A.C. George and A.J. Breslin, in Natural Radiation Environment III, Vol. 2, T.F. Gesell and W.M. Lowder, Eds. (Technical Information Center/U.S. Department of Energy, CONF-780422, National Technical Information Service, Springfield, VA, 1980), pp. 1272-1292.

29. T.L. Hernandez and J.W. Ring, Environ. Int. 8, 45 (1982).

30. B.L. Cohen, to be published in Health Phys.

31. A.C. George, M. Duncan, H. Franklin, p. 291, ref. 2, and A.C. George, personal communication. Data set for Philadelphia uses average of winter and summer concentrations, where available, aggregated with a subset of winter-only concentrations normalized to an annual average (using GM and GSD ratios derived from the rest of the Philadelphia data set).

32. A.R. Hawthorne, R.B. Gammage, C.S. Dudney, in Indoor Air, B. Berglund, T. Lindvall, J. Sundell, Eds. (Proc. of conf., Stockholm, Sweden, Aug. 20-24, 1984), vol. 2, pp. 137-142; includes some measurements in basements. Stated GM and GSD are averages of values for two monitoring periods.

33. L.L. Lloyd, Butte Radiation Study, report to the 1981 Montana Legislature. GM and GSD were calculated from a fit to the number

of living-space measurements in four concentration intervals.

34. GM and GSD were derived by aggregating two data sets of "background" houses from remedial action survey: 29 houses (GM 1.44, GSD 1.7) cited along with cumulative probability plot in B.H. Peterson, U.S. Energy Research and Development Administration Report HASL-325 (1977), pp. 108-109 ; and 33 houses (GM 1.35, GSD 1.54 calculated from individual data), G.A. Franz, personal communication.

35. R.L. Douglas, J.M. Hans, T.A. Wolff, U.S. Department of Commerce Report PB-282-446 (1978); most Santa Fe homes contained pumice block.

36. J. Rundo, F. Markun, N.J. Plondke, J.Y. Sha, M.A. Essling, in Natural Radiation Environment, K.G. Vohra, U.C. Mishra, K.C. Pillai, S. Sadasivan, Eds. (Wiley Eastern Limited, New Delhi, 1982), pp. 155-162.

37. C.T. Hess, R.L. Fleischer, L.G. Turner, to be published in Health Phys. Data set for central Maine uses average of winter and summer concentrations, where available, aggregated with a subset of summer-only concentrations normalized to an annual average using GM and GSD ratios derived from the rest of the Maine data set. (Half of homes were known to have high levels of ^{222}Rn in water supplies.)

38. A.C. George and J. Eng, p. 397, ref. 1; these data are among sets 23-38 because of association with potential contamination, but this does not imply contamination of these houses.

39. H.M. Sachs, T.L. Hernandez, J.W. Ring, Environ. Int. 8, 97 (1982). We averaged winter and summer values from living areas; we assigned values of 0.1 pCi/l to four houses reported as zero.

40. D.J. Moschandreas, H.E. Rector, P.O. Tierney, GEOMET Technologies, Inc. Report GTI No. ES-877 (1981), and D.J. Moschandreas and H.E. Rector, Environ. Int. 8, 77 (1982). We omitted two data points due to sampling problems and assigned values of 0.1 pCi/l to two houses reported as zero.

41. W.M. Lowder, A.C. George, C.V. Gogolak, A. Blay, U.S. Atomic Energy Commission Report HASL TM 71-8 (1971). 42. L.T. Caruthers and A.W. Waltner, Health Phys. 29, 814 (1973). We adjusted their data assuming 0.5 equilibrium factor; activity underestimated slightly due to improper counting-time analysis.

43. Florida Department of Health and Rehabilitative Services, Study of Radon Daughter Concentrations in Structures in Polk and Hillsborough Counties, 1978. Data were used for houses on nonmineralized ("background") land and on land known to be mineralized (but not mined and reclaimed). (A slightly different set of 29 "background" houses - with GM 0.56 pCi/l, GSD 1.82 - is reported by R.J. Guimond, W.H. Ellett, J.E. Fitzgerald, S.T. Windham, P.A. Cuny, EPA Report 520/4-78-013 (1979).)

44. We are very grateful to those who provided us with as yet unpublished data. This work was supported by the Director, Office of Energy Research, Office of Health and Environmental Research, Human Health and Assessments Division and Pollutant Characterization and Safety Research Division, and the Assistant Secretary for Conservation and Renewable Energy, Office of Building Research and Development, Building Systems Division, U.S. Department of Energy under Contract No. DE-AC03-76SF00098.

Table 1. Radon-222 and daughter[5] concentrations measured in U.S. residences. Where individual data are available, preference is given to main-floor living-room or to averaged living-area values, from which the geometric mean (GM) and geometric standard deviation (GSD) are calculated; otherwise these parameters are taken from original literature. (Data sets 23-38 had some prior indication of the probability of high concentrations.)

	Location[ref]	No. of Houses	^{222}Rn Concentration		Measurement Protocol*			Aggregation Code+
			GM(pCi/l)	GSD	Tech.	Per.	Seas.	
1.	Washington[21]	138	0.71	2.48	TD	3m	W	H-4-4.1
2.	Oregon[21]	90	0.86	2.27	TD	3m	W	H-4-2.6
3.	Montana[21]	20	1.32	2.34	TD	3m	W	H-4-0.8
4.	Idaho[21]	17	1.30	2.94	TD	3m	W	H-4-0.9
5.	San Francisco, Cal.[10]	29	0.35	2.19	GS	I	S	4-4.0
6.	Las Vegas, Nev.[22]	3	0.79	2.47	TD	1y	Yr	1-0.5
7.	Col. Springs, Col.[8]	16	1.87	2.34	TD	4-5m	WSp	H-4-0.5
8.	Fargo, N. Dak.[8]	11	5.69	2.39	TD	4-5m	WSp	H-4-0.2
9.	Wisconsin[23]	50	1.10	2.17	TD	3-4m	W	H-4-4.7
10.	Houston, Tex.[24‡]	103	0.47	1.94	TD	3-6m	SF	2-3.1
11.	Portland, Maine[8]	1	0.44	2.98	TD	4-5m	WSp	H-4-0.5
12.	New York[25]	27	0.89	2.65	TD	2-9m	SF[25]	4-8.5
13.	Rochester, N.Y.[26]	8	0.50	4.08	CR	2w	W	H-2-1.0
14.	Northeastern N.Y.[27]	9	0.78	3.12	TD	~6m	FWSp	H-1-1.0
15.	N.Y. City area[28]	11	0.45	1.56	PM	1w/seas	2Yr	4-7.1
16.	New Jersey[28]	9	1.36	1.73	PM	1w/seas	2YR	4-4.0
17.	Princeton, New Jersey[29]	11	1.09	3.95	TD,GS	~5m	WSp	H-2-1.0
18.	Pittsburgh, Penn.[30‡]	122	1.45	2.35	TD	1y	Yr	4-2.9

Table 1. (Continued)

19.	Philadelphia, PA area[31]	31	1.84	2.32	AC	3d/seas	WS	A-4-7.1
20.	Damascus, Maryland[31]	41	3.04	2.11	AC	3d/seas	WSp	H-4-5.5
21.	East Tennessee[32‡‡]	40	2.0	2.5	TD	2x3m	WF	H-2-0.8
22.	Charleston, S. Car.[8]	20	0.47	2.12	TD	4-5m	WSp	H-4-0.5
23.	Butte, Mont.[33‡‡]	179	3.46 §	3.03 §	RP	1w/seas	Yr	2
24.	Grand Junction, Col.[34‡‡]	62	1.39 §	1.61 §	RP	1w/1m	Yr	2
25.	Santa Fe, N. Mex.[35]	6	0.94 §	2.26 §	RP	1-16d	Yr	1
26.	Farmington, N. Mex.[35]	6	0.74 §	1.66 §	RP	1-12d	SpS	1
27.	New Mexico[10]	9	2.31	2.45	GS	I	Sp	1
28.	Chicago, Ill.[36‡‡]	44	0.5	3.3	GS	I	F	4
29.	Central Maine[37]	70	1.66	2.56	TD	6-8m	1-2Yr	A-2
30.	Lewiston, N.Y.[38]	10	0.50	1.31	PM	1-2w/seas	2Yr	2
31.	Middlesex, N.J.[38]	15	0.52	1.39	PM	1-2w/seas	2Yr	2
32.	Canonsburg, Penn.[38]	8	0.94	2.15	PM	1-2w/seas	2Yr	2
33.	Eastern Pennsylvania[39]	36	3.29	3.41	TD	2-8m	WS	A-4
34.	Maryland[40]	58	1.90	3.69	GS	I	SpSF	2
35.	Oak Ridge, Tenn.[41]	14	1.28 §	2.24 §	GS	I	W	H-2
36.	Raleigh, N. Car.[42]	10	0.52	2.87	GS	I	F	2
37.	Florida (nonmin.)[43]	29	0.73 §	1.60 §	RP	1w/seas	Yr	4
38.	Florida (min.)[43]	4	2.14 §	2.51 §	RP	1w/seas	Yr	1

Footnotes to Table 1 on page 23.

Footnotes to Table 1

*Measurement protocol is indicated by symbols. Technique (Tech): TD = track-etched detector, GS = grab sample, CR = continuous radon monitor, PM = PERM (passive environmental radon monitor), AC = activated carbon integrating device, RP = RPISU (radon progeny integrating sampling unit). Period (Per): (#)y,m,w, or d = continuous number of years, months, weeks or days; I = Instantaneous; /seas means measurement performed each season, /1m means each month. Season (Seas): W = winter, Sp = spring, S = summer, F = fall, Yr = spans 4 seasons.

+ Gives normalization and weights (other than number of homes). Seasonal data normalization (if any): A = GM and GSD already reflect our best estimate of annual average concentration, usually 0.5x (winter value + summer value) where such data exist, aggregated (where needed) with a normalized subset of single-season values; H = heating season to be normalized to an annual average in aggregated data. Integer number gives subjective relative weighting factor to be applied to data set for aggregation purposes. Decimal number gives population weight, approximately equal to population (in millions) within 50-mile-radius centered on named city or within state (less any population assigned to cities).

‡ No data on individual houses; only statistical data were obtained.

§ ^{222}Rn daughter concentration was measured. cf. note 5.

TABLE 2. Comparison of annual-average* to winter ^{222}Rn lognormal parameters.

Location[ref]	No. of Houses with both Winter and Summer Measurements	Annual-Average* ^{222}Rn Concentration		Winter-Only ^{222}Rn Concentration		Ratio of Annual-Average to Winter Lognormal Parameters	
		GM(pCi/l)	GSD	GM(pCi/l)	GSD	GM Ratio	GSD Ratio
Pacific NW[21]	32	2.18	2.25	2.97	2.41	0.734	0.934
Central Maine[37]	58	1.61	2.52	1.66	2.81	0.970	0.897
Eastern Pennsylvania[39]	36	3.29	3.41	4.40	3.81	0.748	0.895
Philadelphia, PA area[31]	23	2.01	2.15	2.61	2.63	0.770	0.817
					Average Ratio	0.806	0.886

*0.5 x (winter + summer)

Table 3. ^{222}Rn concentration distributions for various data selections, normalizations, and weights.

Aggregation Type *		^{222}Rn Distribution†			Fraction of Homes Exceeding 8 pCi/l (Fraction of Population Exposure in these Homes)‡
		GM (pCi/l)	GSD	Average ⊕ (pCi/l)	
38 sets					
Un-norm	#Homes	1.22	3.14	2.35	0.051(0.31)
	Equal	1.07	3.08	2.01	0.037(0.25)
	Subj.	1.07	3.12	2.04	0.038(0.26)
Norm	#Homes	1.13	3.09	2.14	0.042(0.27)
	Equal	0.98	2.96	1.77	0.026(0.20)
	Subj.	0.97	2.98	1.76	0.027(0.20)
22 sets					
Un-norm	#Homes	0.97	2.81	1.65	0.021(0.16)
	Equal	1.01	3.14	1.94	0.035(0.25)
	Subj.	1.05	3.10	1.99	0.036(0.25)
Norm	#Homes	0.85	2.64	1.36	0.010(0.09)
	Equal	0.88	2.91	1.56	0.020(0.16)
	Subj.	0.92	2.89	1.62	0.021(0.16)
	Pop.§	0.89	2.68	1.45	0.013(0.11)

* Aggregate distributions labeled "38" include all data sets, while those labeled "22" exclude 16 sets with prior expectation of high ^{222}Rn concentrations. Those labeled "Unnorm" employ the parameters of Table 1 directly, while those labeled "Norm" indicate a normalization of sets

Footnote to Table 2 - continued

acquired during heating season only (labeled "H" in Table 1). Alternate weighting schemes are used for aggregating the data sets: number weighting (# Homes); equal weighting (Equal); subjective weighting (Subj.) by the integer (1-4) given in the aggregation code of Table 1; or population weighting (Pop.), for 22-set grouping only, using populations (in millions) given in the last column of Table 1.

+ The aggregate distribution is equal to $\Sigma w_i p(GM_i, GSD_i)$ where the ith data set is characterized by a lognormal probability function p with parameters GM_i and GSD_i, having a weight w_i, and where parameters for the aggregate distribution are then given by:

$$\ln GM = (\Sigma_i w_i)^{-1} \Sigma_i w_i \ln GM_i \quad \text{and}$$

$$(\ln GSD)^2 = (\Sigma_i w_i)^{-1} \{\Sigma_i w_i [(\ln GSD_i)^2 + (\ln GM_i)^2]\} - (\ln GM)^2.$$

⊕ For a lognormal distribution, the average (arithmetic mean) equals GM x exp $(0.5 (\ln GSD)^2)$.

‡ Similarly, these aggregations imply that 6-15% of homes have concentrations exceeding 4 pCi/l, representing 27-54% of total exposure, and that 19-33% exceed 2 pCi/l, representing 54-76% of total exposure.

§ Slight modifications of the population weighting scheme - e.g., adding the Chicago and nonmineralized Florida sets (28 and 37) or using a circle of radius 100 miles for associating city populations west of 90° west longitude - resulted in slightly lower GMs, slightly higher GSDs, and the same fraction exceeding 8 pCi/l.

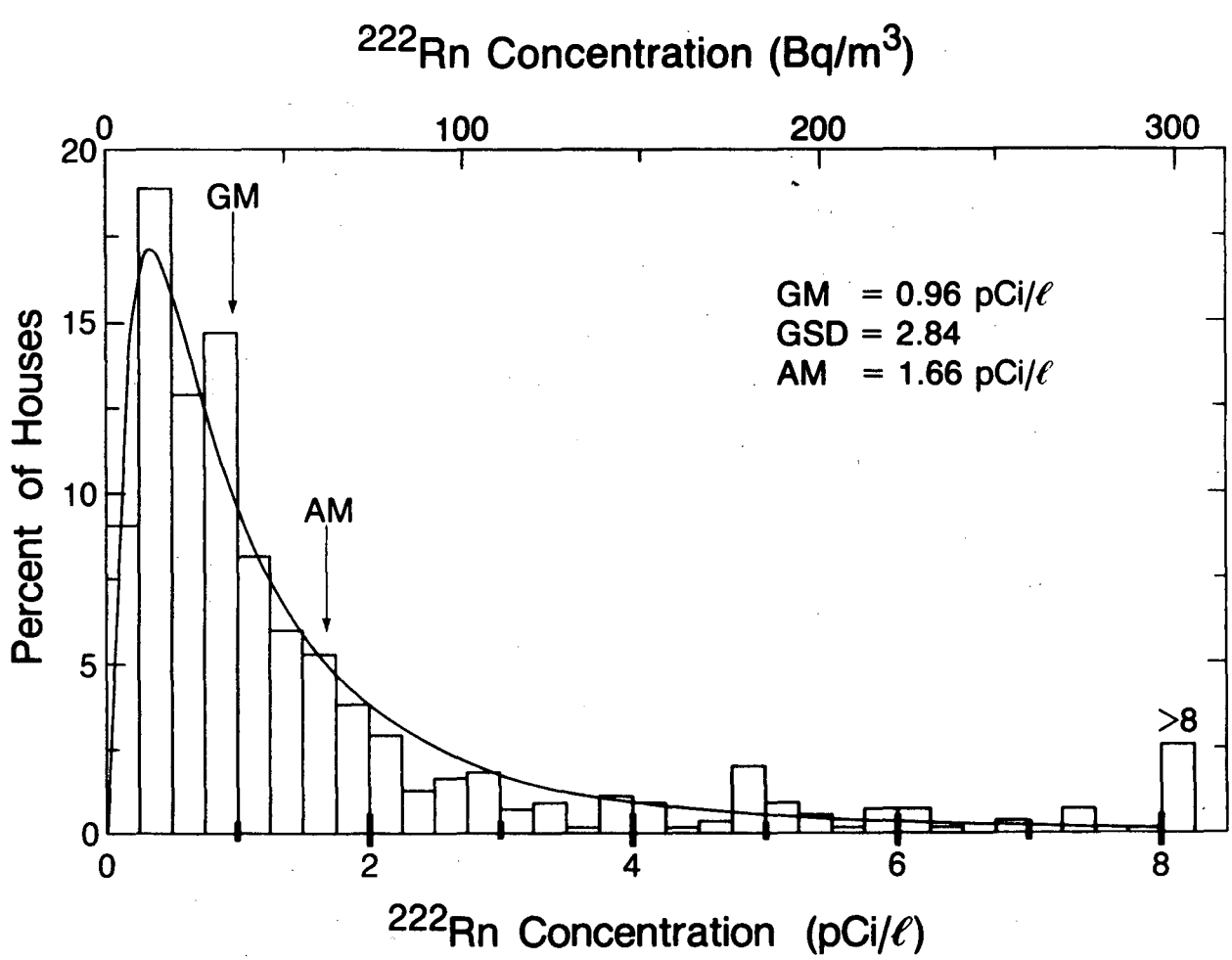

XBL 8411-4824

Figure 1. Probability distribution of ^{222}Rn concentrations from direct aggregation of the 552 individual data in 19 sets (1 to 22, less 10, 18, and 21, for which we do not have individual data). The smooth curve is the lognormal functional form corresponding to the indicated parameters, calculated directly from the data. The X^2 for the data with respect to this function is large enough to occur with only about 5% probability if the function represents the true distribution. The relatively large X^2 might be ascribed to the appearance of fewer houses at midrange concentrations (cf. 3 $\pm$ 1 pCi/l) than suggested by a lognormal distribution and to the corresponding appearance of more houses in the long tail and at low concentrations.

LAWRENCE BERKELEY LABORATORY
TECHNICAL INFORMATION DEPARTMENT
UNIVERSITY OF CALIFORNIA
BERKELEY, CALIFORNIA 94720

Lawrence Berkeley Laboratory
UNIVERSITY OF CALIFORNIA

Materials & Molecular
Research Division

A SUBNANOSECOND TIME-RESOLVED EMISSION STUDY OF Cu_2O AND GaAs

J.S. Weiner
(Ph.D. Thesis)

August 1984

Prepared for the U.S. Department of Energy under Contract DE-AC03-76SF00098

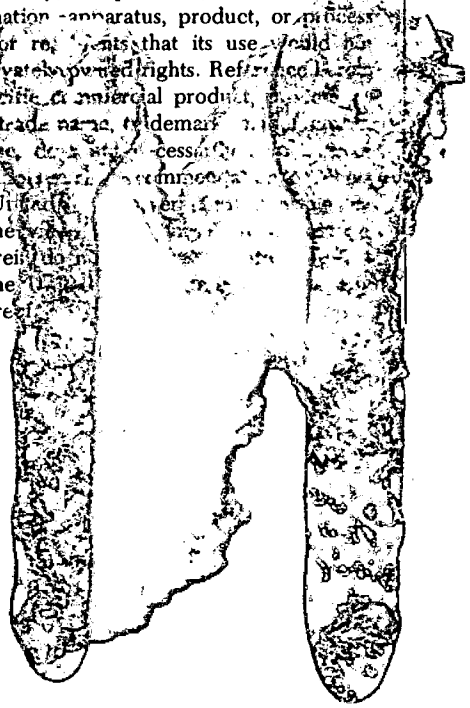

DISCLAIMER

LBL-18276

A SUBNANOSECOND TIME-RESOLVED EMISSION STUDY OF Cu_2O AND GaAs

Joseph S. Weiner
(Ph.D. Thesis)

Department of Physics
University of California, Berkeley

and

Materials and Molecular Research Division
Lawrence Berkeley Laboratory
Berkeley, California 94720

August 1984

This work was supported by the Director, Office of Energy Research, Office of Basic Energy Sciences, Materials Sciences Division of the U.S. Department of Energy under Contract Number DE-AC03-76SF00098.

A SUBNANOSECOND TIME-RESOLVED EMISSION STUDY OF Cu_2O AND GaAs

Joseph S. Weiner

ABSTRACT

This thesis presents a series of time-resolved luminescence and light scattering experiments which are aimed at studying how nonequilibrium electron-hole populations excited by picosecond laser pulses in semiconductors reach equilibrium. The development of a time-delayed coincidence photon counting system for the time-dependent measurements is described, and this system is tested by measuring the photoexcited free carrier lifetimes in GaAs doped with deep impurities.

The bulk of this thesis is devoted to the study of the dynamics of excitons in Cu_2O. We first develop a model to explain quantitatively the lineshape of nonthermalized luminescence spectra in Cu_2O which have been obtained with continuous wave lasers. Then we measure the time-dependence of the ortho-exciton and para-exciton populations in Cu_2O as a function of temperature. We demonstrate conclusively that the ortho-exciton lifetime is dominated by its decay into the para-exciton, and furthermore, this decay rate increases with temperature as $T^{3/2}$. As a result, at low temperatures the ortho-excitons and para-excitons are not in thermal equilibrium, but at $T>\sim 40\ ^{\circ}K$ the two exciton systems reach thermal equilibrium almost instantaneously.

We also studied the time-dependence of both one-phonon and two-phonon Raman modes when resonantly enhanced at the ortho-exciton in Cu_2O, and found from their time-dependence that these modes should be

more correctly identified as hot luminescence. To understand the one-phonon results we found it necessary to introduce a new relaxation process corresponding to scattering among the triply degenerate ortho-exciton states. From the two-phonon results we were able to directly determine the exciton lifetime as a function of its kinetic energy. These results are representative of information which cannot be determined from steady state measurements, so we conclude that time-dependent light scattering and emission measurement is a technique which is capable of greatly improving our knowledge about dynamic processes occurring not only in condensed matter, but, in principle, also in molecular and biological systems.

ACKNOWLEDGEMENTS

I wish to thank my advisor, Professor Peter Y. Yu, for his unrelenting support, guidance and encouragement during the course of my graduate career.

I would also like to thank Dr. Nathan Caswell for his collaboration in the early stages of this work.

Thanks to Chuck Collins, Farid Askary and Robbie Berg for their incessant wit and camaraderie. Also, thanks to Cynthia Bilorusky for typing my publications.

My deepest gratitude to Professor Y. R. Shen and Andre Mysyrowicz for providing the Cu_2O samples used in my experiments, and, for many valuable discussions, to Professor P. W. Yu of Wright State University, Dayton, Ohio for the Cr doped GaAs samples, and to Hewlett-Packard of Palo Alto for the pure and oxygen doped GaAs samples.

This work has been supported by the Director, Office of Energy Research, Office of Basic Energy Sciences, Materials Science Division of the U. S. Department of Energy under Contract Number DE-AC03-76SF00098.

TABLE OF CONTENTS

PART 1

I. INTRODUCTION

Much of what is known today about the properties of solids has been determined by means of optical spectroscopy. The earliest experiments consisted of absorptivity and reflectivity measurements using lamps as the excitation source. From these experiments it was possible to learn about the electronic and vibrational structure of semiconductors. The development of fixed frequency lasers facilitated photoluminescence and Raman scattering experiments, which provided additional information about the energy levels and made possible the study of excited state populations. With the advent of tunable lasers it became possible through excitation spectroscopies such as resonant Raman scattering to learn about the relative strengths of interactions such as that between electrons and phonons. All of these techniques use steady state excitation and therefore can provide little or no information about the dynamics of processes going on in solids. In many cases the dynamics of these processes can only be studied by time-resolved measurements. For example, questions have arisen as to whether resonant Raman scattering, which is a coherent process, can be distinguished from hot luminescence, which consists of absorption followed by emission.[1] It has been suggested that one means by which the two processes can be distinguished is by their different time-dependent behavior.

Within the past ten years the commercial development of reliable picosecond pulsed lasers has made possible a whole new range of time-resolved experiments for studying transient phenomena.[2] For example, using picosecond laser spectroscopy it is possible to measure free carrier lifetimes in a semiconductor containing deep traps. It is possible to directly observe how nonequilibrum carrier populations reach

equilibrium, and, it should be now possible to answer the question of whether resonant Raman scattering and hot luminescence can be distinguished.

The purpose of this thesis is to study the relaxation of photoexcited nonequilibrium electron and hole populations in semiconductors. For our materials we have chosen to study GaAs and Cu_2O, for the following reasons. GaAs is interesting from a technological standpoint. Its transport properties make it useful in fabricating fast electronic devices. An important parameter which characterizes such devices is the free carrier lifetime, which is determined by several posssible relaxation processes. Cu_2O, while not as useful as GaAs technically, is a simple classical system for studying properties of excitons, and, therefore, is well-suited for studies of the dynamical properties of excitons. We have investigated the dynamics of exciton relaxation in Cu_2O by means of time-resolved luminescence and light scattering measurements. One of our most important findings is that the time-dependent behavior of resonant Raman scattering at the yellow exciton in Cu_2O is consistent with its interpretation as due to hot luminescence. Further, we have been able to observe in real time how a nonequilibrium exciton population in Cu_2O reaches thermal equilibrium, and from these measurements we have obtained new information on exciton relaxation processes.

The organization of the thesis is as follows: The thesis is divided into two parts. In part 1 we describe the experimental apparatus and results of experiments in GaAs. Part 2 describes the experiments in Cu_2O. After the introduction in chapter I, the time-delayed coincidence photon counting system which makes possible our time-resolved

experiments is described in chapter II. This system has relatively poor (>50 psec) time resolution compared to the length of our laser pulses, but does have the excellent sensitivity needed to study weak emission and light scattering processes.

In chapter III the capability of our time-delayed coincidence photon counting system is demonstrated by measuring the free carrier lifetime of GaAs samples containing deep traps. The excellent signal to noise performance of this system allows us to distinguish between different decay mechanisms by their different time-dependence. In chapter IV a historical review of optical measurements in Cu_2O, and of its properties is presented. We point out a number of questions that have been raised by steady state measurements in Cu_2O, including questions specific to Cu_2O such as the decay mechanisms of its ortho-excitons, and, general questions, such as the nature of nonthermalized luminescence and the distinction between hot luminescence and resonant Raman scattering. Chapter V contains a study of nonthermalized luminescence spectra of Cu_2O obtained under steady state excitation. A theoretical model which explains quantitatively for the first time the nonthermalized luminescence spectra is presented. The same model with appropriate modifications is utilized later to explain the time-dependent measurements. The time-dependence of various luminescence peaks is presented in chapter VI. The time-dependence of resonantly enhanced one-phonon and two-phonon Raman modes in Cu_2O is presented in chapter VII. By interpreting these modes as due to hot luminescence we are able to explain not only the time-dependence of these modes but also some features of the CW Raman results such as the breakdown of the Raman selection rules which has been attributed to sample imperfections.[3]

Finally, our concluding remarks are contained in chapter VIII.

REFERENCES

1. Y. R. Shen, Phys. Rev. B 9, 622 (1974).

2. See for example Ultrashort Light Pulses, ed. by S. L. Shapiro (Springer-Verlag New York 1977) and references therein.

3. A. Z. Genack, H. Z. Cummins, M. A. Washington and A. Compaan, Phys. Rev. B 12, 2478 (1975); A. Compaan and H. Z. Cummins, Phys. Rev. Lett. 31, 41 (1973).

II. EXPERIMENTAL SETUP

The same experimental setup was used for all of our experiments, both cw and time-resolved. It is shown schematically in Figure 2.1. The laser consists of a Spectra Physics model 171 Argon ion laser, equipped with the model 342S modelocker unit, which produces ∿200 psec full-width-half-maximum (FWHM) pulses at intervals of ∿12 nsec. The output of the argon laser synchronously pumps a modelocked Spectra Physics model 375 dye laser, which provides a tunable source of picosecond pulses. Wavelength selection of the dye laser is provided by a two plate birefringent filter and an etalon, both of which are situated within the cavity of the dye laser. The dye laser produces pulses of ∿7 psec FWHM, which have a spectral width of ∿1 cm^{-1} FWHM. In order to prevent dye fluorescence from reaching the sample, the dye laser beam is filtered by passing the beam through two Brewster angle prisms. One advantage of this laser system is that it can be switched from pulsed to cw operation and back again simply by turning the modelocker off and on.

The samples were mounted on cold fingers in a Janis supervaritemp dewar, which could be maintained at temperatures ranging from 2°K to room temperature. The temperature of the cold finger was measured with a germanium diode temperature sensor. Temperature regulation was provided by a specially designed temperature controller.

Photoluminescence from the samples was analyzed by a Spex model 1403 double monochromator and a time-delayed coincidence photon counting system.[1] In this approach, a train of light pulses excites the sample and individual photons emitted or scattered by the sample are detected in a time-resolved manner by a fast photomultiplier tube. A portion of

the incident beam is split off and sent to a fast photodiode to provide a time reference. By counting for a long enough time, a histogram can be produced of the number of photons emitted from the sample as a function of their delay time with respect to the incident pulses.

This technique offers excellent sensitivity since single photons are being counted. As in conventional photon counting, the signal to noise ratio can be improved by counting for longer times. Also, the response of the system to laser pulses can be directly measured. The measured decay curves can then be deconvoluted with the instrument response, which substantially improves the time-resolution. One potential limitation of this technique is that the timing electronics can only respond to only one photon after each laser pulse. If more than one photon is emitted by the sample per laser pulse then the subsequent photons are ignored. In order to avoid distortion of the decay curves it is therefore necessary to keep the detection probability much less than one photon per excitation pulse, which can be accomplished by making the energy per pulse small, however, the signal to noise ratio can still be quite high if the repetition rate is high. The synchronously pumped modelocked laser is well-suited, therefore, for use with the time-delayed coincidence photon counting system because of its high repetition rate of 80 Mhz and low pulse energy of $\sim$1 nJ.

The timing electronics is shown schematically in Figure 2.1. The photoluminescence photons are detected by an Amperex model PM2254B photomultiplier tube with an S-20 photocathode. The output of the PMT is amplified by a B and H model DC3002 amplifier, inverted by a pulse inverter,[2] and then sent to an Ortec model 934 constant fraction discriminator (CFD). A portion of the incident beam is split off to be

used as a timing reference, and is detected by a Texas Instruments model TIED55 fast photodiode. The signal from the photodiode is sent to a second CFD. The outputs of the two CFDs are sent to an Ortec model 457 time to amplitude converter (TAC), which measures the time difference between the two signals and generates a pulse whose amplitude is proportional to the delay. The amplitude of the TAC output is analyzed by a LeCroy model 3001 multi-channel analyzer (MCA), which displays the number of photons versus time delay. The contents of the MCA are transferred to a Z-80 based microcomputer and stored on floppy discs for plotting and analysis.

The TAC has a dead time of 5 μs once it has been started, therefore, to avoid overloading it, the relatively infrequent pulses from the photomultiplier tube are used to start the TAC and the 80 Mhz pulse train from the fast photodiode is used to stop the TAC. The minimum time interval that the TAC can measure is 10 nsec, which is almost as long as the 12 nsec period between laser pulses. In order that the delay between the start and stop signals be long enough for the TAC to measure, we have devised a fast prescaler, using emitter coupled logic (ECL), which allows only every fourth photodiode pulse to reach the stop input of TAC. Since the photons which were emitted after any laser pulse can start the TAC, the spectra produced by the MCA contain several replicas of the time decay, separated by the period of the laser. This time interval can be precisely determined from the modelocker frequency, and provides an accurate calibration for our time-base.

Another limitation to the performance of the TAC is that its output shows some differential nonlinearity for delay times less than 50 nsec,

however, we were able to correct our data for this by by normalizing it with time spectra obtained by using a cw lamp as the signal source.

The instrument response of our system is shown in Figure 2.2. It has a FWHM of less than 400 psec. By deconvolution we have resolved decay times as short as 50 psec. The width of the instrument response is primarily due to the jitter in the transit time of electrons travelling between the cathode and the first dynode of the photomultiplier tube.[3] The instrument response time has been minimized for our system in two ways: First, by carefully adjusting the potentials on the various plates of the photomultiplier tube for the fastest response; and second, by using a floating lens to focus the collected light onto the spot on the photocathode which gives the fastest response.

We found that the adjustment of the CFD which was triggered by the photomultiplier tube also affected the width of the instrument response. In principle, the timing of the output pulses produced by the CFD should be independent of the amplitude of the pulses from the photomultiplier tube. In practice, in order to obtain the best possible instrument response, we found it necessary to set the CFD triggering threshold high enough to reject 50 % of the PMT pulses.

We also found that our spectrometer contributed considerably to the width of the instrument response. If $\Delta\nu$ and Δt are the spectral and temporal width of a light pulse there is an uncertainty principle, as a result of the Fourier transformation relating time with frequency, which states that $\Delta\nu\Delta t \geq A$, where A is a constant of the order of one. A high spectral resolution provided by the spectrometer will therefore decrease the temporal resolution. It can be shown that the temporal dispersion of

a grating spectrometer is given by $\Delta t=R/\nu$, where R is the grating resolution and ν is the light frequency.[4] For our spectrometer $\Delta t=300$ psec. The physical picture is that light rays which strike different parts of the grating traverse paths of different lengths in reaching the exit slit, so, the temporal dispersion of the spectrometer is proportional to the grating width. In practice, therefore, we found it necessary to use only half of the grating width in order to minimize the contribution of the spectrometer to the instrument response.

REFERENCES

1. K. G. Spears, L. E. Cramer and L. D. Hoffland, Rev. Sci. Instrum. 49, 255 (1978).

2. C. N. Winningstad, IRE Trans. Nuc. Sci. NS-6, 26 (1959).

3. B. Leskovar, C. C. Lo, Nuc. Inst. Meth. 123, 145 (1975).

4. N. H. Schiller and R. R. Alfano, Opt. Commun. 35, 451 (1980).

FIGURE CAPTIONS

Figure 2.1 Experimental setup for measuring time-resolved photoluminescence. CFD-constant fraction discriminator, TAC-time to amplitude converter, MCA-multi-channel analyzer.

Figure 2.2 Typical instrument response to a dye laser pulse of ∿7 psec long.

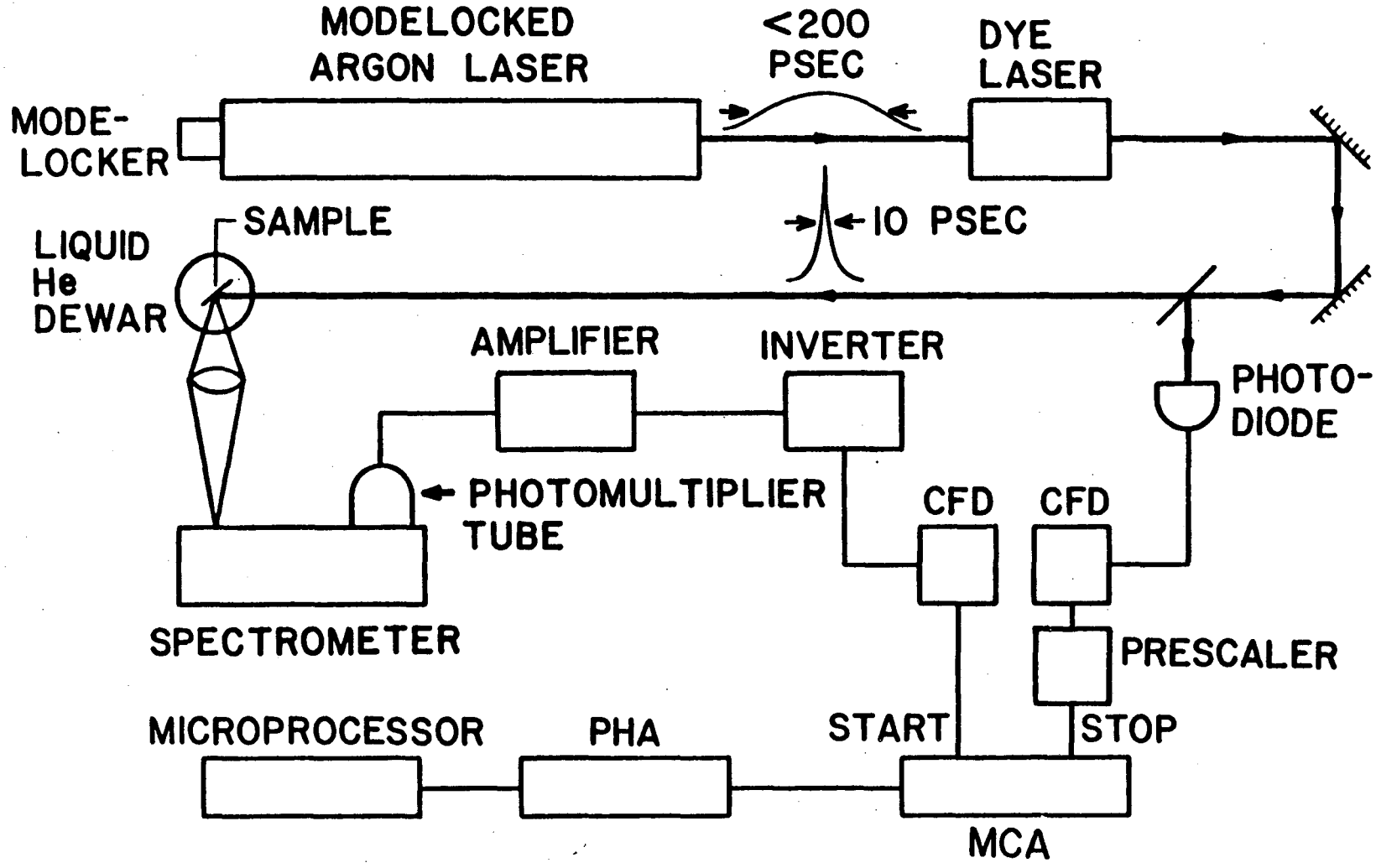
MODELOCKED
ARGON LASER
<200
PSEC
DYE
LASER
MODE-
LOCKER
SAMPLE
10 PSEC
LIQUID
He
DEWAR
AMPLIFIER
INVERTER
PHOTO-
DIODE
PHOTOMULTIPLIER
TUBE
CFD
CFD
SPECTROMETER
PRESCALER
MICROPROCESSOR
PHA
START
STOP
MCA
XBL 8312-4704

Figure 2.1

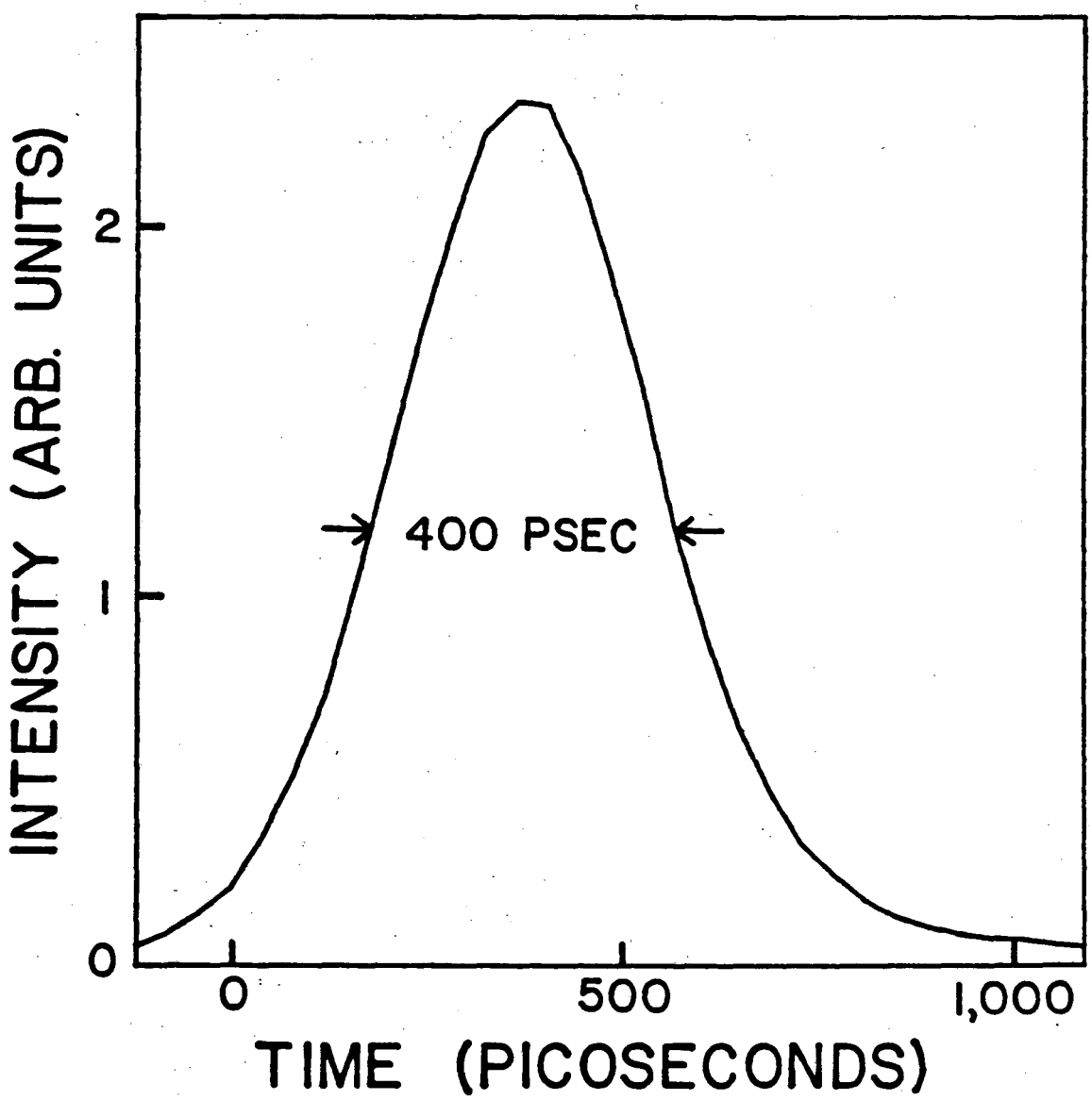
INTENSITY (ARB. UNITS)
2
1
0
400 PSEC
0
500
1,000
TIME (PICOSECONDS)

Figure 2.2

III. GaAs

This chapter describes our study of carrier lifetimes in GaAs. The mobility of electrons in gallium arsenide is higher than that of silicon, making gallium arsenide useful for constructing fast devices such as photodiodes[1] and photoconductive switches.[2] The switching recovery time of these devices is determined by the free carrier lifetime, which can be shortened by the addition of deep centers such as chromium or oxygen.

Free carrier lifetimes in GaAs:Cr and GaAs:O have been determined from time-dependent photoconductivity measurements.[1-3] This technique has several limitations: Time-dependence is measured by sampling oscilloscopes, which have poor sensitivity, so the measured decays are often noisy. In addition, the detector response can be distorted by the effects of stray capacitance or impedance mismatch.[3] It is therefore desirable to find a more effective means of measuring the photo-excited carrier lifetime. In section A of this chapter we demonstrate that this can be accomplished with a time-delayed coincidence photon counting system. Its high sensitivity makes it possible to distinguish between the different processes which affect the free carrier lifetime. In section B we describe our measurements of the lifetimes of bound excitons in GaAs. These lifetimes cannot be measured at all by photoconductivity since only carriers which are mobile can contribute to the photo-induced current. Bound exciton lifetimes have been determined by optical phase-shift photoluminescence measurements, but this technique has poor time resolution and sensitivity.[4]

A. Free Carrier Lifetime Measurement

1. Experiment

The experimental setup has been described in chapter II. The samples were cooled to a temperature of 40°K, at which the band gap of GaAs is 1.52 ev.[5] Styryl-9 dye was used in the dye laser in order to generate pulses in the infrared. The samples were excited with 1.56 ev photons. The energy per pulse was 0.75 nj. The dye laser was focussed onto a 100 μm diameter spot on the samples, producing an estimated 2×10^{15} free carriers/cm^3.

We examined the luminescence decay of five different gallium arsenide samples. A summary of their properties is contained in Table 3.1.

In Figure 3.1 we show the time-integrated photoluminescence spectrum of Cr doped GaAs (sample #1). The structure of interest is the dominant peak at 12,200 cm^{-1}. We have identified this peak as due to band to band recombination of photo-excited carriers from its photon energy and from the dependence of its intensity on temperature and laser power. It is present in all of the samples. Its time-decay is shown in Figure 3.2 (a), (b) and (c) for samples #5, 1 and 3 respectively. In all three spectra the curve labelled 'laser' represents the instrument response. We note that very little noise is present in the decay curves, and, in all three spectra the luminescence decay is clearly slower than the instrument response.

2. Theory

A number of processes can cause a decay of the photo-excited carrier population. These include: (i) radiative recombination; (ii)

Auger recombination; (iii) Trapping at impurities; (iv) Surface recombination and (v) Diffusion of carriers away from the area of observation.

Radiative recombination in gallium arsenide has been studied extensively,[6] and measured lifetimes range from 1 nsec for heavily doped ($10^{19}cm^{-3}$) samples to as long as 1 μsec for undoped samples. Given the moderate doping densities ($<6x10^{17}cm^{-3}$) and photo-excited free carrier densities ($2x10^{15}cm^{-3}$) of our experiment, the radiative recombination rate should be negligible. Similarly, Auger recombination only becomes significant for carrier densities higher than $10^{19}cm^{-3}$ and should be negligible in our experiment.[7]

Due to the strong absorption in GaAs, above bandgap photo-excitation produces a nonuniform distribution of carriers which is localized close to the surface of the sample. Surfaces tend to have a high defect concentration due to dangling bonds or impurities, so surface recombination can be significant. The large density gradient at the surface will cause most of the carriers to diffuse into the bulk where their recombination luminescence will be reabsorbed. This diffusion, therefore, will also contribute to the luminescence decay.

In order to determine the contributions of bulk and surface recombination and diffusion to the observed luminescence decay, we use the following model. The crystal is semi-infinite, with its surface at z=0. Assuming constant carrier concentration in the x and y directions, the diffusion equation for the free carrier concentration N is:

$$\frac{dN}{dt} = G(z,t) + D\frac{\partial^2 N}{\partial z^2} - \frac{N}{\tau} \qquad (3.1)$$

where G(z,t) is the generation rate, D is the ambipolar diffusion constant, and τ is the bulk recombination lifetime due to trapping at

defects and impurities. Equation (3.1) has to be solved subject to the boundary conditions that:

$$D\frac{\partial N}{\partial z}\Big|_{z=0} = N(0,t)S \qquad \text{and} \qquad N(\infty,t) = 0 \tag{3.2}$$

where S is the surface recombination velocity. We will assume that the incident laser pulse is a delta function in time so that G(z,t) is given by:

$$G(z,t) = N_o \delta(t) e^{-\alpha_i z} \tag{3.3}$$

where α_i is the absorption coefficient of GaAs at the incident laser frequency.

The time-dependent emission intensity can be calculated from N(z,t) using the expression:

$$I(t) \propto \int_0^\infty e^{-\alpha_i z} N(z,t)\,dz \tag{3.4}$$

where α_e is the absorption coefficient of GaAs at the emission frequency. The exponential term accounts for the reabsorption of light emitted from carriers within the bulk. The solution to equations (3.1)-(3.4) has been shown to be:[8]

$$I(t) \propto e^{-t/\tau}\left[A_1 W(\alpha_i \sqrt{(Dt)}) + A_2 W(S/D\sqrt{(Dt)}) + A_3 W(\alpha_e \sqrt{(Dt)})\right] \tag{3.5}$$

where $W(x) = \exp(x^2)\operatorname{erfc}(x)$ and erfc is the complementary error function.

$$A_1 = \frac{\alpha_i}{\alpha_i^2 - \alpha_e^2} + \frac{2S/D}{(S/D - \alpha_i)(\alpha_i - \alpha_e)} \tag{3.6}$$

$$A_2 = \frac{2S/D}{(S/D - \alpha_i)(\alpha_e - S/D)} \tag{3.7}$$

$$A_3 = \frac{2}{\alpha_i + \alpha_e} - A_1 - A_2 \tag{3.8}$$

The term outside the brackets in Equation (3.5) is a simple

exponential decay with decay time τ. The terms inside the brackets are significant only when S and D are both large. Since these terms lead to non-exponential decaya, the surface recombination and diffusion terms can be readily distinguished from the bulk recombination term.

3. Comparison of Theory and Experiment.

The bulk lifetimes of our samples were determined by convoluting Equation (3.5) with the instrument response and adjusting the lifetime to fit the experimental curves. The absorption coefficients were taken to be $\alpha_i = 1.2 \times 10^4 cm^{-1}$ and $\alpha_e = 10^4 cm^{-1}$.[4] In all cases the best fits were obtained when S and D were assumed to be negligible. Significantly worse fits were obtained if we assumed that S and D have values typically quoted in the literature.[9] For example, the broken curve in Figure 3.2 (b) was calculated by assuming D = 10 cm^2 sec^{-1}, S = 10^6 cm sec^{-1} and τ = 300 psec, while the dotted curve was obtained by assuming S = D = 0 and τ = 170 psec. The bulk recombination times obtained for all five samples are listed in Table 3.1. The shortest times that we measured in the semi-insulating samples are consistent with transient photoconductivity measurements in Cr doped GaAs.[1]

By comparing the free carrier lifetime in the pure GaAs sample with those of the semi-insulating samples we conclude that the free carrier lifetimes in the sami-insulating samples are limited by trapping at the deep levels which are present. In principle, if the trap concentration is known, the trapping cross section, σ, can be calculated from the measured lifetime by assuming:

$$1/\tau = N_t \langle v \rangle \sigma \tag{3.9}$$

where $\langle v \rangle$ is the thermal velocity of the carrier trapped and N_t is the

trap concentration. The measured lifetimes in samples #1 and #2 are not inversely proportional to the known Cr concentration, which suggests that the actual numbers of traps in our samples are different from their Cr concentrations, so, to determine σ with this technique requires a more reliable measurement of the trap density.

B. Lifetimes of Bound Excitons

1. Experiment

We performed our measurements on our high purity sample #5. The sample was immersed in liquid helium at the Lambda point, 2.17°K. The laser was tuned to an energy of 2 ev, well above the bandgap of GaAs, and the laser light was focussed onto the sample with a cylindrical lens to produce an average power density of 0.7 W cm^{-2}.

A time-integrated spectrum is shown in Figure 3.3. This spectrum is similar to those previously published.[4,10] Peak #7 at 12,219 cm^{-1} has been identified as due to free exciton recombination and peaks #1-5 are due to recombination of bound excitons. We found that peaks #1-5 saturated easily with increased incident intensities and exhibited extremely strong temperature dependence. These properties support the assignment of peaks #1-5 to bound excitons. Unfortunately most of the peaks overlap each other, making unambiguous determination of the lifetimes difficult, however, we did measure the lifetimes of peaks #1 and 3.

2. Results

The solid curves in Figure 3.4 (a) and (b) represent the decay in time of the luminescence peaks #1 and 3 respectively. We determined the

lifetimes of the peaks by convoluting the instrument response with a single exponential and fitting the resultant curve to the data (shown as the dotted curves in Figure 3.4 (a) and (b)). The lifetime of peak #1 is 2.6 ± 0.2 nsec, and of peak #3 is 1.4 ± 0.1 nsec. The latter measurement is in agreement with the value of 1.6 ± 0.6 nsec reported by Hwang[4] for the lifetime of an exciton bound to a neutral acceptor in GaAs.

C. Conclusions

We have demonstrated that the technique of time-delayed coincidence photon counting can be used to simply and easily measure decays with lifetimes shorter than 100 psec, and to measure the decays of very weak spectral features.

Table 3.1

GaAs Samples

Sample	Dopant and Concentration	Other Characteristics	τ (psec)
1[a]	Cr: $10^{15}cm^{-3}$		170
2[a]	Cr: $2x10^{16}cm^{-3}$		90
3[a]	Cr: $1.6x10^{17}cm^{-3}$		<90
4[b]	O: $6x10^{17}cm^{-3}$	LEC Grown	250
5[b]	undoped, $N_a, N_d < 10^{14}cm^{-3}$	4 μm thick epi-layer on semi-insulating substrate	1200

[a]Obtained from Wright State University, Dayton, Ohio.

[b]Obtained from Hewlett-Packard, Palo Alto, CA.

REFERENCES

1. C. H. Lee, A. Antonetti and G. Mourou, Optics Commun. 21 158 (1977); C. H. Lee, Appl. Phys. Lett 30, 84 (1977).
2. See for example G. Mourou and W. Knox, Appl. Phys. Lett. 35, 492 (1979).
3. B. Hwang, F. A. Lindholm, and R. B. Hammond, IEEE J. Quantum Electron. QE-19, 648 (1983).
4. C. J. Hwang, Phys. Rev. B 8, 646 (1973).
5. J. S. Blakemore, J. Appl. Phys. 53, R123 (1982).
6. R. J. Nelson and R. G. Sobers, Appl. Phys. 49, 6103 (1978).
7. W. Rosenthal, Solid State Commun. 13, 1215 (1973).
8. J. Vaitkus, Phys. Stat. Solidi 34, 769 (1976).
9. C. Hoffman, H. J. Gerritsen and A. V. Nurmikko, J. Appl. Phys. 51, 1603 (1980).
10. See P. J. Dean and D. C. Herbert; in Excitons, ed. by K. Cho (Springer-Verlag, New York) p. 55.

FIGURE CAPTIONS

Figure 3.1 Time-integrated luminescence spectrum of Cr doped GaAs (sample #1). The main peak at 12,200 cm^{-1} is identified as due to band-to-band recombination of electrons and holes.

Figure 3.2 Time-dependent decay of the band-to-band luminescence in (a) undoped GaAs (sample #5), (b) GaAs doped with $10^{15} cm^{-3}$ of Cr (sample #1) and (c) GaAs doped with $1.6 \times 10^{17} cm^{-3}$ of Cr (sample #3). The dots are best fits obtained by convolution of the instrument response (curves labelled as 'laser') with Equation (3.5), assuming S=D=0, and lifetimes given in Table 3.1. In (b) the broken curve was similarly obtained using D=10 cm^2 sec^{-1}, $S=10^6$ cm sec^{-1} and τ=300 psec.

Figure 3.3 Time-integrated luminescence spectrum of high purity GaAs (sample #5) at a temperature of 2.2°K. Peak #7 is due to free exciton recombination. The remaining peaks are due to recombination of bound excitons.

Figure 3.4 Time-dependent decay of bound exciton luminescence lines (a) peak #1 and (b) peak #3. The dotted lines are fits obtained by convoluting the instrument response with a single exponential with lifetimes of 2.6 nsec and 1.4 nsec respectively.

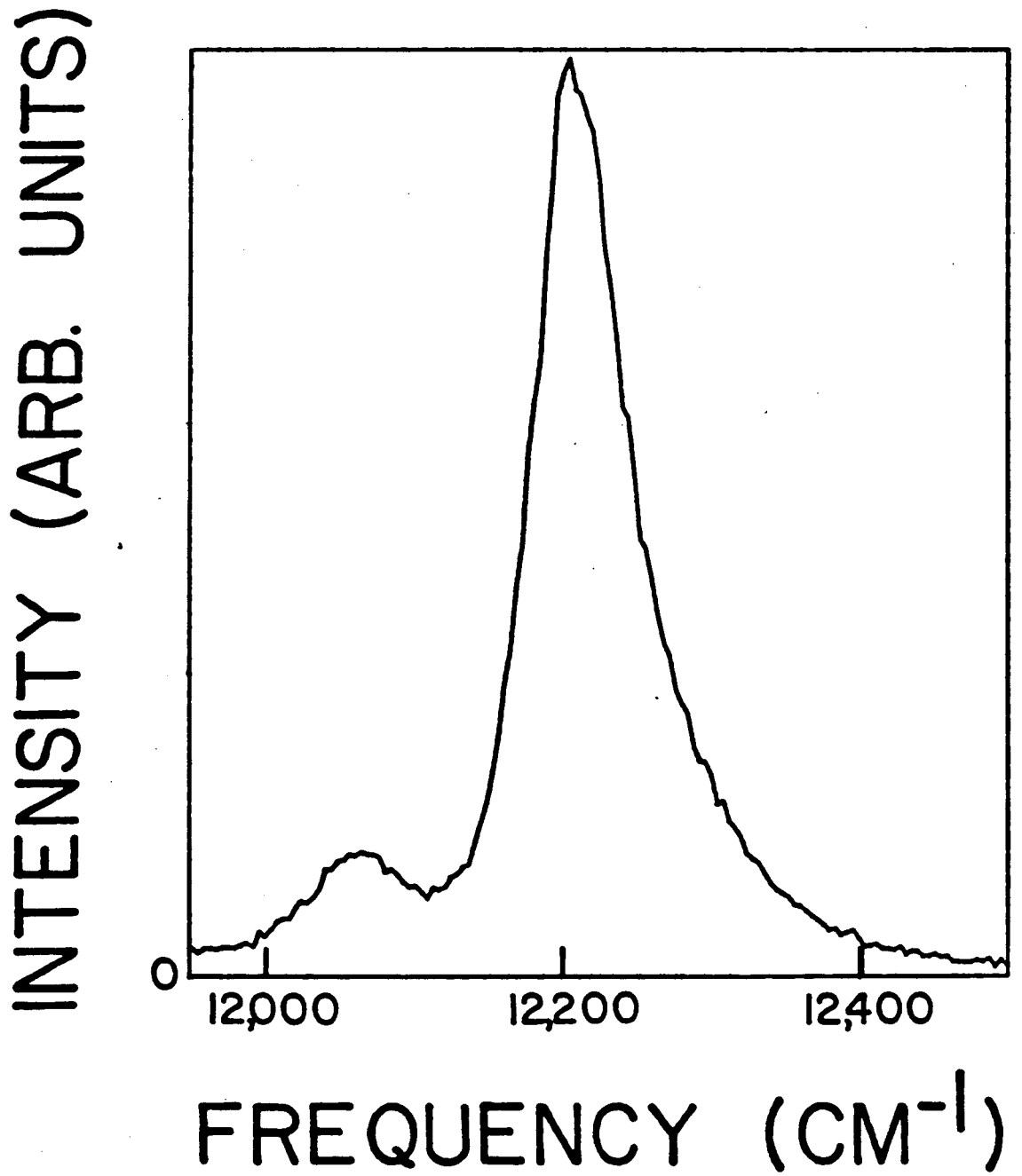

XBL 8312-4702

Figure 3.1

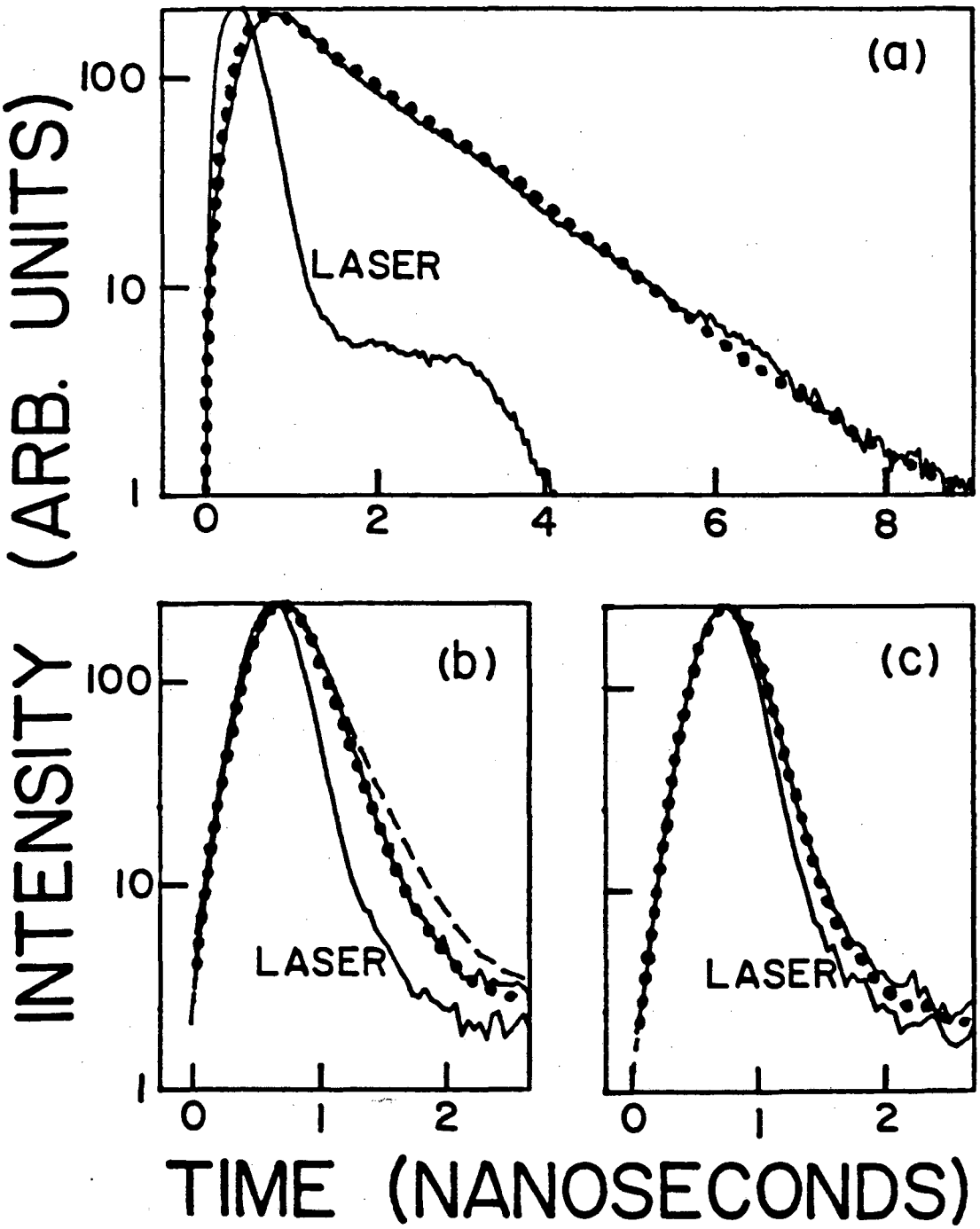

XBL 8312-4703

Figure 3.2

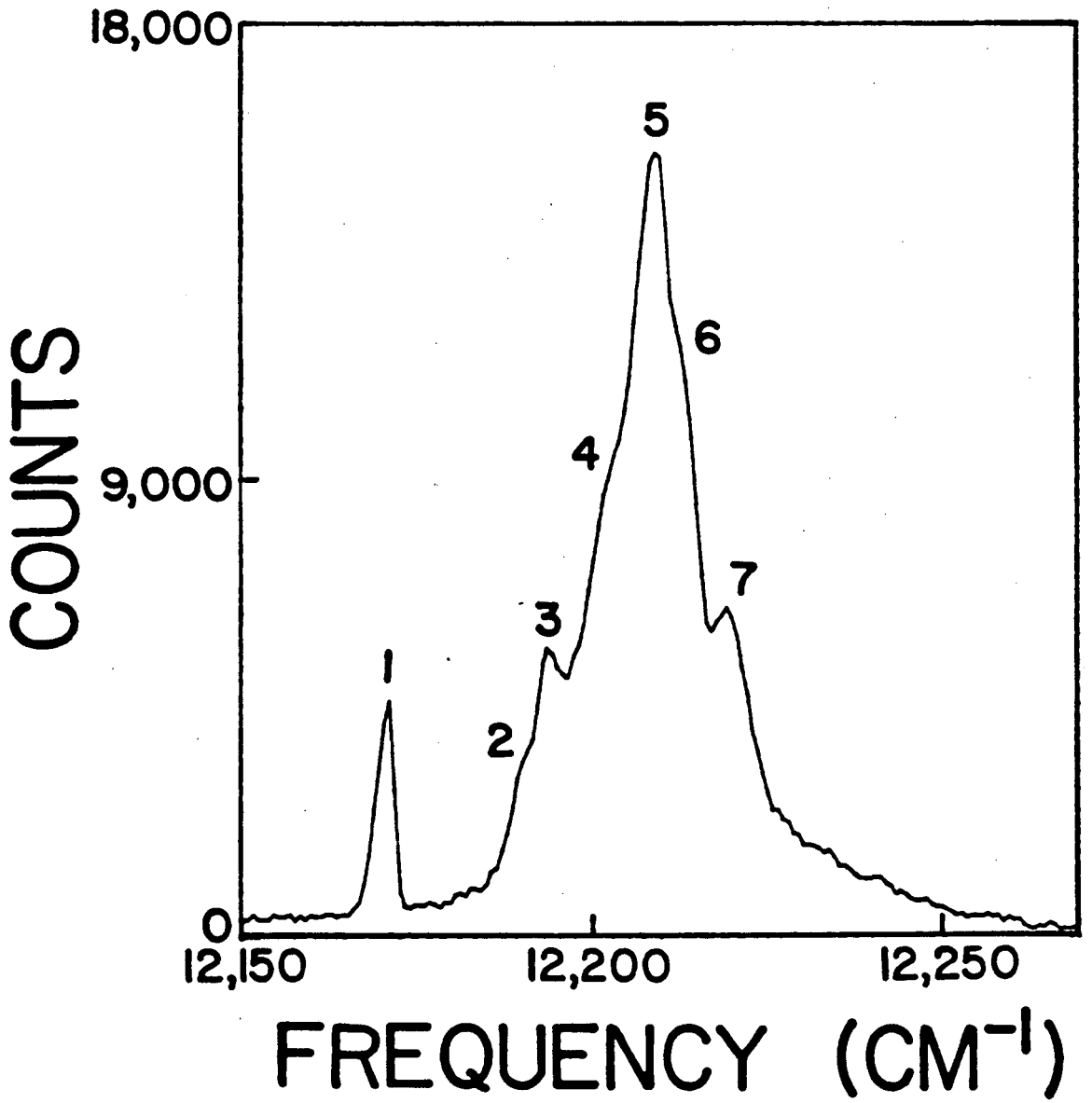
18,000
9,000
0
COUNTS
1
2
3
4
5
6
7
12,150
12,200
12,250
FREQUENCY (CM⁻¹)

Figure 3.3

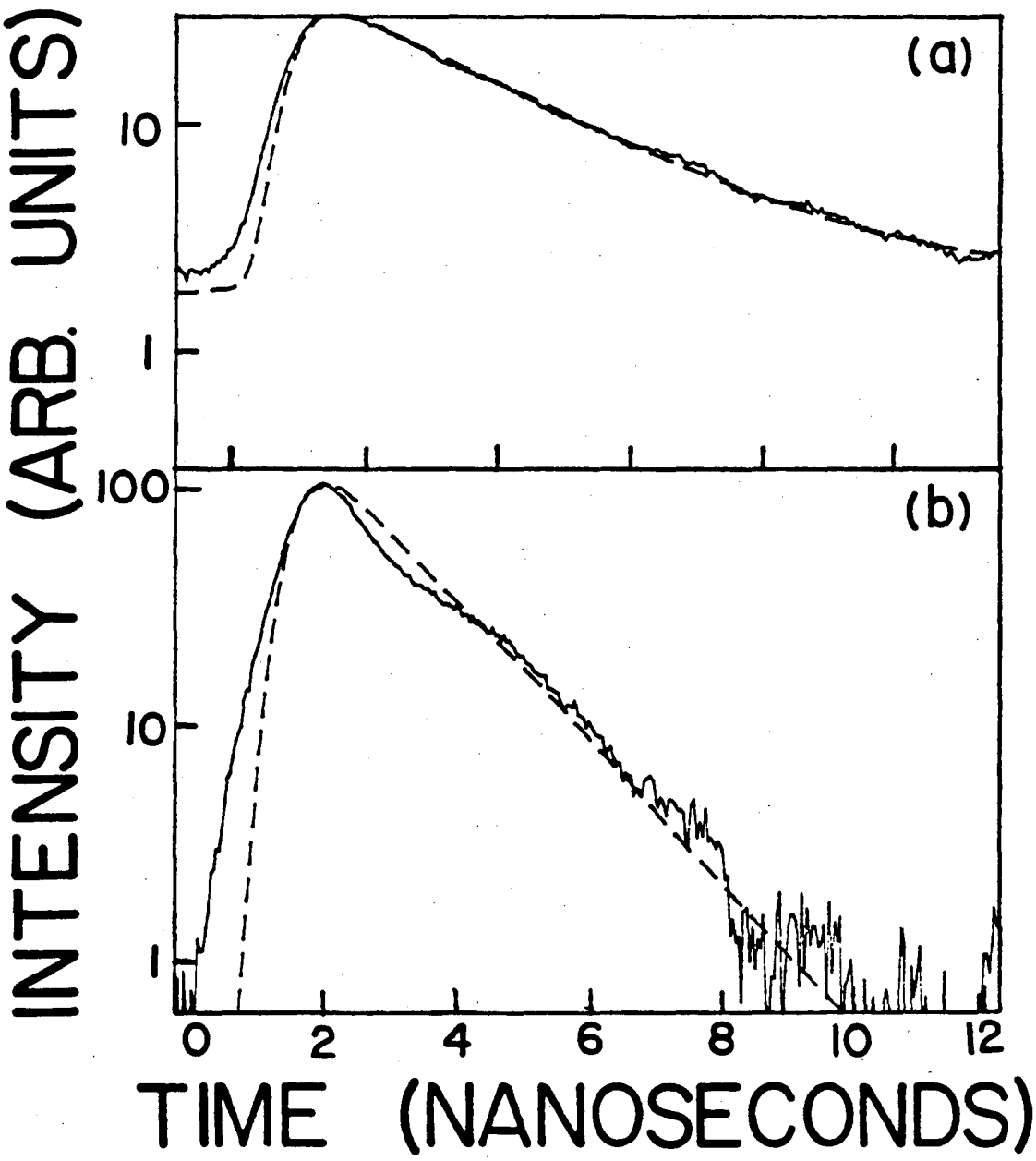
INTENSITY (ARB. UNITS)
(a)
10
1
100
(b)
10
1
0
2
4
6
8
10
12
TIME (NANOSECONDS)

Figure 3.4

IV. OPTICAL PROPERTIES OF Cu_2O

Part 2 of this thesis consists of work aimed at understanding the dynamics of excitons in Cu_2O. Cu_2O is a good system in which to study exciton dynamics because most of its properties are well-known. This chapter provides a review of past work on Cu_2O. In section A the electronic and vibrational structure of Cu_2O are discussed. Sections B and C describe the results of photoluminescence and Raman scattering measurements respectively. Section D describes the time-resolved measurements that have been made to date. In section E we summarize the questions which have been raised that we will study using time-resolved techniques.

A. Electronic and Vibrational Structure[1-13]

Cuprous oxide crystallizes in a cubic lattice with space group O_h^4. It is a direct gap semiconductor. It has six atoms per unit cell and therefore 15 optical phonons. The crystal has inversion symmetry, so its electronic and vibrational eigenstates all have definite parity. Evidence for the existence of excitons was first seen in Cu_2O,[3] and it remains a classic system for the study of the properties of excitons.

The absorption spectrum of Cu_2O exhibits several Rydberg-like series corresponding to the creation of excitons (Figure 4.1). The series are termed yellow, green, blue, or indigo according to their positions in the visible spectrum. The yellow series consists of excitons formed from the lowest energy conduction band and the highest energy valence band (Figure 4.2). At 4.2 °K it is given by:

$$E_n = 17{,}525 - \frac{786}{n^2}\ cm^{-1} \qquad n=2,3,4,... \tag{4.1}$$

The n=1 line occurs at an energy of 16,400 cm^{-1}, lower than predicted by Equation (4.1), and is very weak. To explain the small oscillator strength, Elliot proposed that the valence band (Γ_7^+) and conduction band (Γ_6^+) have the same parity so that 1S exciton transitions are electric-dipole forbidden.[4] The 1S exciton absorption line is then due to electric-quadrupole transitions. Electric-quadrupole absorption is expected to be anisotropic, even in a cubic crystal such as Cu_2O. This has been experimentally observed by Gross and Kaplyanskii, in support of Elliot's theory. A controversy was touched off by the band structure calculation of Dahl and Switendick[6] which predicted valence and conduction band symmetry assignments inconsistent with this model. More recently, however, Kleinman and Mednick[7] performed a self-consistent calculation of the energy bands of Cu_2O which does agree with Elliot's model. The accepted symmetries of the bands in Cu_2O are given in Figure 4.2.

The 1S exciton can also be excited by phonon-assisted electric-dipole transitions, which give rise to several steps in the absorption continuum beginning at 16,490 cm^{-1}.[3] Elliot[4] showed that Cu_2O has optical phonons with symmetries: (i) $\Gamma_{15}^-(1)$ and $\Gamma_{15}^-(2)$ (TO and LO) which are infrared active; (ii) Γ_{25}^-, Γ_{12}^- and Γ_2^- which are silent modes; and (iii) Γ_{25}^+, which is the only Raman active mode. Only the Γ_{15}^-, Γ_{25}^-, Γ_{12}^- and Γ_2^- phonons can participate in phonon-assisted transitions to the 1S exciton. Table 4.1 gives the energies of the zone center phonons that have been measured via absorption,[8,9] resonant Raman scattering,[10] photoluminescence[11] and neutron scattering.[12] The energies are in good agreement with the values which have been theoretically obtained.[13]

B. Photoluminescence Spectra[11,14-23]

Several researchers have studied photoluminescence in Cu_2O. The photoluminescence spectrum exhibits transitions involving the same phonons as in indirect absorption. The energies and interpretations of the different luminescence lines that have been observed are detailed in Table 4.2.[11] The zero phonon line is observed at the same energy in both absorption and emission.

The strongest phonon-assisted luminescence line is mediated by the Γ_{12}^- phonon. This is probably due to the close proximity of the Γ_{12}^- conduction band, which acts as the resonant intermediate state. The Γ_{12}^- phonon has negligible dispersion and its coupling to the ortho-exciton is independent of k-vector, so the lineshape of the phonon-assisted luminescence is given by:[14]

$$I(\omega_s) \propto g(E)\rho_k(E) \quad ; \quad E = \hbar\omega_s + \hbar\omega_{12} - \hbar\omega_{1S} \tag{4.2}$$

$g(E)$ is the exciton density of states and $\rho_k(E)$ is the exciton distribution function, which for a population in thermal equilibrium is usually approximated by the Boltzmann distribution $\exp(-E/K_bT)$. The Γ_{12}^- phonon-assisted line displays different lineshapes depending upon sample preparation. Naturally occurring and melt-grown samples show spectra like that in Figure 4.3 (a), where the width of the Γ_{12}^- phonon-assisted line varies with temperature. Samples grown by oxidation of copper show much weaker luminescence spectra like that in Figure 4.3 (b). The phonon-assisted line is much broader and is insensitive to temperature. It has been suggested that in the latter type of samples the photo-excited excitons decay before reaching thermal equilibrium. This may be due to the presence of many defects in these samples, resulting in a short non-radiative lifetime and low quantum efficiency. In chapter V we

will quantitatively explain the phonon-assisted luminescence lineshapes in Cu_2O. A nonthermal exciton distribution has also been observed in strongly excited melt grown and natural samples, because the exciton lifetime is shortened by exciton-exciton collisions at high density.[15,16]

The luminescence lines at 16,181 cm^{-1} and 16,201 cm^{-1} exhibit very strong temperature dependence and therefore are probably due to phonon-assisted luminescence from a weakly bound exciton.[17]

The anomalous temperature dependence of the line occurring at 16,219 cm^{-1} has caused it to be attributed to phonon-assisted recombination of the 1S para-exciton.[18] The 1S exciton is split by the exchange interaction between the electron and hole spins into a Γ_{25}^+ triplet and a Γ_2^+ singlet state, which are referred to as the ortho-exciton and para-exciton respectively, by analogy with the hydrogen molecule. The ortho-exciton is the state occurring at 16,400 cm^{-1} which has been discussed so far. Group theoretical analysis indicates that the para-exciton can recombine via a Γ_{25}^- (87 cm^{-1}) phonon-assisted electric dipole transition, Thus, if the 16,219 cm^{-1} line is identified with this transition then the para-exciton level would lie at 16,303 cm^{-1}. Several experiments have confirmed this assignment. A line appears in the absorption spectrum at this energy when the crystal is either uniaxially stressed,[19] or, subjected to a magnetic field.[20] An absorption edge starting at 16,388 cm^{-1} due to Γ_{25}^- phonon--assisted transitions to the para-exciton has also been observed.[21]

Gross, Kreingol'd, and Makarov[19] have studied ortho- to para-exciton relaxation by monitoring the temperature dependence of the ortho-exciton luminescence intensity (Figure 4.4). They found that for

temperatures greater than 30°K the intensity of the Γ_{12}^- phonon-assisted recombination peak increases as $\exp(-\Delta/K_bT)$ with Δ=96 cm^{-1}. Below 30°K it deviates from exponential dependence, implying that at low temperatures the ortho- and para-exciton populations are not in thermal equilibrium. Several temperature dependent models for ortho-para conversion have been proposed.[22,23] In chapter VI we present a test of these models by measuring the ortho-para conversion rate as a function of temperature.

C. Raman Scattering[15,24-30]

Resonance Raman scattering is of particular interest in Cu_2O due to the presence of a large number of exciton lines involving electric-dipole and quadrupole transitions and phonon-assisted electric-dipole transitions. The only even parity and hence Raman allowed phonon is the 515 cm^{-1} Γ_{25}^+ phonon, which has been observed in Raman scattering by Compaan and Cummins.[15] They also observed enhancement of the normally forbidden odd parity Raman modes when the laser frequency was in resonance with the electric-quadrupole allowed 1S yellow exciton level.[24] They proposed a Raman scattering mechanism consisting of virtual excitation of the 1S exciton by an electric-quadrupole transition, followed by phonon-assisted electric-dipole emission of the scattered light. The polarization selection rules for these processes have been derived by Birman[25] and studied experimentally by Compaan and Cummins. Although the experimental and theoretical results are in qualitative agreement, there are some quantitative discrepancies which remain to be resolved.

Several groups have used the odd parity phonon Raman scattering as

a quadrupole spectrometer.[26,27] By observing the resonant enhancement of the odd parity Raman modes as a function of the incident laser frequency the energies of quadrupole transitions to higher S and D states of the exciton series can be determined.

Resonant enhancement of multiphonon Raman modes at the 1s yellow and higher levels has also been observed in Cu_2O, and has been studied extensively by Yu and Shen.[10,28] The mechanism for the two-phonon modes involves a phonon-assisted electric dipole transition to the 1S exciton, followed by phonon-assisted emission of the scattered photon. The phonon participation allows 1S excitons of any momentum to be excited, hence, resonant enhancement occurs over a range of incident laser energies above the phonon-assisted absorption edge. Yu and Shen measured the resonant enhancement of the $2\Gamma_{12}^-$ Raman mode at the 1S yellow exciton (Figure 4.5) and found it to be given by:

$$I_{2\Gamma_{12}^-}(\omega_\ell) \propto \alpha(\omega_\ell)\gamma_{rad}/\gamma(E) \tag{4.3}$$

where $\alpha(\omega_\ell)$ is the absorption coefficient at the laser frequency, γ_{rad} is the rate of radiative recombination of the 1S exciton with emission of a Γ_{12}^- phonon, and $\gamma(E)$ is the total rate of decay of the 1S exciton with excess energy $E = \hbar(\omega_\ell - \omega_{1S} - \omega_{12})$. This led Klein[29] to propose that the process being observed was a two-step hot luminescence process consisting of phonon-assisted absorption followed by phonon-assisted emission. Later, Shen [30] pointed out that in a time-resolved experiment resonance Raman scattering and hot luminescence can be distinguished by different decay times. In chapter VII we describe time-resolved measurements aimed at distinguishing between resonant Raman scattering and hot luminescence.

Yu and Shen also observed resonant enhancement of some two-phonon modes around the n=2 to n=6 peaks of the yellow exciton series, and were able to quantitatively explain the enhancement as due to multiple resonances in the scattering process.

Yu and Shen observed multiphonon Raman modes in Cu_2O whose frequencies varied with the laser frequency (Peaks X,Y and Z in Figure 4.6). They determined that these were either three-phonon or four-phonon Raman modes in which one or more of the phonons was a dispersive acoustic phonon. The wavevector and hence the energy of the participating acoustic phonon is determined by the wavevector of the resonantly excited 1S exciton. The exciton energy depends upon the energy of the incident photons, so, the energy of the Raman mode varies with the laser energy. Using this model Yu and Shen were able to explain the observed dispersion, however, they were not able to fit the lineshapes of the Raman lines satisfactorily. This is because they have arbitrarily separated their spectra into Raman scattering and a background due to thermalized luminescence. In chapter V we will show that by considering the spectrum to be entirely due to hot luminescence the shape of these Raman spectra can be fitted quite well.

D. Time-Resolved Measurements[15,31,32]

Very few time-resolved measurements have been made in Cu_2O. Mysyrowicz, Hulin and Antonnetti[31] have determined the para-exciton lifetime to be 13 μs in a naturally occurring crystal. Several groups have attempted to measure the lifetime of the ortho-exciton, but, have been limited by their 1-3 nsec experimental resolution. The short ortho-exciton lifetime relative to that of the para-exciton is somewhat

surprising, but can be understood if the ortho-exciton can decay into the para-exciton. Migus et al[32] have used time-resolved resonant two-photon absorption to set a lower limit of ~1 nsec on the ortho-exciton lifetime at room temperature.

E. Scattering Processes[15,28,33,34]

There are four basic processes by which an ortho-exciton population can relax. They are: (i) elastic intraband scattering processes such as scattering between states of different k, or between different degenerate sublevels; (ii) inelastic intraband scattering of excitons by phonons; (iii) interband scattering, of excitons from the ortho- to the para-exciton level and (iv) recombination. Work on processes (iii) and (iv) in Cu_2O has already been discussed in sections B and D respectively. Elastic scattering (process (i)) is presumably due to impurities, but no studies have been made in Cu_2O. Acoustic phonon scattering in Cu_2O (process (ii)) is quite well understood. From the linewidth of one-phonon resonant Raman scattering Habiger and Compaan[15] determined the exciton-acoustic phonon scattering rate at k=0. More recently, Trebin et al[33] have determined the acoustic deformation potential for Cu_2O from optical measurements of uniaxially stressed crystals. In the appendix we have derived expressions for the acoustic phonon scattering rates using the theory developed by Toyazawa.[34] The relative magnitudes for exciton scattering by different optical phonons have been determined from three-phonon resonant Raman scattering measurements by Yu and Shen.[28] The absolute magnitudes are not yet known.

The following chapters describe experiments to measure different

aspects of the time-dependence of the Cu_2O spectrum, however, all of these measurements were performed with one goal, that of understanding the dynamics of exciton scattering in Cu_2O.

The organization of the rest of this thesis is as follows: Chapter V describes nonthermalized luminescence in Cu_2O, which occurs as a result of competition between intraband acoustic phonon scattering and non-radiative recombination. Chapter VI describes our study of ortho- to para-exciton conversion in Cu_2O. We also touch upon recombination of bound excitons in this chapter. Time-dependent measurements of the resonant Raman lines in Cu_2O are presented in chapter VII.

Table 4.1

Phonon energies (cm^{-1}) of Cu_2O obtained by various techniques.

Symmetry assignment of phonons	Infrared[a] Absorption (300°K)	Optical[b] Absorption	Raman[c] Scattering
Γ_{25}^-		88	86
Γ_{12}^-		110	109
Γ_{15}^-1(TO)	146.3		153
Γ_{15}^-1(LO)	149.3		
Γ_2^-			350
Γ_{25}^+			515
Γ_{15}^-2(TO)	609		635
Γ_{15}^-2(LO)	638		665

[a]P. Dawson, M. M. Hargrave, and G. R. Wilkinson, J. Phys. Chem. Solids 34, 2201 (1973).

[b]S. Brahms and M. Cardona, Solid State Commun. 6, 733 (1968).

[c]P. Y. Yu, Y. R. Shen, Y. Petroff and L. M. Falicov, Phys. Rev. Lett. 30, 283 (1973).

Table 4.1 (continued)

Symmetry assignment of phonons	Luminescence[d]	Theoretical[e] calculation	Neutron[f] scattering
Γ_{25}^{-}	87	98.6	87
Γ_{12}^{-}	110	110	105
$\Gamma_{15}^{-}1$(TO)	152	143	146
$\Gamma_{15}^{-}1$(LO)	154.4	159	
Γ_{2}^{-}	350	307	347
Γ_{25}^{+}	515	549	
$\Gamma_{15}^{-}2$(TO)	633	608	
$\Gamma_{15}^{-}2$(LO)	662	639	

[d] Y. Petroff, P. Y. Yu and Y. R. Shen, Phys. Rev. B 12, 2488 (1975).

[e] C. Carabatos and B. Prevot, Phys. Status Solidi 44, 701 (1971).

[f] M. M. Beg and S. M. Shapiro, Phys. Rev. B 13, 1728 (1976).

Table 4.2

Luminescence Peaks in Cu_2O at 4.2°K (from Reference 11).

Peak Energy (cm^{-1})	Identification
16,400	Ortho-exciton
16,315	Ortho - Γ_{25}^- phonon
16,293	Ortho - Γ_{12}^-
16,250	Ortho - Γ_{15}^-
16,219	Para - Γ_{25}^-
16,200	Ortho - $\Gamma_{12}^- - \Gamma_{25}^-$
16,179	Ortho - $2\Gamma_{12}^-$
16,089	Ortho - $2\Gamma_{12}^- - \Gamma_{25}^-$
16,067	Ortho - $3\Gamma_{12}^-$
16,052	Ortho - Γ_2^-
15,888	Ortho - Γ_{25}^+
15,770	Ortho - $\Gamma_{15}^-(2)$ (TO)
15,740	Ortho - $\Gamma_{15}^-(2)$ (LO)
15,709	Extrinsic

Table 4.2 (Continued)

15,421	Extrinsic
15,237	Extrinsic
15,217	Extrinsic

REFERENCES

1. S. Nikitine, in Optical Properties of Solids, edited by S. Nudelman and S. S. Mitra (Plenum, New York, 1969).
2. V. T. Agekayan, Phys. Status Solidi A 43, 11 (1977).
3. R. W. Baumeister, Phys. Rev. 121, 359 (1961).
4. R. J. Elliot, Phys. Rev. 124, 340 (1961).
5. E. F. Gross and A. A. Kaplyanskii, Fiz. Tverd. Tela 2, 379 (1960) [Sov. Phys. Solid State 2, 353 (1960)].
6. J. P. Dahl and A. C. Switendick, J. Phys. Chem. Solids 27, 931 (1966).
7. L. Kleinman and K. Mednick, Phys. Rev. B 21, 1549 (1980).
8. See for example, P. Dawson, M. M. Hargreave and G. R. Wilkinson, J. Phys. Chem Solids 34, 2201 (1973).
9. S. Brahms and M. Cardona, Solid State Commun. 6, 733 (1968).
10. P. Y. Yu and Y. R. Shen, Phys. Rev. B 12, 1377 (1975).
11. Y. Petroff, P. Y. Yu and Y. R. Shen, Phys. Rev. B 12, 2488 (1975).
12. M. M. Beg and S. M. Shapiro, Phys. Rev. B 13, 1728 (1976).
13. C. Carabatos and B. Prevot, Phys. Status Solidi 44, 701 (1971). See also K. Huang, Z. Phys. 171, 213 (1963) and C. Carabatos, Phys. Status Solidi 37, 773 (1970).
14. A. Compaan and H. Z. Cummins, Phys. Rev. B 6, 4753 (1972).
15. R. M. Habiger and A. Compaan, Sol. State Commun. 18, 1531 (1976).
16. D. Hulin, A. Mysyrowicz and C. Benoit a la Guillaume, Phys. Rev. Lett. 45, 1970 (1980).
17. Y. Petroff, P. Y. Yu and Y. R. Shen Phys. Rev. Lett. 29, 1558 (1972).

18. F. I. Kreingol'd and V. L. Makarov, Fiz. Tverd, Tela, 15, 1307 (1973) [Sov. Phys. Sol. State 15, 890 (1973)].

19. E. F. Gross, F. I. Kreingol'd and V. I. Makarov, ZhETF Pis Red. 15, 383 (1972) [JETP Lett. 15, 269 (1972)].

20. G. Kuwabara, M. Tanaka and H. Fukutani, Solid State Commun. 21, 599 (1977).

21. P. D. Bloch and C. Schwab, Phys. Rev. Lett. 41, 514 (1978).

22. A. Mysyrowicz, D. Hulin, and C. Benoit a la Guillaume, J. Lum. 24/25, 629 (1981).

23. N. Caswell and P. Y. Yu, Phys. Rev. B 25, 5519 (1982).

24. A. Compaan and H. Z. Cummins, Phys. Rev. Lett. 31, 41 (1973). See also A. Z. Genack, H. Z. Cummins, M. A. Washington and A. Compaan, Phys. Rev. B 12 2478 (1975).

25. J. L. Birman, Phys. Rev. B 9, 4518 (1974); J. L. Birman, Solid State Commun. 13, 1189 (1973).

26. M. A. Washington, A. Z. Genack, H. Z. Cummins, R. H. Bruce, A. Compaan and R. A. Forman, Phys. Rev. B 15, 2145 (1977).

27. R. G. Waters, F. H. Pollack, H. Z. Cummins, R. H. Bruce and J. Wicksted, in Light Scattering in Solids, ed. J. L. Birman, H. Z. Cummins and K. K. Rebane (Plenum, New York, 1979), p.229.

28. P. Y. Yu and Y. R. Shen, Phys. Rev. B 17, 4017 (1978).

29. M. V. Klein, Phys. Rev. B 8, 919 (1973).

30. Y. R. Shen, Phys. Rev. B 9, 622 (1974).

31. A. Mysyrowicz, D. Hulin and A. Antonetti, Phys. Rev. Lett. 43, 1123 (1979).

32. A. Migus, J. L. MArtin, R. Astier, A. Antonnetti, D. Hulin and A. Mysyrowicz, in Picosecond Phenomena II, edited by R. M.

Hochstrasser, W. Kaiser and C. V. Shank (Springer-Verlag Berlin, Heidelberg, New York 1980).

33. H. R. Trebin, H. Z. Cummins and J. L. Birman, Phys. Rev. B 23, 597 (1981); R. G. Waters, F. H. Pollak, R. H. Bruce and H. Z. Cummins, Phys. Rev. B 21, 1665 (1980).

34. Y. Toyazawa, Prog. Theor. Phys. 20, 53 (1958).

FIGURE CAPTIONS

Figure 4.1 Absorption spectrum of Cu_2O at 4.2°K showing the yellow exciton series and the phonon-assisted absorption edge (from Reference 3).

Figure 4.2 Energy bands in Cu_2O at the zone center.

Figure 4.3 Luminescence spectra of the yellow 1S exciton in Cu_2O for (a) a sample grown by an arc image furnace and (b) a sample grown by oxidation of copper (from Reference 11).

Figure 4.4 Temperature dependence of the Γ_{12}^- phonon-assisted ortho-exciton recombination peak in Cu_2O (from Reference 19). The broken curve is a plot of $\exp(-\Delta/K_bT)$ where $\Delta=96$ cm^{-1}.

Figure 4.5 Raman cross-section of the two Γ_{12}^- (220 cm^{-1}) mode of Cu_2O plotted as a function of incident photon energy (from Reference 10). The broken line is a plot of Equation (4.3) using the theory described in Reference 10.

Figure 4.6 Raman frequency shifts of all of the observed Raman modes of Cu_2O between 190 and 400 cm^{-1} as a function of incident photon energy ω_ℓ (from Reference 10).

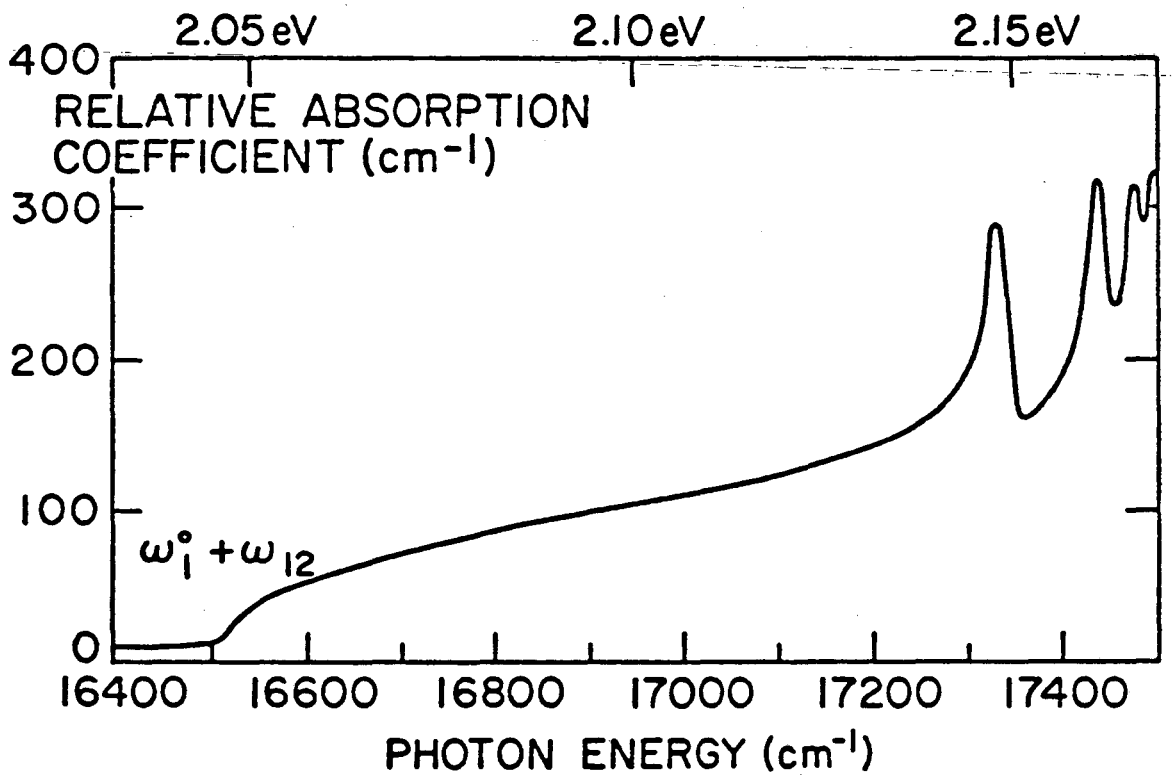
2.05 eV
2.10 eV
2.15 eV
400
RELATIVE ABSORPTION
COEFFICIENT (cm⁻¹)
300
200
100
0
$\omega_1^\circ + \omega_{12}$
16400
16600
16800
17000
17200
17400
PHOTON ENERGY (cm⁻¹)

Figure 4.1

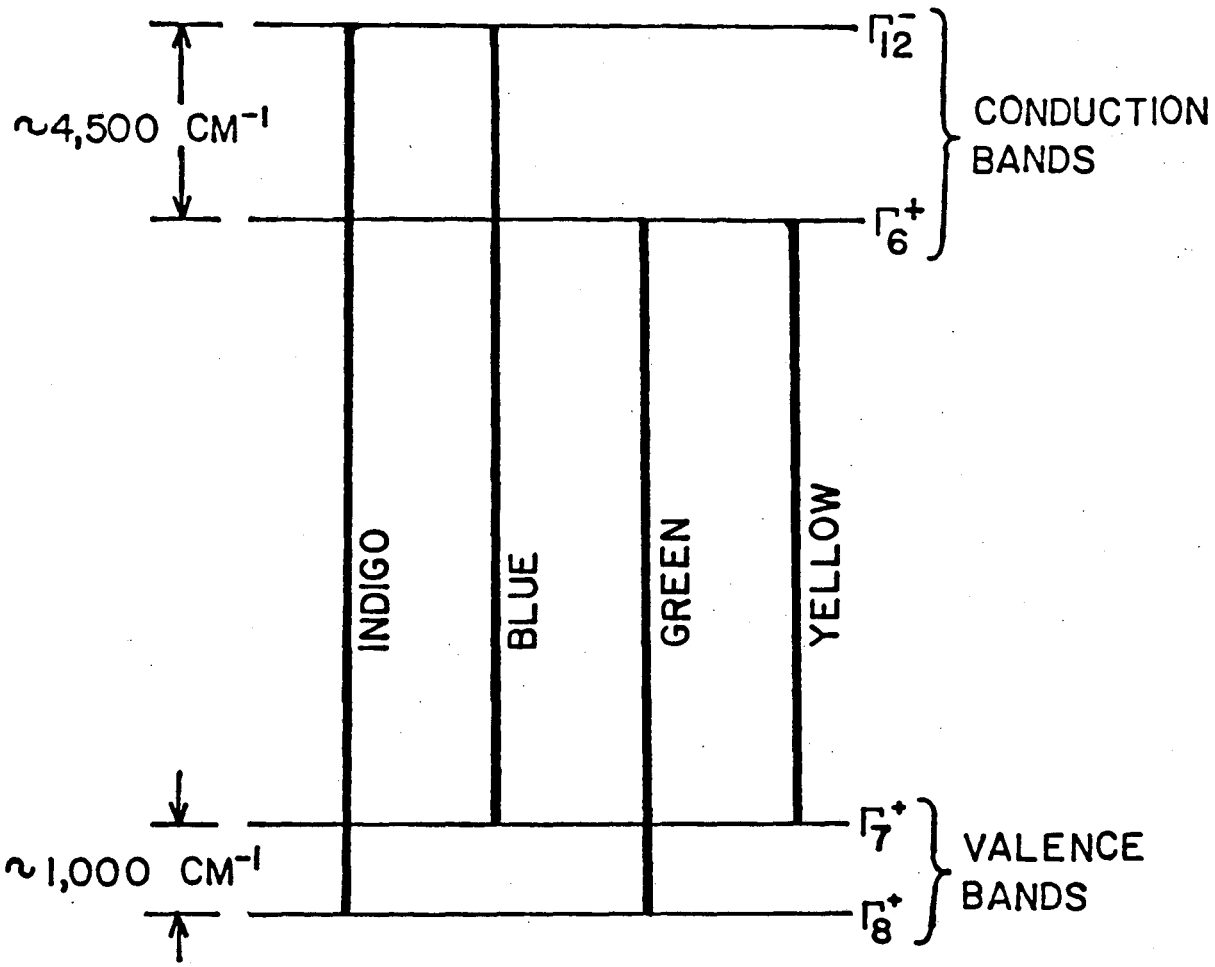
~4,500 CM⁻¹
~1,000 CM⁻¹
Γ12⁻
Γ6⁺
Γ7⁺
Γ8⁺
CONDUCTION BANDS
VALENCE BANDS
INDIGO
BLUE
GREEN
YELLOW

Figure 4.2

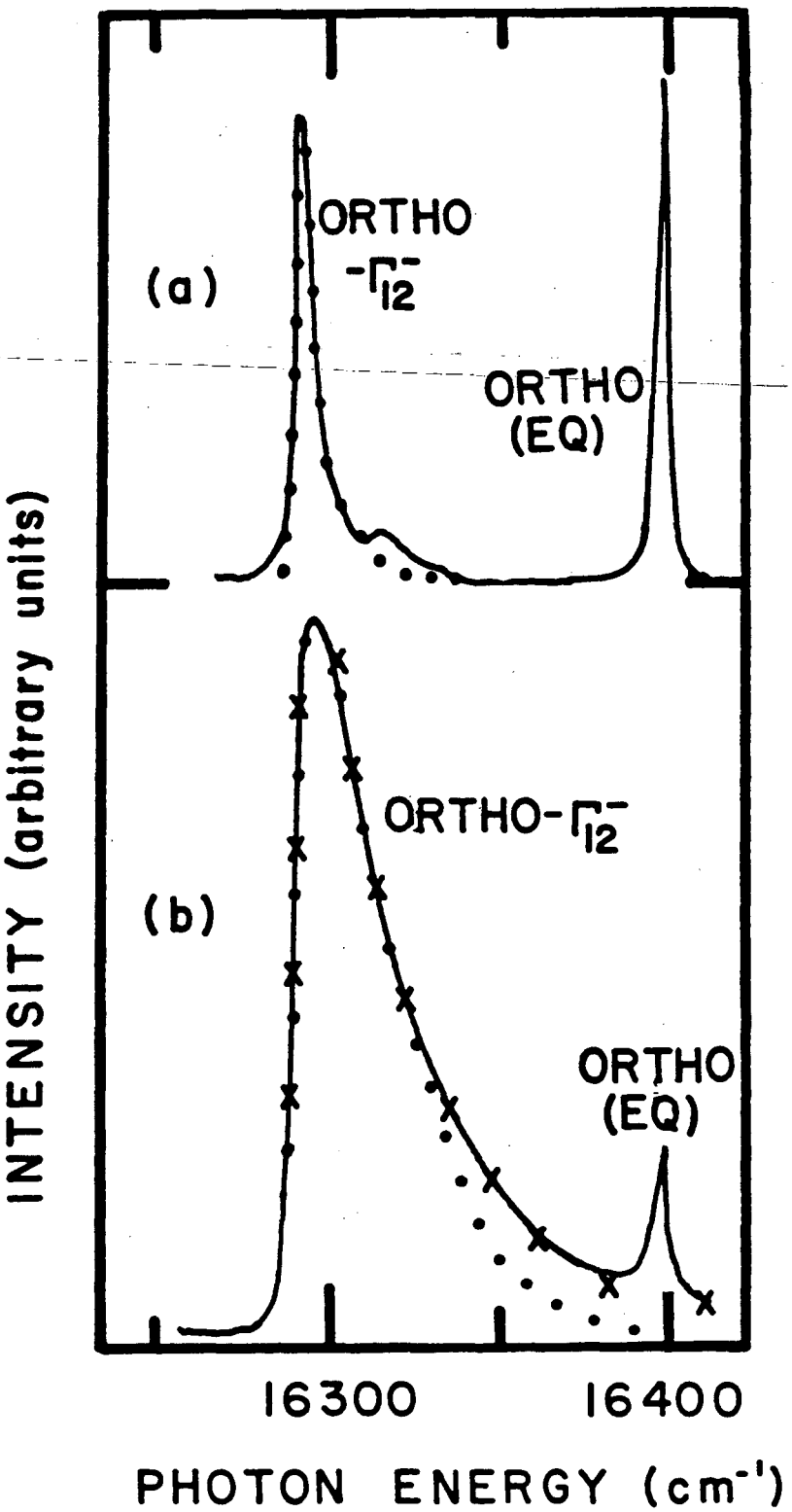
ORTHO
$-\Gamma_{12}^-$
(a)
ORTHO
(EQ)
ORTHO-Γ_{12}^-
(b)
ORTHO
(EQ)
INTENSITY (arbitrary units)
16300
16400
PHOTON ENERGY (cm^{-1})

Figure 4.3

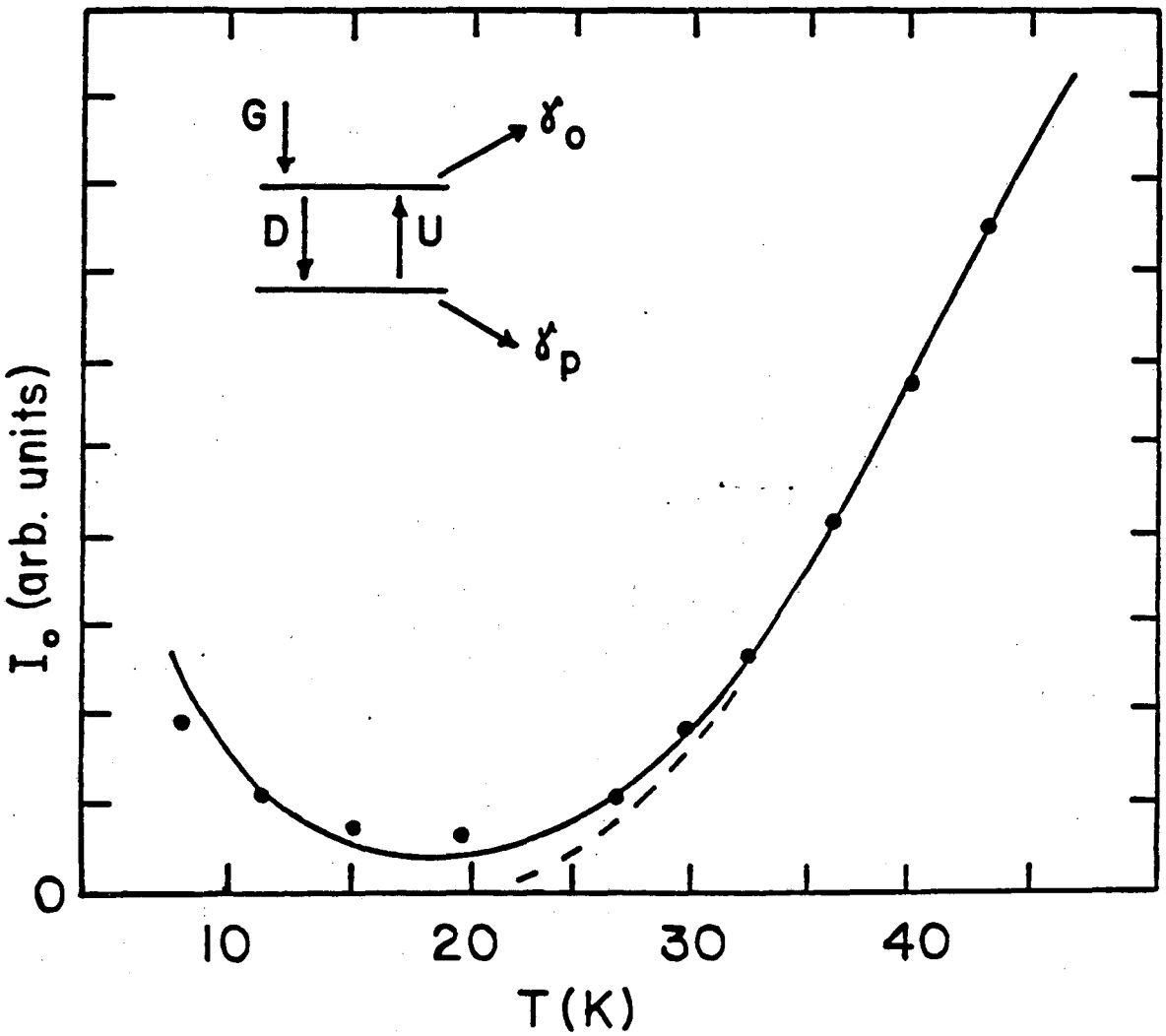

Figure 4.4

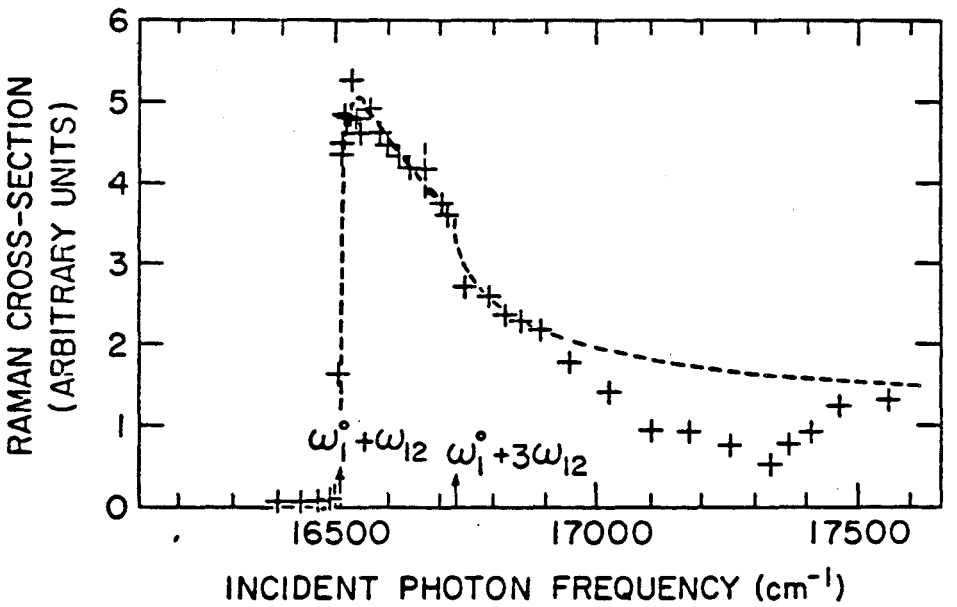
RAMAN CROSS-SECTION
(ARBITRARY UNITS)
0
1
2
3
4
5
6
16500
17000
17500
INCIDENT PHOTON FREQUENCY (cm⁻¹)
ω°1+ω12
ω°1+3ω12

Figure 4.5

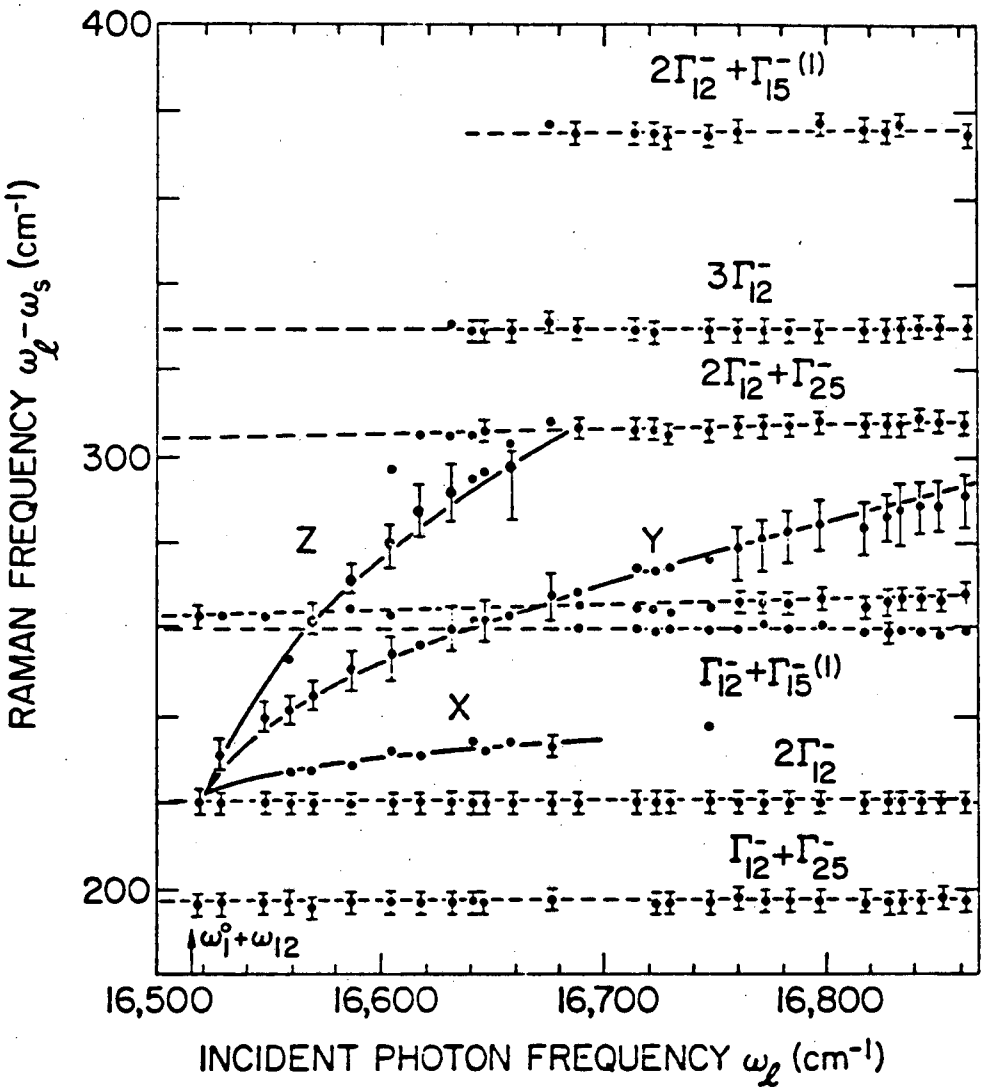
400
300
200
RAMAN FREQUENCY $\omega_\ell - \omega_s$ (cm^{-1})
$2\Gamma_{12}^- + \Gamma_{15}^-(1)$
$3\Gamma_{12}^-$
$2\Gamma_{12}^- + \Gamma_{25}^-$
Z
Y
X
$\Gamma_{12}^- + \Gamma_{15}^-(1)$
$2\Gamma_{12}^-$
$\Gamma_{12}^- + \Gamma_{25}^-$
$\omega_1^\circ + \omega_{12}$
16,500
16,600
16,700
16,800
INCIDENT PHOTON FREQUENCY ω_ℓ (cm^{-1})

Figure 4.6

V. NONTHERMALIZED LUMINESCENCE SPECTRA IN Cu_2O

In this chapter we describe our experimental investigation of photoluminescence due to a non-thermalized distribution of excitons in Cu_2O. Phenomena associated with a non-thermal equilibrium distribution of carriers occur in many semiconductors. In particular, such effects are well known in the photoluminescence spectra of amorphous[1] and heavily doped[2] semiconductors, and in the polariton fluorescence spectra of high purity semiconductors.[3,4] These spectra contain information about various relaxation processes affecting the carriers which is lost once thermalization occurs. Cu_2O is an ideal material in which to study nonthermalized luminescence because its emission spectrum has many of the features common to the more complex systems, while its properties are better known. For example, we have been able to obtain good agreement between theory and experiment using a minimum of adjustable parameters, and from these parameters we have deduced the exciton non-radiative lifetime and effective mass. In addition, the present theory resolves the discrepancy between experiment and the previous theory of Yu and Shen[5] with regard to the lineshape of some resonant Raman peaks in Cu_2O.

A. Photoluminescence Spectrum of Cu_2O[6-8]

Photoluminescence spectra of Cu_2O due to the yellow ortho-exciton are shown in Figure 5.1. In both curves the excitation frequencies are well above the Γ_{12} phonon-assisted indirect absorption edge at 16,509 cm^{-1}. Although these spectra have been reproduced from Reference 6, we have obtained similar spectra with our samples. The sharp line at 16,400

cm^{-1} is due to direct electric-quadrupole recombination of the ortho-exciton. The broader peak is due to Γ_{12}^- phonon-assisted dipole recombination of the exciton. It is well known[6] that the phonon-assisted peak has two different lineshapes depending upon the sample preparation. Melt-grown and naturally occurring samples show spectra similar to that of Figure 5.1 (a), and are believed to be of good quality, while samples which are produced by oxidation of copper show spectra similar to that shown in Figure 5.1 (b), and are believed to contain many defects.

In Figure 5.1 (a), the lineshape of the phonon-assisted peak is quantitatively explained by assuming that the excitons are in thermal equilibrium with each other. The exciton distribution function $\rho_k(E)$ is assumed to be given by the Boltzmann distribution function $\exp(-E/K_bT_{ex})$, where K_b is the Boltzmann constant and T_{ex} is the exciton temperature. Notice that T_{ex} may be different from the bath temperature. It has been shown from absorption measurements[7] that the exciton-Γ_{12}^- phonon interaction is independent of k, the wavevector of the exciton. As a result, the luminescence intensity $I(\omega_s)$ should be given by:

$$I(\omega_s) \propto g(E)\rho_k(E) \tag{5.1}$$

where the exciton energy E is related to the emission frequency ω_s by $\hbar\omega_s = \hbar\omega_{1S} + E - \hbar\omega_{12}$. $\hbar\omega_{1S}$ and $\hbar\omega_{12}$ are respectively the zone-center exciton and Γ_{12}^- phonon energies. g(E) is the exciton density of states, and was assumed to be proportional to $E^{1/2}$.[6] The points in Figure 5.1 (a) are a plot of Equation (5.1) with T_{ex} = 7 °K while the bath temperature is 1.8 °K. The agreement between theory and experiment is quite satisfactory. Also, the emission lineshape was found to be temperature dependent, but independent of the excitation frequency, as

would be expected from a system in thermal equilibrium.

On the other hand, the lineshape of the Γ_{12}^{-} phonon-assisted peak in Figure 5.1 (b) cannot be fitted satisfactorily by Equation (5.1) with a Boltzmann distribution function. The points in Figure 5.1 (b) are representative of such a fit with T_{ex} adjusted to a rather large value of 26°K. In addition, we have found that this emission spectrum is insensitive to sample temperature for temperatures below 77°K. Also, as the excitation frequency approaches the indirect absorption edge so that the phonon-assisted peak now overlaps the $2\Gamma_{12}^{-}$ Raman peak, the width of the phonon-assisted peak narrows, because its intensity at frequencies above the $2\Gamma_{12}^{-}$ Raman peak decreases.

B. Experiment

The experimental setup has already been described in chapter II. The modelocker was turned off, making the output of the dye laser cw. The dye used was Rhodamine 6G. The laser linewidth was typically 1 cm^{-1}. The sample was immersed in liquid helium at a temperature of 2.17°K. The spectrometer resolution was 2 cm^{-1}. The sample was grown by oxidation of copper in an oxygen atmosphere.

Some representative experimental spectra are shown as solid curves in Figure 5.2. The sharp structures in Figure 5.2 whose emission frequencies vary with the excitation frequency have been identified as resonant Raman peaks by Yu and Shen.[5]

C. Theory

It has been proposed that the behavior of exciton emission spectra as represented by curves in Figure 5.1 (b) and in Figure 5.2 is due to

a nonthermalized exciton distribution caused by an exciton nonradiative lifetime too short for the excitons to attain thermal equilibrium.[2,6] Although this explanation accounts satisfactorily for the increased linewidth and lower integrated intensity of the exciton emission in samples with a large amount of defects (Presumably due to oxygen complexes in Cu_2O.), so far this theory has not been tested quantitatively. We show here that such a theory can indeed account quantitatively for all of the experimental results in Cu_2O.

In order to calculate the nonthermalized luminescence spectra in Figure 5.1(b) and Fig 5.2, we first obtain the exciton distribution function $\rho_k(E)$ from the following rate equation:

$$\left(\frac{d\rho_k}{dt}\right) = \left(\frac{\partial\rho_k}{\partial t}\right)_{in} - \left(\frac{\partial\rho_k}{\partial t}\right)_{out} + \left(\frac{\partial\rho_k}{\partial t}\right)_c - \left(\frac{\partial\rho_k}{\partial t}\right)_r - \left(\frac{\partial\rho_k}{\partial t}\right)_{nr} \qquad (5.2)$$

where k is the exciton wavevector. $\left(\frac{\partial\rho_k}{\partial t}\right)_{in}$ and $\left(\frac{\partial\rho_k}{\partial t}\right)_{out}$ represent, respectively, the rates at which excitons are scattered into and out of the state k by phonons. $\left(\frac{\partial\rho_k}{\partial t}\right)_c$ is the rate of exciton creation due to the incident radiation. $\left(\frac{\partial\rho_k}{\partial t}\right)_r$ is the exciton radiative recombination rate, while $\left(\frac{\partial\rho_k}{\partial t}\right)_{nr}$ is the non-radiative rate due to defects plus the net rate of ortho-exciton to para-exciton conversion.[8]

We numerically solve Equation (5.2) for the steady state solution (i.e., $\left(\frac{d\rho_k}{dt}\right) = 0$) utilizing the following assumptions based on previous optical results:[5,9]

(i) The kinetic energy of the exciton is given by: $E=\hbar^2k^2/2m$, where m is its effective mass.

(ii) Interactions between the ortho-exciton and optical phonons other than the Γ_{12}^- mode can be neglected.

(iii) The Γ_{12}^- phonon is dispersionless.[10]

(iv) $\left(\frac{\partial \rho_k}{\partial t}\right)_r$ and $\left(\frac{\partial \rho_k}{\partial t}\right)_{nr}$ are both independent of k, and furthermore $\left(\frac{\partial \rho_k}{\partial t}\right)_{nr} >> \left(\frac{\partial \rho_k}{\partial t}\right)_r$.

(v) The scattering of excitons by the transverse acoustic phonon is negligible compared to scattering by the longitudinal acoustic (LA) phonon. The exciton-LA phonon interaction matrix element is assumed to be proportional to $q^{1/2}$, where q is the phonon wave vector. The constant of proportionality depends on the deformation potential and other quantities, which are known for Cu_2O.

(vi) The LA phonon dispersion is isotropic and is given by $\omega_{LA} = vq$, where v is the LA phonon velocity.

The scattering rate $\left(\frac{\partial \rho_k}{\partial t}\right)_{out}$ is obtained by summing the probability of scattering an exciton out of a given initial state into all possible final states. The rate $\left(\frac{\partial \rho_k}{\partial t}\right)_{in}$ is obtained by summing the corresponding probability over all initial states. In the appendix we have derived analytic expressions for $\left(\frac{\partial \rho_k}{\partial t}\right)_{out}$ and $\left(\frac{\partial \rho_k}{\partial t}\right)_{in}$, which are given as Equations (A.5) and (A.6).

Our model can be schematically represented by Figure 5.3. Excitons are created by indirect absorption of the incident phonon (ω_i) at energy $E_c = \hbar\omega_i - \hbar\omega_{12} - \hbar\omega_{1S}$. Those excitons which radiatively recombine without scattering by LA phonons produce the sharp $2\Gamma_{12}^-$ Raman line at $\omega_s = \omega_i - 2\omega_{12}$ described in Reference 5. The rest will either decay nonradiatively or be scattered by LA phonons. Radiative recombination of excitons scattered successively by LA phonons produces the asymmetric peaks below the $2\Gamma_{12}^-$ Raman line in the spectra in Figure 5.2 and

identified as LA phonon sidebands of the $2\Gamma_{12}^{-}$ Raman peak by Yu and Shen. In this simple model, whether a thermalized or non-thermalized emission spectrum is observed is determined entirely by the relative magnitude of the phonon scattering terms $\left(\frac{\partial \rho_k}{\partial t}\right)_{in}$ and $\left(\frac{\partial \rho_k}{\partial t}\right)_{out}$ compared to $\left(\frac{\partial \rho_k}{\partial t}\right)_{nr}$. The phonon scattering terms lead to the establishment of thermal equilibrium among the excitons. However, if $\left(\frac{\partial \rho_k}{\partial t}\right)_{nr}$ is comparable or larger than the phonon scattering rates, then the excitons do not have sufficient time to thermalize before they recombine.

D. Comparison of Theory and Experiment

To obtain the theoretical curves shown as points in Figure 5.2 and as x's in Figure 5.1 (b), the exciton creation rate is assumed to be a delta function $\delta(E - E_c)$. For the exciton-LA phonon matrix element in Cu_2O we use the deformation potential of 2.1 ev which has been determined by Trebin et al[11]. Equations (A.5) and (A.6) for $\left(\frac{\partial \rho_k}{\partial t}\right)_{in}$ and $\left(\frac{\partial \rho_k}{\partial t}\right)_{out}$ involve the kinematic factor mv^2, which determines the position of the subsidiary phonon sideband peaks in Figure 5.2. For v we used the previously determined value of $v=4.5\times10^5$ cm/sec. Yu and Shen have determined m to be 3.0 times the free electron mass m_e. We found a slightly lower value of $(2.7\pm0.1)m_e$ with our theory, but this difference is not significant since it is within the experimental uncertainty. Other than for m and an overall intensity factor, $\left(\frac{\partial \rho_k}{\partial t}\right)_{nr}$ is the only adjustable parameter in the calculation. The theoretical curves in Figure 5.1 (b) and Figure 5.2 are obtained by setting $\left(\frac{\partial \rho_k}{\partial t}\right)_{nr}$ equal to $(3.5\pm0.5)\times10^{10}$ sec^{-1} and convoluting the spectra calculated with Equations (5.1) and (5.2) with a Gaussian spectrometer spectral function (FWHM = 2 cm^{-1}). The value of $\left(\frac{\partial \rho_k}{\partial t}\right)_{nr}$ obtained this way is in good

agreement with the value of $(2\text{-}4)\times10^{10}$ sec^{-1} determined directly from time-resolved photoluminescence.

E. Conclusions

Other than for the small peaks labelled '*', which are due to phonons not considered here, the theory reproduces very well all the salient features of the experimental spectra, including those previously identified by Yu and Shen[5] as due to resonant Raman scattering. In fact, Yu and Shen found that their theoretical lineshapes of the $2\Gamma_{12}^{-}$ + nLA (n=1 and 2) Raman modes are wider than those experimentally observed, while we do not find such discrepancy between our theory and experiment. We conclude that this is because they have arbitrarily decomposed the spectrum into Raman peaks and a luminescence background. Our model shows that in Cu_2O it is not necessary to separate the two because our model includes both in a simple unified manner.[12] We note also the excellent agreement between our theory and the nonthermalized lineshape in Figure 5.1 (b). Thisis the first time such a lineshape has been explained quantitatively in Cu_2O. The thermalized emission spectrum in Figure 5.1 (a) can also be obtained using our model by simply decreasing $\left(\frac{\partial \rho_k}{\partial t}\right)_{nr}$. In Chapter VI we will show that for samples which exhibit thermalized luminescence spectra $\left(\frac{\partial \rho_k}{\partial t}\right)_{nr}$ lies in the range of 10^5 to 10^9 sec^{-1}, much smaller than that of the sample discussed here.

REFERENCES

1. J. Shah and M. A. Bosch, Phys. Rev. Let. 42, 1420 (1979).
2. S. Permogorov and V. Travnikov, Solid State Commun. 29, 615 (1979).
3. See references in H. Sumi, J. Phys. Soc. Jpn. 41, 526 (1976).
4. F. Askary and P. Y. Yu, Solid State Commun. 47, 241 (1983).
5. P. Y. Yu and Y. R. Shen, Phys Rev. B 12, 1377 (1975).
6. Y. Petroff, P. Y. Yu and Y. R. Shen, Phys. Rev. B 12, 2488 (1975).
7. A. Compaan and H. Z. Cummins, Phys. Rev. B 6, 4753 (1972).
8. J. S. Weiner, N. C. Caswell P. Y. Yu, and A. Mysyrowicz, Solid State Commun., 46, 105 (1983).
9. See, for example, S. Nikitine in Optical Properties of Solids, edited by S. Nudelman and S. S. Mitra (Plenum, New York, 1969).
10. M. M. Beg and S. M. Shapiro, Phys. Rev. B 13, 1728 (1976).
11. H. R. Trebin, H. Z. Cummins and J. L. Birman, Phys. Rev. B 23, 597 (1981); R. G. Waters, F. H. Pollack, R. H. Bruce and H. Z. Cummins, Phys. Rev. B 21, 1665 (1980).
12. M. V. Klein, Phys. Rev. B 8, 919 (1973). According to this reference, what we calculate here would be called hot luminescence.

FIGURE CAPTIONS

Figure 5.1 The luminescence spectra of the yellow 1S ortho-exciton in Cu_2O at 1.8°K for (a) a sample grown by an arc image furnace and (b) a sample grown by oxidation of copper. The solid curves are the experimental curves from Reference 6. The solid circles are fits with a Boltzmann distribution and exciton temperatures T_{ex} = 7°K and 26°K respectively for (a) and (b). The points denoted by 'x' are calculated with the model discussed in the text.

Figure 5.2 Luminescence spectra in Cu_2O at 2.1°K as a function of the excitation frequency: (a) 16,547 $cm,^{-1}$ (b) 16,575 $cm,^{-1}$ (c) 16,620 cm^{-1} and (d) 16,678 cm^{-1}. The solid curves are the experimental results while the solid circles are calculated from our model. Peaks denoted as * are due to phonons not included in our present model (See Reference 4 for their identifications).

Figure 5.3 Schematic description of processes included in our calculation of the exciton distribution function. The light arrows denote optical transitions, the dotted arrows denote exciton scattering by Γ_{12}^{-} phonons while the heavy arrows denote exciton scattering by LA phonons. Non-radiative recombinations are represented by a line terminated by an x.

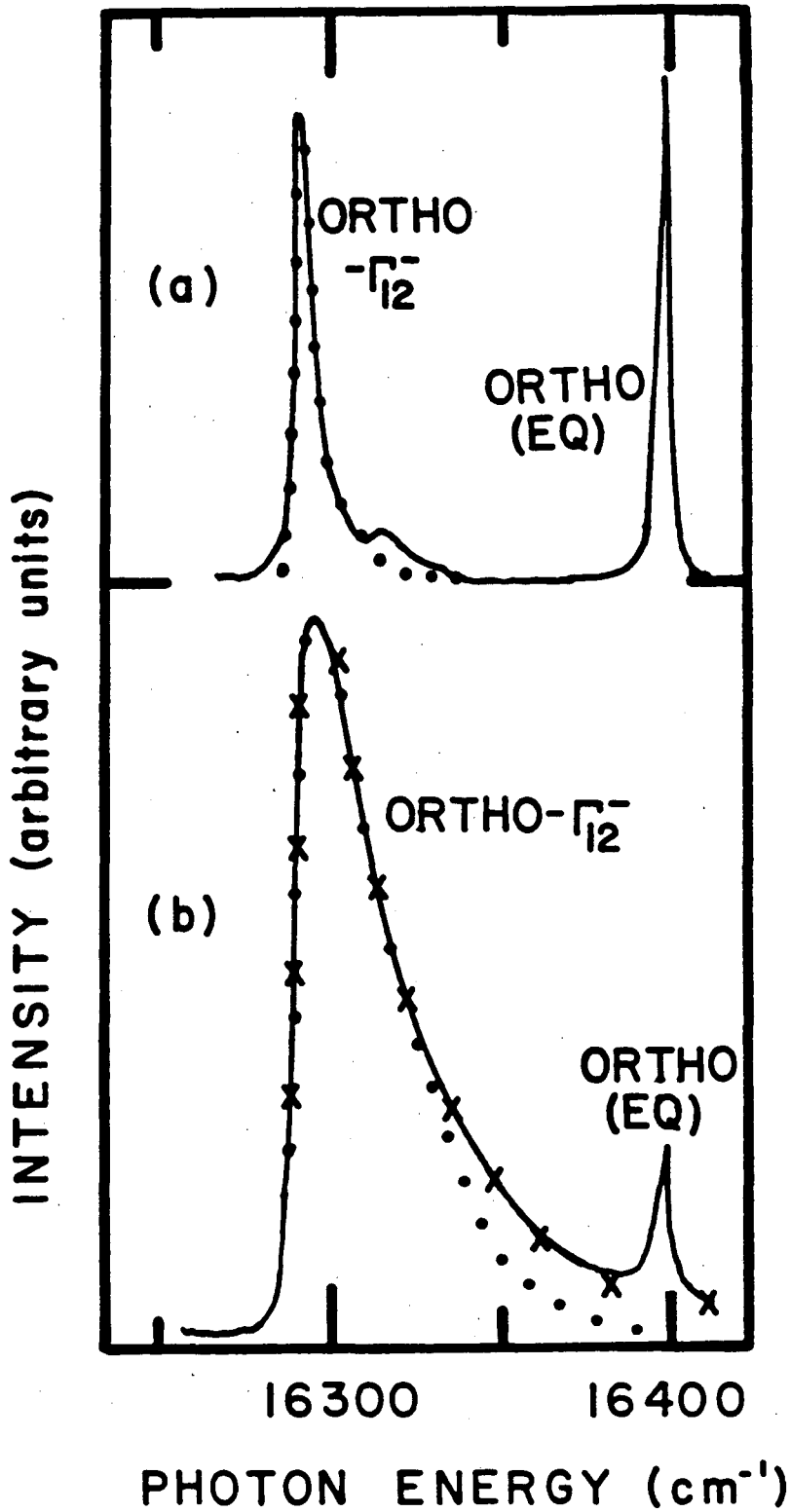
(a)
ORTHO
$-\Gamma_{12}^{-}$
ORTHO
(EQ)
(b)
ORTHO-Γ_{12}^{-}
ORTHO
(EQ)
INTENSITY (arbitrary units)
16300
16400
PHOTON ENERGY (cm^{-1})

Figure 5.1

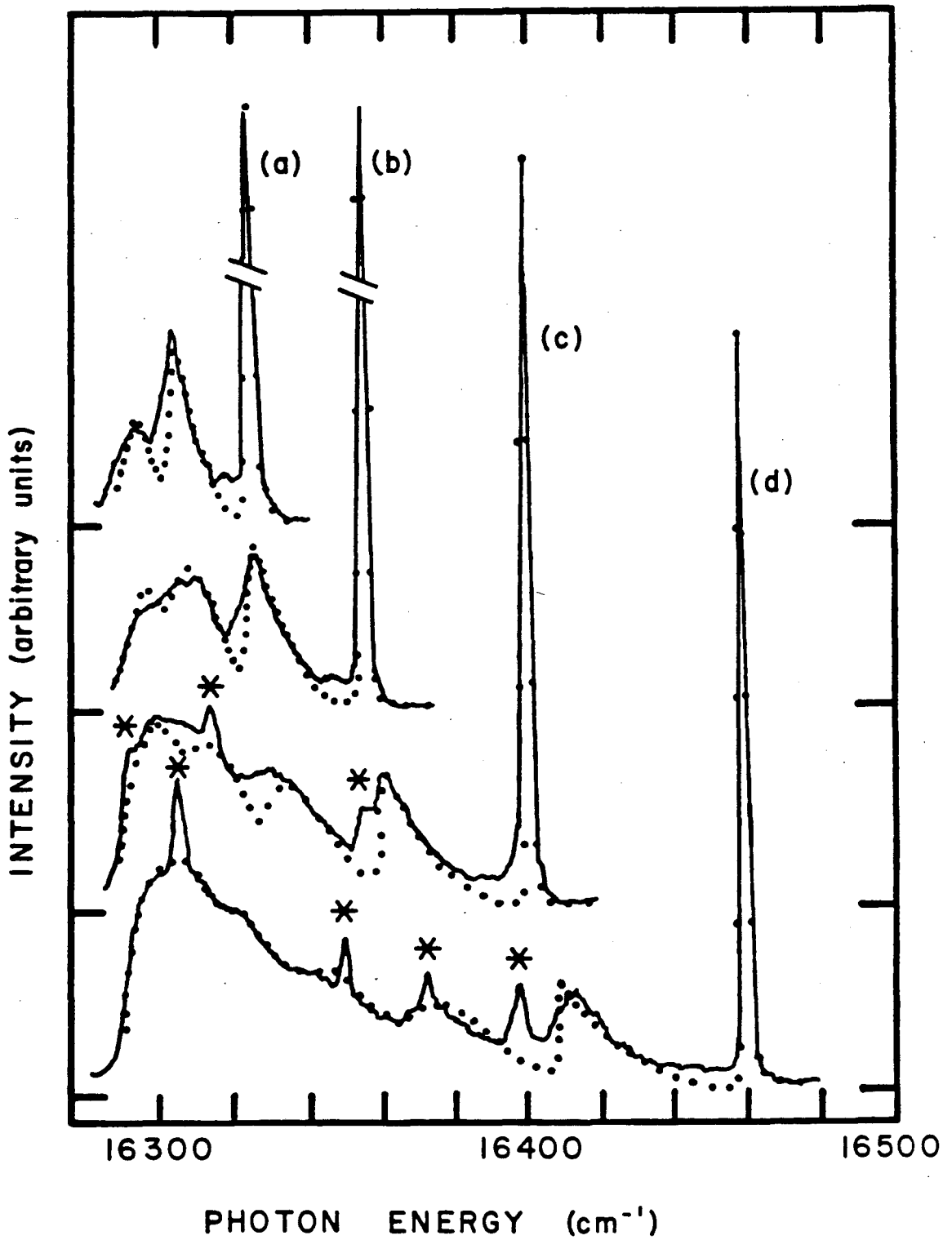
(a)
(b)
(c)
(d)
INTENSITY (arbitrary units)
16300
16400
16500
PHOTON ENERGY (cm⁻¹)

Figure 5.2

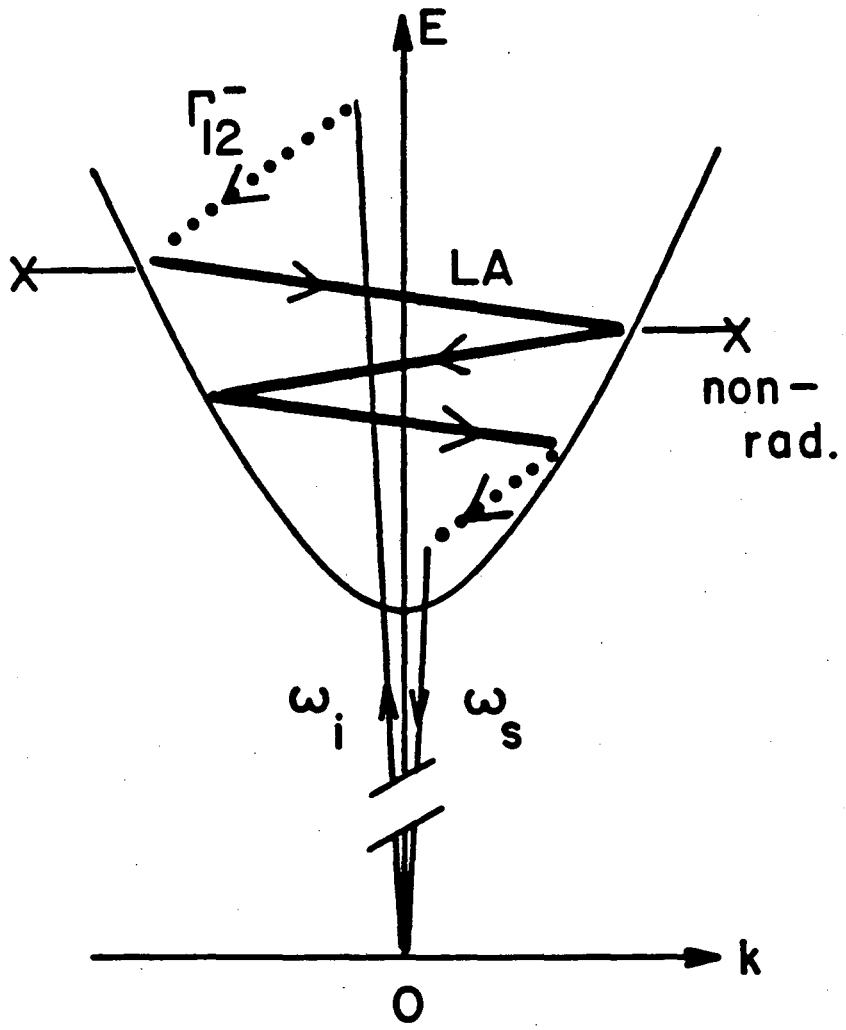

Figure 5.3

VI. EXCITON LIFETIMES IN Cu_2O

In section A of this chapter we describe our measurements of the lifetimes of the ortho-exciton and para-exciton in Cu_2O. Since these levels are electric-dipole forbidden[1] their lifetimes are expected to be quite long. However, previous attempts to measure the ortho-exciton lifetime with nanosecond laser pulses have been unsuccessful.[2,3] Even in the Cu_2O sample with the largest para-exciton lifetime found so far the ortho-exciton lifetime is $\leqslant$ 3 nsec.[3] It has been suggested that the ortho-exciton lifetime is shorter than expected because it is dominated by decay of the ortho-exciton into the lower energy para-exciton level.[3] We have measured the ortho-exciton lifetime in Cu_2O for the first time. By monitoring both the ortho-exciton and para-exciton decays as a function of temperature, we demonstrate that the ortho-exciton lifetime at finite temperatures is indeed dominated by its decay into the para-exciton level. Furthermore, we find that the ortho-para conversion rate increases with temperature approximately as $T^{3/2}$. Our results are important to current efforts to observe Bose-Einstein condensation of excitons in Cu_2O.[4,5]

There are several lines in the spectrum of Cu_2O which exhibit very strong temperature dependence, and thus have been attributed to recombination of bound excitons.[6] In section B we present time dependent measurements on these lines which support this suggestion.

A. Ortho- to Para-Exciton Conversion

Figure 6.1 shows a typical photoluminescence spectrum of Cu_2O. The sharp line at 16,397 cm^{-1} is due to direct electric-quadrupole

recombination of ortho-excitons. The broader peak lying at 16,290 cm^{-1} is due to Γ_{12}^- phonon-assisted recombination of the ortho-exciton, and the weaker but equally broad peak lying at 16,220 cm^{-1} is due to Γ_{25}^- phonon-assisted recombination of the para-exciton.

Gross, Kreingol`d, and Makarov[7] were the first to estimate the relative ordering of the ortho-exciton and para-exciton in Cu_2O. For temperatures greater than 30°K they found that the intensity of the Γ_{12}^- phonon-assisted ortho-exciton recombination peak increases as $\exp(-\Delta E/K_b T)$ with ΔE=12 mev. Based upon this result, they proposed that the ortho-exciton level must lie 12 mev (or 96 cm^{-1}) above the para-exciton. Below 30 °K the ortho-exciton emission intensity deviates from exponential dependence, and exhibits a minimum at 20 °K (Their results are reproduced in Figure 6.2). They explained this behavior qualitatively by proposing that the ortho-exciton and para-exciton are not in thermal equilibrium at temperatures below 30 °K. But as the temperature increases above 30°K the ortho- to para-exciton conversion rate becomes fast enough for the two to reach thermal equilibrium before recombining. Recently, two temperature dependent models for the ortho- to para-exciton conversion mechanism have been proposed.[5,8] Both are capable of explaining the experimental temperature dependence of the ortho-exciton luminescence intensity. We present a direct test of these two models by measuring the ortho- to para-exciton conversion rate as a function of temperature.

1. Experiment

We determine the ortho-para conversion rate in Cu_2O by exciting the ortho- and para-exciton emissions and then monitoring their decay. The

experimental setup has already been described in chapter II. The laser frequency is chosen to be 16,800 cm^{-1}, which is well below the 2S exciton at 17,378 cm^{-1}, so that only 1S excitons are excited.

It is known that Cu_2O samples can be divided into two types depending upon their luminescence lineshape.[6] Those which show nonthermalized luminescence have extremely short (Less than 100 psec) luminescence lifetimes,[9] presumably due to the presence of many defects,[10] so we have performed our experiments on two samples which exhibited thermalized lineshape. One is a melt-grown bulk crystal,[11] while the other is a high quality natural single crystal.[3] By fitting the time-averaged luminescence lineshape with the expression $E^{1/2}\exp(-E/K_bT)$ where E is the exciton energy, K_b is the Boltzmann constant, and T is the exciton temperature, we can determine the temperatures of the ortho- and para-exciton.[8] At all temperatures, we found that the exciton temperatures are very close to the lattice temperature measured by a calibrated thermometer mounted next to the sample. Furthermore, we determined from time-resolved measurements that the excitons reached the lattice temperature in less than 100 psec.

Figure 6.3(a-c) shows the decay in time of the Γ_{12}^- phonon-assisted ortho-exciton emission peak, and of the Γ_{25}^- phonon-assisted para-exciton emission peak at three temperatures. We note that at low temperatures the ortho-exciton decays exponentially with a single time-constant. At $T \geq 10^{\circ}K$ the decay seems to have two time constants: a slow one and a fast one. The amplitude of the fast decaying component, relative to that of the slow decaying component, becomes smaller with increase in temperature, while its decay rate becomes faster. For $T>50^{\circ}K$ the slow component dominates over the fast component, so the ortho-exciton again

decays with a single time constant. In contrast to the ortho-exciton decay, the para-exciton decay is independent of temperature. We note that at $T>50^{\circ}K$ both the ortho-exciton and para-exciton decay at the same rate.

The results obtained in both samples are qualitatively similar. The main difference lies in the para-exciton decay rate. In the melt-grown sample the para-exciton lifetime is 10 nsec, while in the high qualitiy natural crystal the para-exciton lifetime is 13 μsec.[3] The lifetime of the ortho-exciton at $T=2.5^{\circ}K$ is about twice as long in the natural crystal as that of the melt-grown crystal, but this difference disappears at higher temperatures.

2. Theory

The time-dependence of the ortho- and para-exciton luminescence can be understood in terms of the two level mode shown in the inset of Figure 6.2. We assume that the ortho- and para-exciton scatter into each other at the rates D and U which are temperature dependent. N_o, G_o, and γ_o are respectively the distribution function, generation rate, and recombination rate of the ortho-exciton. The corresponding quantities for the para-exciton are represented by N_p, G_p, and γ_p. $N_o(t)$ and $N_p(t)$ can be obtained by solving the rate equations:

$$g_o\dot{N}_o = -g_oN_oD + g_pN_pU - \gamma_og_oN_o + G_o(t) \tag{6.1}$$

$$g_p\dot{N}_p = -g_pN_pU + g_oN_oD - \gamma_pg_pN_p + G_p(t) \tag{6.2}$$

where the degeneracies of the ortho- and para-exciton levels, g_o and g_p, are respectively three and one. By assuming that the generation rates $G_o(t)$ and $G_p(t)$ are both delta functions and that $U<<(\gamma_o,\gamma_p)<D$ the

solutions for $N_o(t)$ and $N_p(t)$ are given approximately by:

$$g_oN_o(t) = g_oN_o(0)e^{-(D+\gamma_o)t} + g_p(U/D)(g_oN_o(0) + g_pN_p(0))e^{-\gamma_p t} \quad (6.3)$$

$$g_pN_p(t) = -g_pN_p(0)(D/(D+\gamma_o))e^{-(D+\gamma_o)t} + (g_oN_o(o) + g_pN_p(0))e^{-\gamma_p t} \quad (6.4)$$

The first terms in Equations (6.3) and (6.4) represent respectively, the decay of the excess population of ortho-excitons and the corresponding buildup of the para-excitons. The factor $(D/(D+\gamma_o))$ is the branching ratio for the ortho-para transition. As the para-exciton population builds up, the two excitons will eventually reach thermal equlibrium with $N_o(t)/N_p(t) = g_pU/(g_oD) = e^{-\Delta E/K_bT}$, and both levels will decay as $e^{-\gamma_p t}$ for $t \to \infty$.

3. Comparison of Theory and Experiment.

Our results can be understood in terms of the two level model of section 2. The initial fast decay of the ortho-exciton luminescence corresponds to the decay of the nonequilibrium ortho-exciton population. The slow ortho-exciton decay is due to the decay of the ortho-exciton population which is now in thermal equilibrium with the para-exciton population. According to Equation (6.3), therefore, the first decay rate of N_o should be given by $\gamma_o + D$, while the slow decay rate of N_o should be equal to γ_p, and should be the same as that of N_p. In practice, we found that, for $T<40^\circ K$, N_o and N_p did not reach thermal equilibrium with each other within the laser pulse separation of 12 nsec.

By convoluting Equations (6.3) and (6.4) with the instrument response and using $\gamma_o + D$ and γ_p as adjustable parameters, we fit the experimental $N_o(t)$ curves to extract the fast decay rate $D + \gamma_o$ as a function of temperature. The resultant values of $D + \gamma_o$ are plotted

as open circles in Figure 6.4. The large uncertainty in $D + \gamma_o$ at high temperatures is due to the combined effect of the instrument resolution and the smaller relative amplitude of the fast decaying component at higher temperatures.

The striking result in Figure 6.4 is the strong temperature dependence of $D + \gamma_o$. Since γ_o is presumably due to the recombination of the ortho-excitons at defects and hence temperature independent, the strong temperature effect must be attributed to D. This is supported by the temperature independence of γ_p, and by the similar temperature dependence of $D + \gamma_o$ for the two samples having very different values of γ_p.

Caswell and Yu have proposed a physical model for the ortho-para conversion mechanism based on two-phonon scattering.[8] The result of their calculation is shown as the broken line in Figure 6.4. It is clear that their theory predicts a much stronger temperature dependence in D than we observed. Our results can be fitted quite well by the expression: $a + bT^{3/2}$ where $a=4\times10^8$ sec^{-1} and $b = 0.3\times10^8$ sec^{-1}, while the theoretical curve approaches $T^{7/2}$ instead.

As alternate explanations, we have considered the following mechanisms: (a) defects such as paramagnetic impurities, (b) combinations of phonons and defects; and (c) exciton-exciton interaction. Mechanisms (a) and (b) tend to give temperature dependence weaker than $T^{3/2}$ and in addition their contributions to D would presumably vary greatly between the two samples. We have been able to rule out mechanism (c) by varying the excitation intensity. We found that the ortho-exciton lifetime did not show any dependence upon excitation intensity, although the para-exciton lifetime does decrease

with higher intensity.

B. Bound Excitons

1. Previous Work.

Figure 6.5 Shows the photoluminescence spectrum of our meltgrown sample at a temperature of 2.2°K. We note the presence of two lines labelled F and F' which are not observed at higher temperatures. These lines have been studied in CW measurements by Petroff et al,[6] who made the following observations:

(i) The positions of the lines suggest that F and F' are due to recombination of the ortho-exciton with the assistance of the $\Gamma_{12}^- + \Gamma_{25}^-$ and $2\Gamma_{12}^-$ phonons respectively, however, such processes are forbidden by symmetry and the lines do not have the shapes characteristic of phonon-assisted luminescence.

(ii) The line intensities show strong temperature dependence, and also, saturate quickly with high laser intensities. In comparison, the zero phonon and phonon-assisted ortho-exciton lines exhibit linear dependence upon incident intensity.

(iii) The excitation spectrum of F and F' is similar to that of the other luminescence peaks.

Petroff et al proposed on the basis of these observations that the F and F' lines are due to recombination of weakly bound ortho-excitons with the assistance of the $\Gamma_{12}^- + \Gamma_{25}^-$ and $2\Gamma_{12}^-$ phonons respectively.

2. Results and Discussion.

The modelocked dye laser frequency was tuned to 16,517 cm^{-1} for exciting the F and F' lines and their time-dependence was measured.

Figure 6.6 shows only the decay of the F peak, however, both peaks exhibited the same time-dependence. The solid line in Figure 6.6 is the decay of the ortho-exciton luminescence peak at 16,290 cm^{-1}. Both peaks clearly exhibit the same decay behavior.

This result can be understood with Petroff et al's model. If we assume that K_bT is comparable to the binding energy of the weakly trapped excitons, then the bound exciton population will be in thermal equilibrium with the free exciton population and both will exhibit the same decay. A strongly bound ortho-exciton with a lifetime much shorter than that of the ortho-exciton can also have the same decay time as the ortho-exciton if the bound exciton population is controlled by the ortho-exciton population, however, this model would not explain the strong temperature dependence which has been observed. Thus, the time-dependent measurements support the identification of the F and F' lines as due to bound excitons in Cu_2O.

C. Conclusions

We have shown that the ortho-exciton lifetime at finite temperatures is dominated by its conversion to the para-exciton. We have been able to explain the time decay of ortho-exciton and para-exciton photoluminescence spectra using a simple two-level model and have shown that the decay rate of ortho-excitns into para-excitons increases with temperature as $T^{3/2}$. None of the currently existing theories seem to be able to explain this time dependence.

From our measurements of the decays of the F and F' lines we have confirmed that these lines are due to phonon-assisted recombination of weakly bound ortho-excitons.

REFERENCES

1. See for example S. Nikitine in Optical Properties of Solids, edited by S. Nudelman and S. S. Mitra (Plenum, New York, 1969).
2. R. M. Habiger and A. Compaan, Solid State Commun. 18, 1531 (1976).
3. A. Mysyrowicz, D. Hulin and A. Antonetti, Phys. Rev. Lett., 43, 1123 (1979).
4. D. Hulin, A. Mysyrowicz and C. Benoit a la Guillaume, Phys. Rev. Lett. 45, 1970 (1980).
5. A. Mysyrowicz, D. Hulin and C. Benoit a la Guillaume, J. Lum. 24/25 629 (1981).
6. Y. Petroff, P. Y. Yu and Y. R. Shen, Phys. Rev. B 12, 2488 (1975).
7. E. F. Gross, F. I. Kreingol'd and V. L. Makarov, Sov. J. Exp. Theor. Phys. Lett. 15, 269 (1972); F. I. Kreingol'd and V. L. Makarov, Fiz. Tverd. Tela. 15, 3107 (1973) [Sov. Phys.-Solid State 15, 890 (1973).]
8. N. Caswell and P. Y. Yu, Phys. Rev. B 25, 5519 (1982).
9. See Chapter 4.
10. N. Caswell, J. S. Weiner and P. Y. Yu, Solid State Commun. 40, 843 (1981).

11. We thank Professor Y. R. Shen for the loan of the melt-grown sample.

FIGURE CAPTIONS

Figure 6.1 Photoluminescence spectrum of Cu_2O at a temperature of 26°K.

Figure 6.2 Temperature dependence of the Γ_{12}^- phonon-assisted ortho-exciton peak in Cu_2O. Experimental points are from Reference 7. Solid line is the result of a theoretical model calculation presented in Reference 9. The inset is the schematic diagram of the two-level model discussed in the text.

Figure 6.3 Time-dependent decay of the ortho- and para-exciton luminescence peaks at three different temperatures: (a) 2.5 °K, (b) 35°K, and (c) 48°K. The ortho- and para-exciton curves have been displaced from each other for clarity. The curve labelled 'laser' in (a) represents the instrument response to a dye laser pulse of width ~10 psec.

Figure 6.4 The fast decay rate of the ortho-exciton plotted as a function of temperature. The open circles are experimental points deduced from the luminescence decay curves. The solid line is a plot of the expression $a + bT^{3/2}$, while the broken curve is calculated from the two-phonon mechanism proposed in Reference 8.

Figure 6.5 Luminescence spectrum of Cu_2O at a temperature of 2.2°K. The peaks labelled F and F' are believed to be due to recombination of weakly bound ortho-excitons with the assistance of $\Gamma_{12}^- + \Gamma_{25}^-$ and $2\Gamma_{12}^-$ phonons respectively.

Figure 6.6 Luminescence decay of the F line at a temperature of 2.2°K. The dots are the time-decay of the F line and the solid line is the time-decay of the ortho-exciton peak.

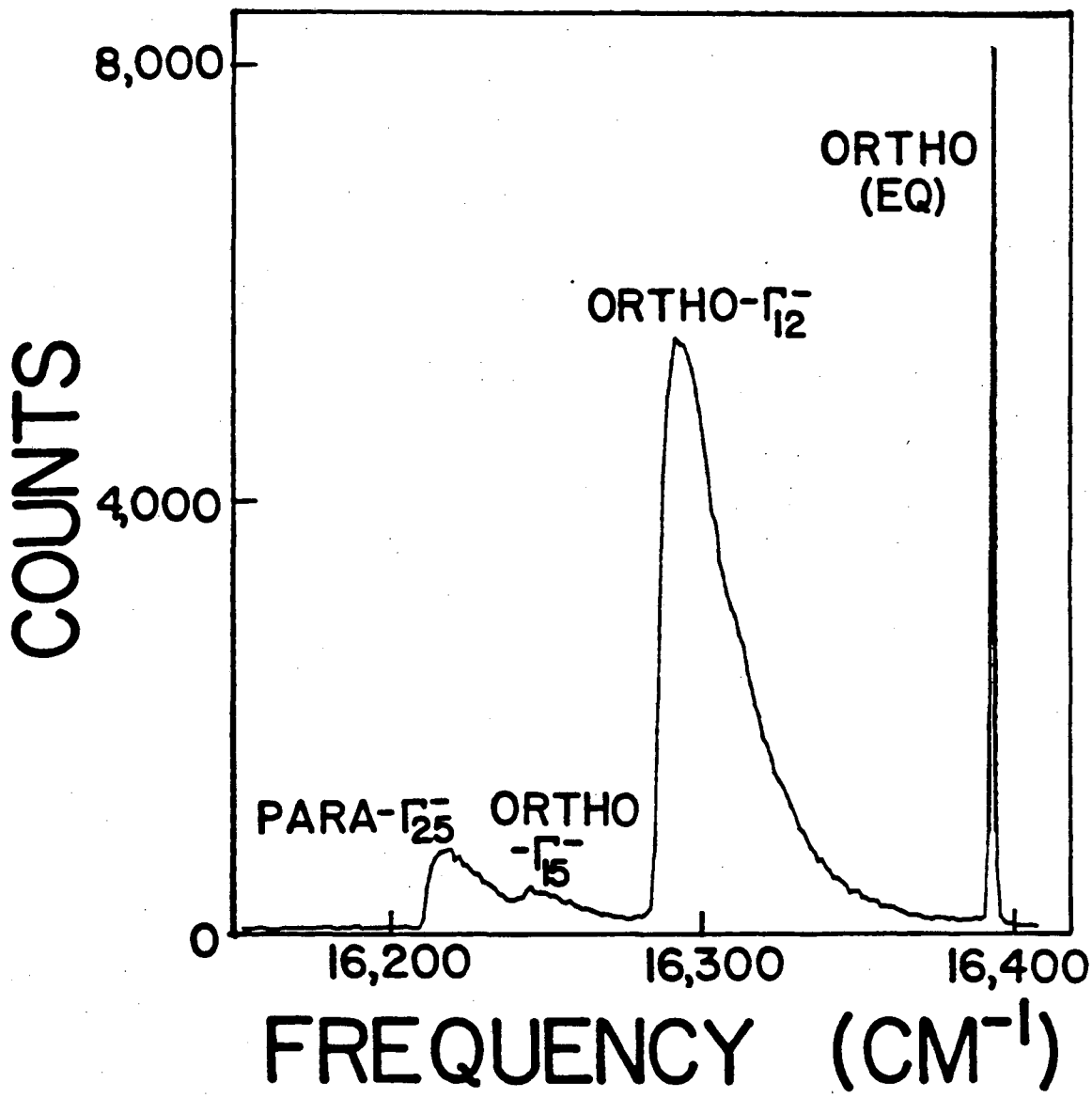
8,000
4,000
0
COUNTS
ORTHO
(EQ)
ORTHO-Γ_{12}^-
PARA-Γ_{25}^-
ORTHO
-Γ_{15}^-
16,200
16,300
16,400
FREQUENCY (CM^{-1})

Figure 6.1

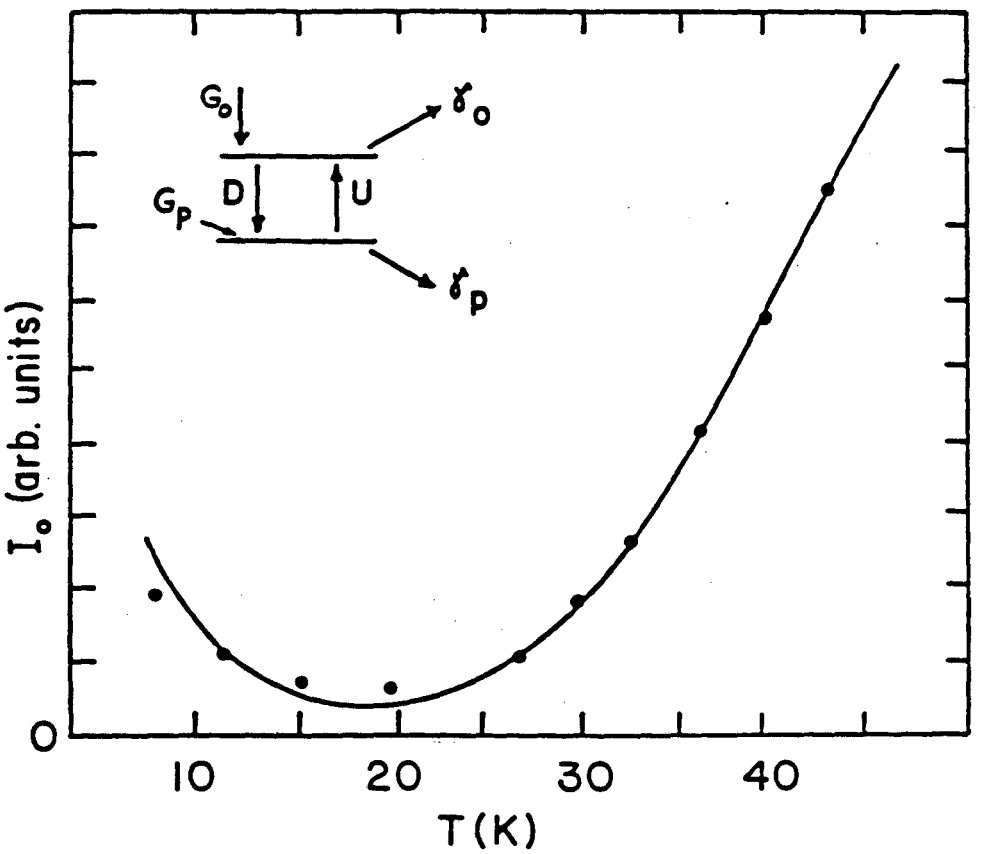

Figure 6.2

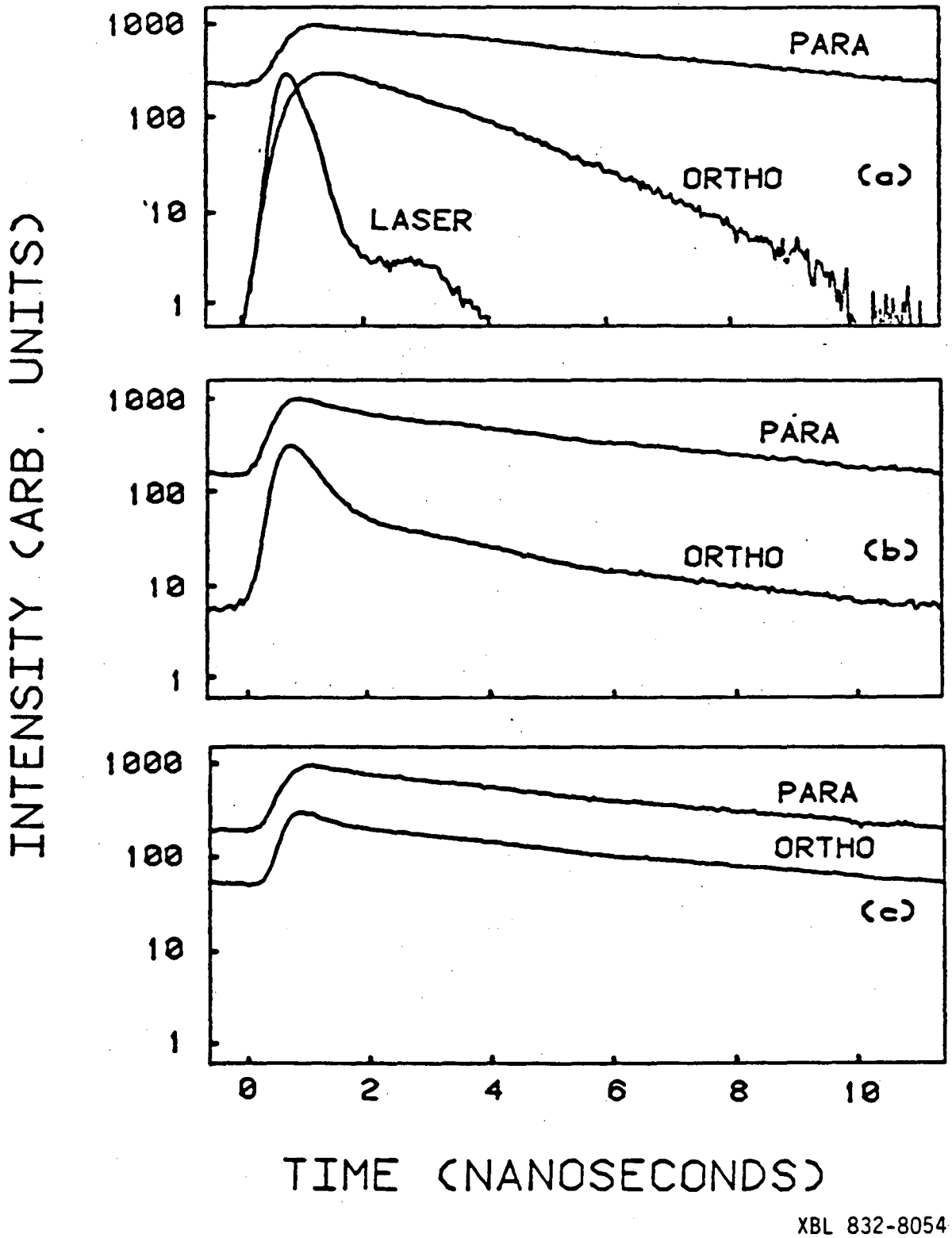
INTENSITY (ARB. UNITS)
1000
100
10
1
PARA
ORTHO
(a)
LASER
1000
100
10
1
PARA
ORTHO
(b)
1000
100
10
1
PARA
ORTHO
(c)
0
2
4
6
8
10
TIME (NANOSECONDS)
XBL 832-8054

Figure 6.3

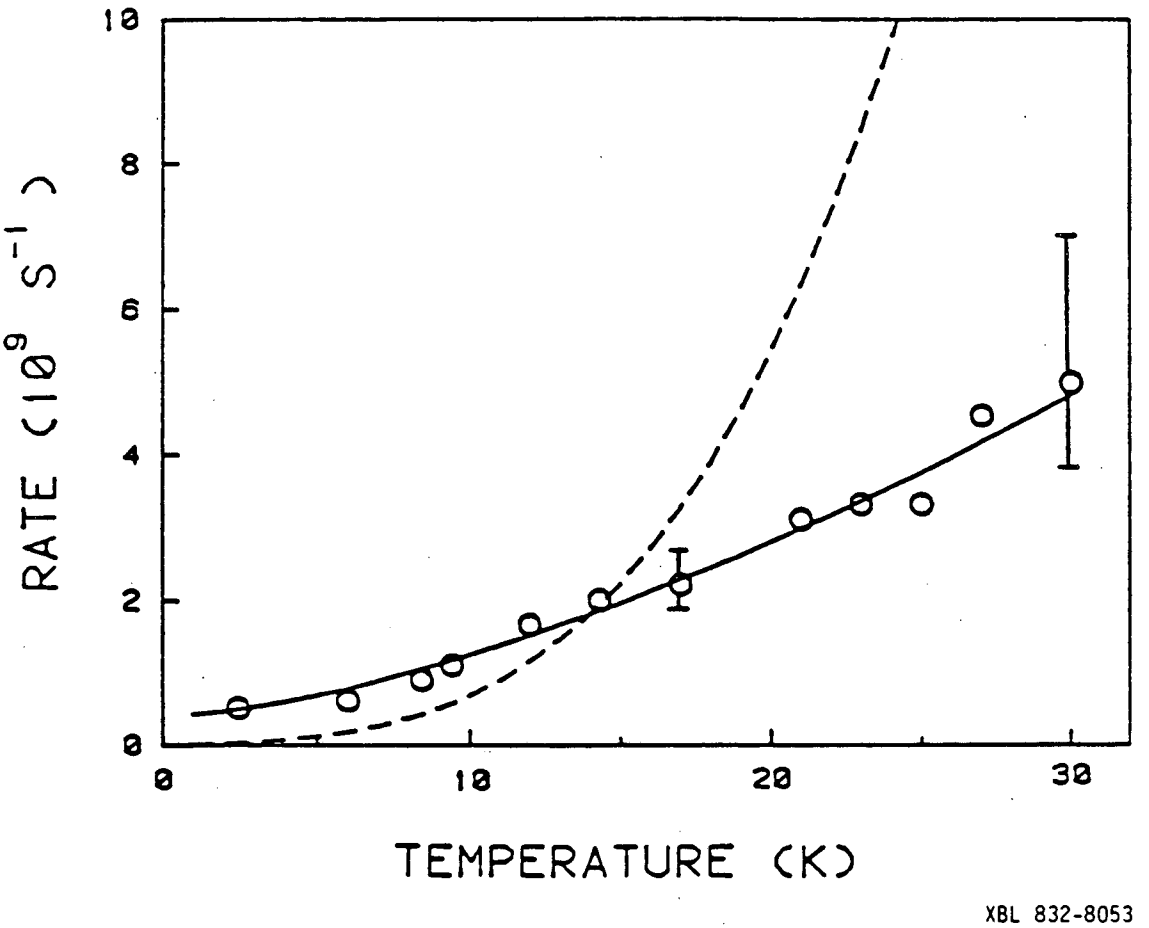

Figure 6.4

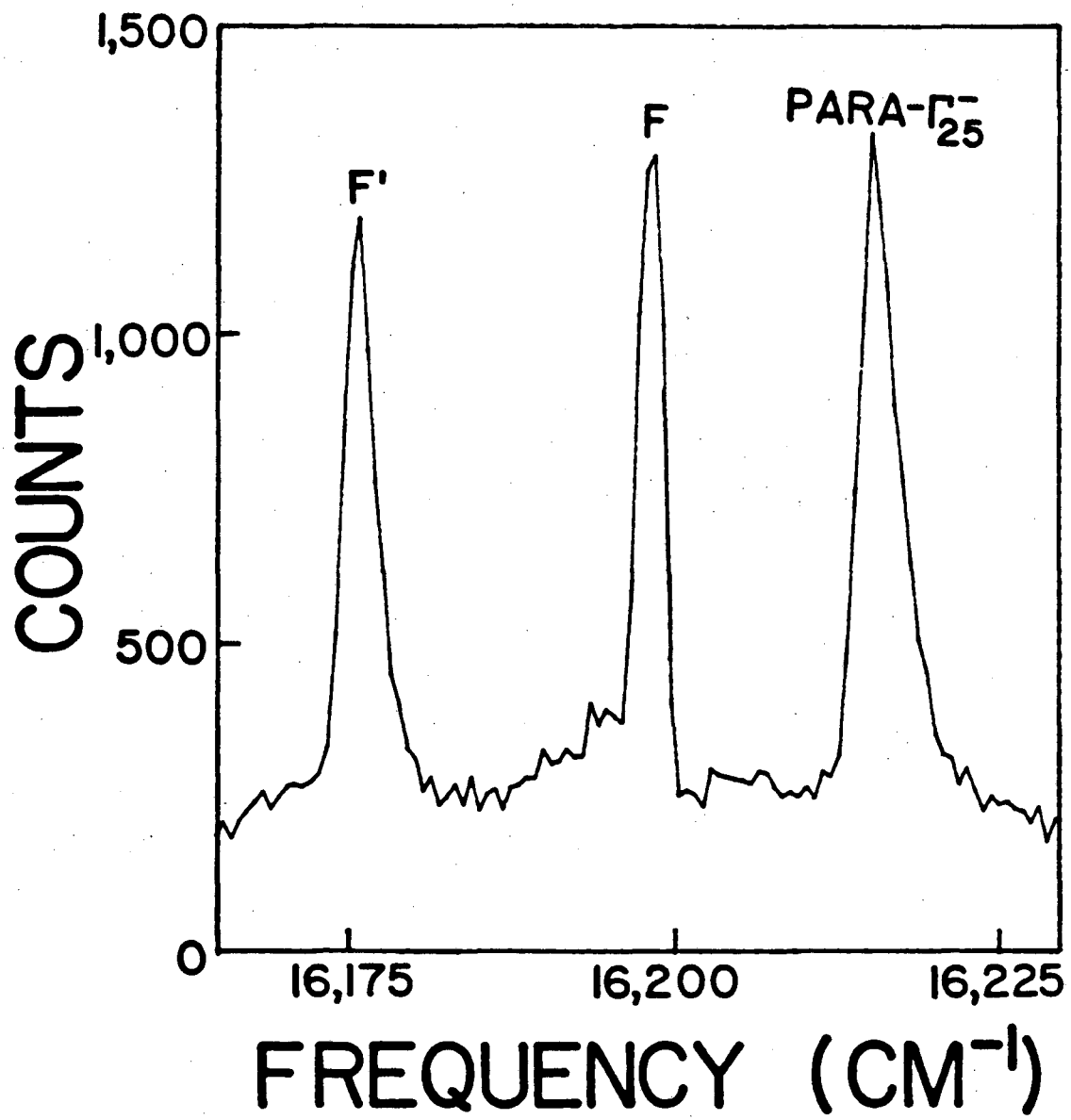
1,500
1,000
500
0
COUNTS
F'
F
PARA-Γ25⁻
16,175
16,200
16,225
FREQUENCY (CM⁻¹)

Figure 6.5

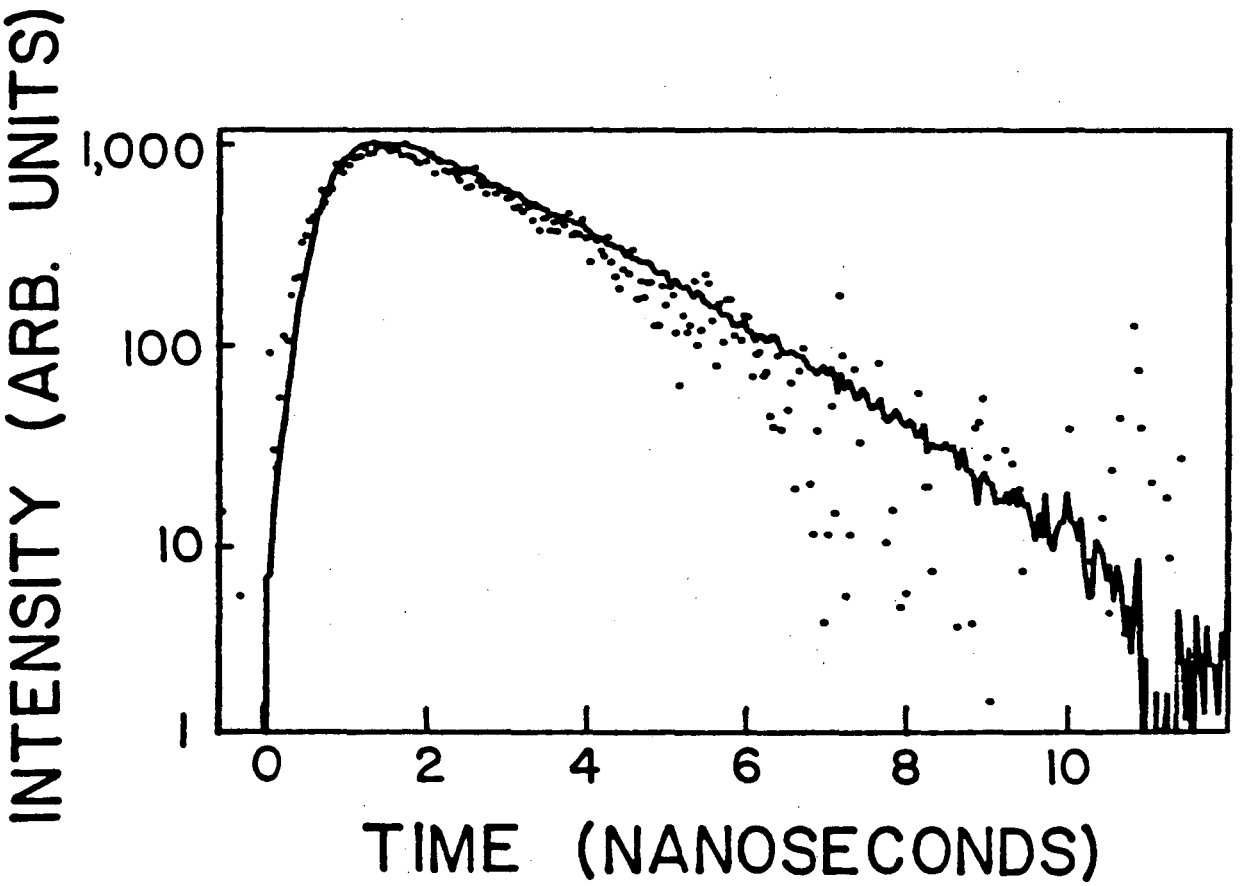

Figure 6.6

VII. TIME-RESOLVED HOT LUMINESCENCE AND RESONANT RAMAN SCATTERING

Resonant Raman Scattering (RRS) with tunable continuous wave (cw) lasers is a well established technique for studying electronic and vibrational excitations in various materials, ranging from semiconductors to hemoglobin.[1,2] It has been suggested that time-resolved RRS will give information about the dynamics of relaxation processes which are not provided by cw RRS measurements.[3] There has also been considerable debate in the literature[3-9] about whether RRS, a one-step coherent process, is distinguishable from hot luminescence (HL), a two-step absorption-emission process. It is now generally agreed that it is difficult to distinguish the two processes by cw experiments, but they can be readily distinguished by their temporal behavior after pulsed excitation.

Several different definitions of HL and RRS are in use, so in section A we will define what we mean by RRS and HL. The HL versus RRS controversy was triggered by a cw study of two-phonon Raman scattering in Cu_2O performed by Yu and Shen,[10] who found that the resonance enhancement of this mode was consistent with that expected for HL. We have measured the time-dependence of this mode in section B, and found that it is indeed dominated by HL. We also studied the time-dependence of one-phonon Raman scattering in Cu_2O. This mode is strongly polarized.[11] Our results, presented in section C, are consistent with HL. Our model explains the observed breakdown of the Raman selection rules at resonance. Breakdown in Raman selection rules in cw RRS has generally been attributed to wavevector dependent scattering.[12] By measuring the time-dependence of the complete one-phonon Raman lineshape

(in section D) we have been able to directly observe the thermalization of the intermediate state excitons and quantitatively explain our results using an extension of the theory developed in chapter V.

A. Definitions of Resonant Raman Scattering and Hot Luminescence

Some of the confusion in the debate over whether RRS and HL are equivalent is due to terminology. We will follow Shen's[5] definitions of HL and RRS. Raman scattering is a coherent process in which scattered photons are radiated by a polarization at frequency ω_s which has been induced in the medium by incident photons with frequency ω_i. When the incident radiation is turned off, the scattered radiation decays at the rate at which the phase coherence of the induced polarization disappears. This phase relaxation time is denoted by T_2. HL results from the radiative decay of the population in the intermediate state excited by the incident photons. HL will therefore decay with the population relaxation time T_1. Since T_2 depends both upon dephasing and population decay processes, T_2 is less than or equal to T_1. In principle, when $T_1 > T_2$, the two processes can be distinguished by their different temporal behavior.

B. Two-Phonon Resonant Raman Scattering in Cu_2O

The two-phonon resonant Raman scattering process in Cu_2O, as shown schematically in the inset of Figure 7.1 (a), involves excitation of ortho-excitons by phonon-assisted electric dipole transitions. Because of phonon participation, excitons with non-zero quasi-momentum can be excited. Their kinetic energy is given by $E = \hbar(\omega_i - \omega_{1S} - \omega_{12})$, where ω_{12} is the frequency of the dispersionless Γ_{12}^- phonon.

Figure 7.1 (a) shows the time-integrated two-phonon spectrum of our sample, which is similar to the cw spectra previously reported.[10] We note that the strengths of the Raman peaks are comparable to the background, so care must be used to determine their decay times.

Our $2\Gamma_{12}^-$ Raman mode is unpolarized so only the time-dependences of the $\hat{e}_i||\hat{e}_s$ component are shown in Figure 7.2. We expect the time-resolved RRS to show at most two decay times, corresponding to T_1 and T_2. We found that the curves in Figure 7.2 show one or two decay components depending on the ortho-exciton kinetic energy E. For curve (i) the Raman mode decays as e^{-t/T_1}, i.e., it is dominated by HL. For curves (ii) and (iii), however, there are two components to the decay. The slower component in both curves has time constant T_1 and its amplitude is consistent with its identification as the luminescence background. The faster component, with a decay time which depends on E, is identified with the $2\Gamma_{12}^-$ Raman peak. Based on this identification one can understand the variation in this fast decay time with E. We assume that the scattering is dominated by HL and the variation in the decay time reflects the dependence of the ortho-exciton lifetime on exciton energy. Yu and Shen[10] concluded from the cw two-phonon RRS in Cu_2O that for E greater than a few wavenumbers the ortho-exciton lifetime is limited by acoustic phonon scattering. Using the model and parameters presented in chapter V, we calculate the acoustic phonon scattering rates for E=4 and 7 cm^{-1} to be $(1.0\pm0.4)\times10^9 sec^{-1}$ and $(2.8\pm0.7)\times10^9 sec^{-1}$ respectively. These values are in fair agreement with the fast decay rates of $(1.8\pm0.6)\times10^9 sec^{-1}$ and $(3.3\pm1)\times10^9 sec^{-1}$ deduced from curves (ii) and (iii). For E = 1 cm^{-1}, however, the acoustic phonon scattering rate becomes too small to affect T_1, which

is then dominated by the ortho- to para-exciton conversion rate,[13] hence, in curve (i) both HL and the thermalized luminescence background will decay with time constant T_1. In summary, we have been able to resolve at most one decay component in the $2\Gamma_{12}^-$ Raman mode and the decay times we deduced are consistent with the energy dependent lifetimes of the exciton intermediate states.

C. One Phonon Resonant Raman Scattering in Cu_2O

One-phonon resonant Raman scattering in Cu_2O, as shown in the inset of Figure 7.1 (b), involves the excitation of zone center ortho-excitons by electric-quadrupole transitions and emission of photons via phonon-assisted electric-dipole transitions. The polarization selection rules for one-phonon RRS are unusual because the electric-quadrupole transition depends on the wavevector $\vec{k}_i$ of the incident photon.[14] The Raman tensors for different directions of $\vec{k}_i$ have been calculated by Birman.[15] For a backscattering geometry in which $\vec{k}||[101]$ the Γ_{12}^- mode is predicted to be nonzero only for incident polarization $\hat{e}_i||[010]$ and scattered polarization $\hat{e}_s||[101]$. Genack et al.[11] have studied the polarization selection rules for the Γ_{12}^- mode in this geometry. Although their results, shown as triangles in Figure 7.3 (b), agree qualitatively with the theory (shown as the broken curve in Figure 7.3 (b)), they also show appreciable intensity in the forbidden configuration. Genack et al attributed this 'forbidden' intensity to imperfections in the crystals.

1. Experimental Results

Our experiments were performed in a back-scattering geometry with a thin slice of melt-grown single crystal of Cu_2O at $2^\circ K$. We determined

the orientation of the sample by measuring the polarization of the ortho-exciton zero-phonon absorption and emission. These are unpolarized unless $\vec{k}$ lies along the [101] direction, in which case the absorption or emission is maximum when the radiation is polarized parallel to the [010] direction.[14] The electric-quadrupole absorption and emission in our sample show considerable polarization (shown as circles and triangles respectively in Figure 7.3 (a)), indicating that the sample surface is oriented close to but not exactly at the [101] direction. This was verified by the x-ray pictures of our sample.

Figure 7.1 (b) shows the time-integrated Γ_{12}^- spectrum of our Cu_2O sample. It is similar to the cw spectra reported previously.[11] The spectrum consists of a sharp Raman peak superimposed on a broader background due to thermalized luminescence.

We measured the polarization dependence of the one-phonon Raman mode at different locations on the sample using a focal spot of 100 μm diameter. We found that over most of the sample the one-phonon Raman line was unpolarized. At the same time we found that the polarization of electric-quadrupole absorption and emission was independent of the spot position, but the width of the absorption and emission lines was inversely correlated with the polarization of the Raman line. We believe therefore that the depolarization of the Raman mode is due to the presence of impurities or defects. For our study we focussed the laser on that portion of the sample which produced the narrowest electric-quadrupole absorption and emission linewidths and hence the most strongly polarized Raman modes.

The open circles in Figure 7.3 (b) represent the polarization dependence of the Γ_{12}^- Raman line in our sample. The incident

polarization was set for maximum electric-quadrupole absorption (near [010]). Our results qualitatively agree with those predicted for $\vec{k}||[101]$. The qualitative difference between our results and those of Reference 11 is presumably caused by the different quality of our sample and by the slight mis-orientation of our sample surface with respect to the [101] direction.

Figure 7.4 shows the time-dependence of the resonantly excited Γ_{12}^- Raman mode for two different polarization geometries: (i) incident laser polarization along the [010] direction while that of the scattered radiation is perpendicular to it ($\hat{e}_i \perp \hat{e}_s$); and (ii) ($\hat{e}_i || \hat{e}_s$).

According to the Raman selection rules calculated by Birman[15] the Γ_{12}^- mode is allowed in the $\hat{e}_i \perp \hat{e}_s$ geometry but forbidden in the $\hat{e}_i || \hat{e}_s$ geometry. As a result the intensity in the forbidden geometry can only result from HL and/or misorientation of the sample with respect to the [101] direction.

By deconvoluting curve (ii) in Figure 7.4 with the system response we found that the emission in the forbidden geometry decays as e^{-t/τ_a} where the decay time τ_a = 1.5 nsec is the same as the ortho-exciton population lifetime (T_1).[13] On the other hand, curve (i) in the allowed geometry can be fitted only by the sum of two exponentials: $ae^{-t/\tau_a} + be^{-t/\tau_b}$ where τ_a again equals 1.5 nsec and τ_b= 0.7 nsec. If we subtract curve (ii) from curve (i) then the resultant curve (iii) in Figure 7.4 represents the degree of polarization of the emission, which decays exponentially with time constant τ_b.

2. Theory and Comparison With Experiment

The decay curves in Figure 7.4 can be understood in terms of the

model shown in the inset. The triply degenerate Γ_{25}^{+} ortho-exciton states have been labelled XY, YZ and ZX, according to their symmetry. W represents the cross relaxation rate which equalizes the population in the three sublevels. If N_{xy}, N_{yz} and N_{zx} represent the population of levels XY, YZ and ZX respectively, then their time-dependence is determined by the rate equation:

$$\frac{dN_{xy}}{dt} = -(W+1/T_1)N_{xy} + WN_{yz} + WN_{zx} + G_{xy}(t) \qquad (7.1)$$

together with similar equations obtained by permuting the sets of indices. G_{xy}, G_{yz} and G_{zx} represent the generation rates for the three levels.

The initial population produced in the three levels can be determined from the electric-quadrupole selection rules.[14] The electric-quadrupole matrix elements are proportional to $(\hat{e}.\vec{r})(\vec{k}.\vec{r})$, where $\hat{e}$ and $\vec{k}$ are the polarization and wave vector respectively of the radiation. For $\vec{k}||[101]$ and $\hat{e}||[010]$ we find that the electric-quadrupole matrix element is proportional to xy+yz, so electric-quadrupole absorption populates states XY and YZ only. In a similar manner it can be shown that emission produced by the XY and YZ states via Γ_{12}^{-} phonon-assisted electric-dipole transitions is polarized with $\hat{e}_s||[101]$, therefore, emission in the forbidden geometry $\hat{e}_s||\hat{e}_i$ is entirely due to population transferred to ZX from XY and YZ during cross-relaxation and should be considered HL only. This interpretation is consistent with the result that the emission in the forbidden geometry decays with the population lifetime T_1. Solving Equations (7.1) and assuming that $G_{xy}(t)=G_{yz}(t)=\frac{N}{2}(t)$, where N is the total ortho-exciton population, we find:

$$N_{xy}(t)=N_{yz}(t)=\frac{Ne}{6}^{-(3W+1/T_1)t} + \frac{Ne}{3}^{-t/T_1} \quad (7.2)$$

$$N_{zx}(t)=\frac{N}{3}(-e^{-(3W+1/T_1)t} + e^{-t/T_1}) \quad (7.3)$$

From Equation (7.2) we expect that in the allowed geometry $\hat{e}_s \perp \hat{e}_i$ there can now be up to three decay components: (a) a RRS component with decay rate T_2^{-1} which is not contained in Equation (7.2); (b) a HL component with decay rate $3W+1/T_1$ due to both cross relaxation and total population decay; and (c) a HL component with decay rate T_1^{-1} due to the total population decay. Since $T_2^{-1} \geq 3W+1/T_1$ and we observe only two decay components in curve (i) we conclude that T_2 is dominated by cross relaxation or is too short to be observed. In both cases the 0.7 nsec. depolarization time we observe is due to cross relaxation.

Equation (7.3) predicts a risetime associated with the forbidden geometry $\hat{e}_s \| \hat{e}_i$, which is not evident in curve (ii). This is probably due to the misorientation of the sample resulting in some population being initially produced in the ZX state, obscuring the rise due to cross-relaxation.

Using the relation $1/\tau_b=(3W+1/T_1)$ we calculated $W=2.5\times10^8$ sec^{-1}. Our model also predicts the ratio of the HL intensities in the forbidden and allowed geometries to be $(1 + 1/(2WT_1)^{-1}=0.43$, and the polarization dependence of the Γ_{12}^- mode in our sample should follow the solid curve in Figure 7.3 (b). We note that this accounts for most of the 'breakdown' in the Raman selection rule that we observe. Whatever remaining discrepancies between the experimental points and the theory can probably be accounted for by the misorientation of the sample. From the width of the ortho-exciton absorption peak and our result we can set

limits on T_2 as 10 psec$<T_2\leq$0.7 nsec.—

D. Thermalization of A Nonequilibrium Exciton Population

In section B we have argued that for excitons with kinetic energy E $\leq$ 1 cm^{-1} the exciton-acoustic phonon scattering time is larger than the exciton lifetime of 1 nsec due to decay into the para-exciton. This suggests that the exciton luminescence should not have a thermalized linehape when it is resonantly excited. In this section we will present experimental results showing how this nonthermalized exciton population reaches equilibrium.

1. Theory

The exciton distribution function $\rho_k(E,t)$ is related to the luminescence lineshape by the relation:[16]

$$I(\omega_s) \propto g(E)\rho_k(E,t) \tag{7.4}$$

where $g(E)=E^{1/2}$ is the exciton density of states. We can write the following rate equation for $\rho_k(E,t)$:

$$\left(\frac{d\rho_k}{dt}\right) = \left(\frac{\partial\rho_k}{\partial t}\right)_{in} - \left(\frac{\partial\rho_k}{\partial t}\right)_{out} - \left(\frac{\partial\rho_k}{\partial t}\right)_{nr} + \left(\frac{\partial\rho_k}{\partial t}\right)_c \tag{7.5}$$

$\left(\frac{\partial\rho_k}{\partial t}\right)_{in}$ and $\left(\frac{\partial\rho_k}{\partial t}\right)_{out}$ are the rates at which excitons are scattered into and out of the state k by acoustic phonons, and are given by Equations (A.5) and (A.6) of the appendix. $\left(\frac{\partial\rho_k}{\partial t}\right)_{nr}$ is the non-radiative exciton decay rate due to ortho-para conversion, which has been measured to be 1.5 nsec in this sample. $\left(\frac{\partial\rho_k}{\partial t}\right)_c$ is the rate of exciton creation due to the laser pulses. Steady state solutions of this rate equation have already been presented in chapter V, however, here we will extend

our solution to the time-dependent domain.

In order to solve for $\rho_k(E,t)$ we assume that the exciton creation rate is given by:

$$\left(\frac{\partial \rho_k}{\partial t}\right)_c = \delta(t) e^{-E^2/A^2} \tag{7.6}$$

where A is the width of the zero-phonon absorption line, which we have measured to be 0.4 cm^{-1}.

Our model is depicted schematically in the inset of Figure 7.1(b). Excitons are directly created at k=0 by absorption. Those excitons which radiatively recombine without scattering produce the sharp peak at 16,288 cm^{-1}. The amplitude of this peak decays with time as the excitons either decay non-radiatively or are scattered by longitudinal acoustic phonons up to higher energy states. The slope of the acoustic phonon dispersion is much larger than that of the exciton dispersion near the bottom of the band due to the large effective mass of the ortho-exciton. As a result, excitons at k=0 can only be scattered by absorption of acoustic phonons of 5 cm^{-1} energy, resulting in the appearance of a broad peak at 16,293 cm^{-1}. At 2.5 °K, K_bT = 2 cm^{-1}, so the rate of this scattering process is slow. On the other hand, excitons with kinetic energy greater than 2.5 cm^{-1} can scatter by emission of acoustic phonons, which will occur much faster. As Askary[17] has pointed out, the faster of the two processes will determine the risetime of the peak at 16,293 cm^{-1}, while the slower process will limit the rate at which equilibrium is reached.

Equations (7.5) and (7.6) were numerically solved for $\rho_k(E,t)$ using an iterative procedure. The material parameters were taken from chapter V. The only other parameters involved in the calculation were the

lattice temperature and the width of the zero-phonon ortho-exciton absorption line, which were obtained experimentally. Equation (7.4) was used to determine the luminescence lineshape. For comparison with our experimental data, the resulting points were convoluted with gaussian functions in frequency and time whose widths were chosen to be 1 cm^{-1} and 500 psec respectively, to correspond to the experimental values. Also, in order to simulate the fact that the experimental laser pulses have a repetition rate of 80 Mhz a replica of the theoretical points was delayed by 12.5 nsec and added to the original points. The resulting theoretical spectra are shown as three-dimensional plots in Figure 7.5 (c) and (d).

2. Experiment

The experimental time-dependent Γ_{12}^{-} phonon-assisted luminescence spectra at 2.5 °K are shown in Figure 7.5 (a) and (b). They were reconstructed from the luminescence decay curves measured at frequency intervals of 1 cm^{-1} using the time-integrated luminescence intensity for normalization. Since the time-decay spectra werenot deconvoluted, the temporal resolution is limited by the 500 psec FWHM of the instrument response. Initially, the spectrum consists of a sharp line at 16,288 cm^{-1} corresponding to recombination of the initial exciton population at k=0. This population appears to relax by a two step process: (i) within 0.5 nsec a peak appears 5 cm^{-1} above the bottom of the band. The maximum amplitude of this peak is about 5 % of that of the k=0 peak; (ii) subsequently, the amplitudes of both peaks decay, until after 5 nsec the spectrum has approximately reached a constant shape.

The theoretical curves in Figure 7.5 (c) and (d) clearly reproduce all of the features of the experimental spectrum, including the position, width and amplitude of the high energy peak, and, the time needed to reach a steady state distribution. Also, by comparing Figure 7.5 (b) and (d) we see that the theory also correctly predicts the risetime of the high energy peak. This good agreement between our model and the experimental result provides strong support to our interpretation of the time dependent emission spectra in Cu_2O.

E. Conclusions

We have found that HL provides a self-consistent interpretation of all the CW and time-resolved measurements of both one-phonon and two-phonon resonant Raman scattering in Cu_2O, including scattering previously assigned to breakdown in Raman selection rules. We have shown that time-dependent emission measurements can determine the intraband scattering rates due to acoustic phonons and crossing relaxation between degenerate sublevels in the case of Cu_2O. These rates cannot be determined directly by CW measurements. Thus time-dependent scattering measurement provides not only insight into the physical mechanisms of light scattering processes, but is also a valuable tool in studying the dynamics of electrons in condensed matter.

REFERENCES

1. See for example, Light Scattering in Solids, ed. by M. Cardona, Topics in Applied Physics, vol. 8 (Springer-Verlag, New York, 1975).
2. See for example, Vibrational Spectra and Structure, vol. 5, ed. by J. R. Durig (Elsevier, Amsterdam, 1976).
3. T. Takagahara, Relaxation of Elementary Excitations, ed. by R. Kubo and E. Hanamura, Solid State Sciences 18 (Springer-Verlag, New York, 1980), p. 45.
4. M. V. Klein, Phys. Rev. B 8, 919 (1973).
5. Y. R. Shen, Phys. Rev. B 9, 622 (1974).
6. P. Saari, in Light Scattering in Solids, ed. J. L. Birman, H. Z. Cummins and K. K. Rebane (Plenum, New York, 1979), p. 315.
8. P. F. Williams, D. L. Rousseau and S. H. Dworetsky, Phys. Rev. Lett. 32, 196 (1974).
9. Y. Masumoto, S. Shionoya and Y. Tanaka, Solid State Commun. 27, 1117 (1978).
10. P. Y. Yu and Y. R. Shen, Phys. Rev. B 12, 1377 (1975).
11. A. Z. Genack, H. Z. Cummins, M. A. Washington and A. Compaan, Phys. Rev. B 12, 2478 (1975); A. Compaan and H. Z. Cummins, Phys. Rev. Lett. 31, 41 (1973).
12. See R. M. Martin and L. M. Falicov; in Reference 1, p. 80.
13. J. S. Weiner, N. Caswell, P. Y. Yu and A. Mysyrowicz, Solid State Commun., 46, 105 (1983).
14. R. J. Elliot, Phys. Rev. 124, 340 (1961).
15. J. L. Birman, Phys. Rev. B 9, 4518 (1974).

16. Y. Petroff, P. Y. Yu and Y. R. Shen, Phys. Rev. B 12, 2488 (1975).

17. F. Askary and P. Y. Yu, Phys. Rev B 28, 6165 (1983).

FIGURE CAPTIONS

Figure 7.1 Time-integrated Raman spectra of Cu_2O at $2^{\circ}K$. The dotted line represents the thermalized luminescence background. (a) One-phonon Raman spectrum. (b) Two-phonon Raman spectrum for E=4 cm^{-1}. The insets in (a) and (b) are respectively the schematic diagrams of one-phonon and two-phonon Raman scattering processes discussed in the text.

Figure 7.2 Time-dependence of two-phonon RRS in Cu_2O for incident laser frequencies corresponding to $E=\hbar(\omega_1-\omega_o-\omega_{12})$ equal to (i) 1 cm^{-1}, (ii) 4 cm^{-1} and (iii) 7 cm^{-1} respectively. The dotted curve superimposed on (iii) represents a typical fit to the experimental curves by convolution of the system response with a decay function of the form: $\left(0.126e^{-t/1.5\ \text{nsec}} + e^{-t/0.26\ \text{nsec}}\right)$.

Figure 7.3 Polarization dependence measurements in Cu_2O. (a) EQ absorption (circles) and emission (triangles) plotted as a function of the angle between the polarization and the [010] direction. (b) One-phonon Raman intensity for $\hat{e}_i \| [010]$, plotted as a function of the angle between the scattered polarization $\hat{e}_s$ and the [010] direction. The circles represent our experimental results. The triangles represent data from Reference 11. The broken and solid curves represent the predictions of Reference 15 and of the theory described in the text respectively.

Figure 7.4 Time-dependence of one-phonon Raman scattering in Cu_2O.

The scattering configurations were: (i) $(\hat{e}_s \perp \hat{e}_i)$ and (ii) $(\hat{e}_s \| \hat{e}_i)$. Curve (iii) was obtained by taking the difference between curves (i) and (ii). Curve (iv) represents the system's response to a 10 psec long dye laser pulse. The inset represents the three-level model discussed in the text.

Figure 7.5 Lineshape of the Γ_{12}^{-} phonon-assisted ortho-exciton luminescence as a function of time at a temperature of 2.5°K. (a) and (b) show the measured lineshapes. The experimental points are spaced at intervals of 1 cm^{-1}. (c) and (d) show the corresponding lineshapes calculated using the model described in the text.

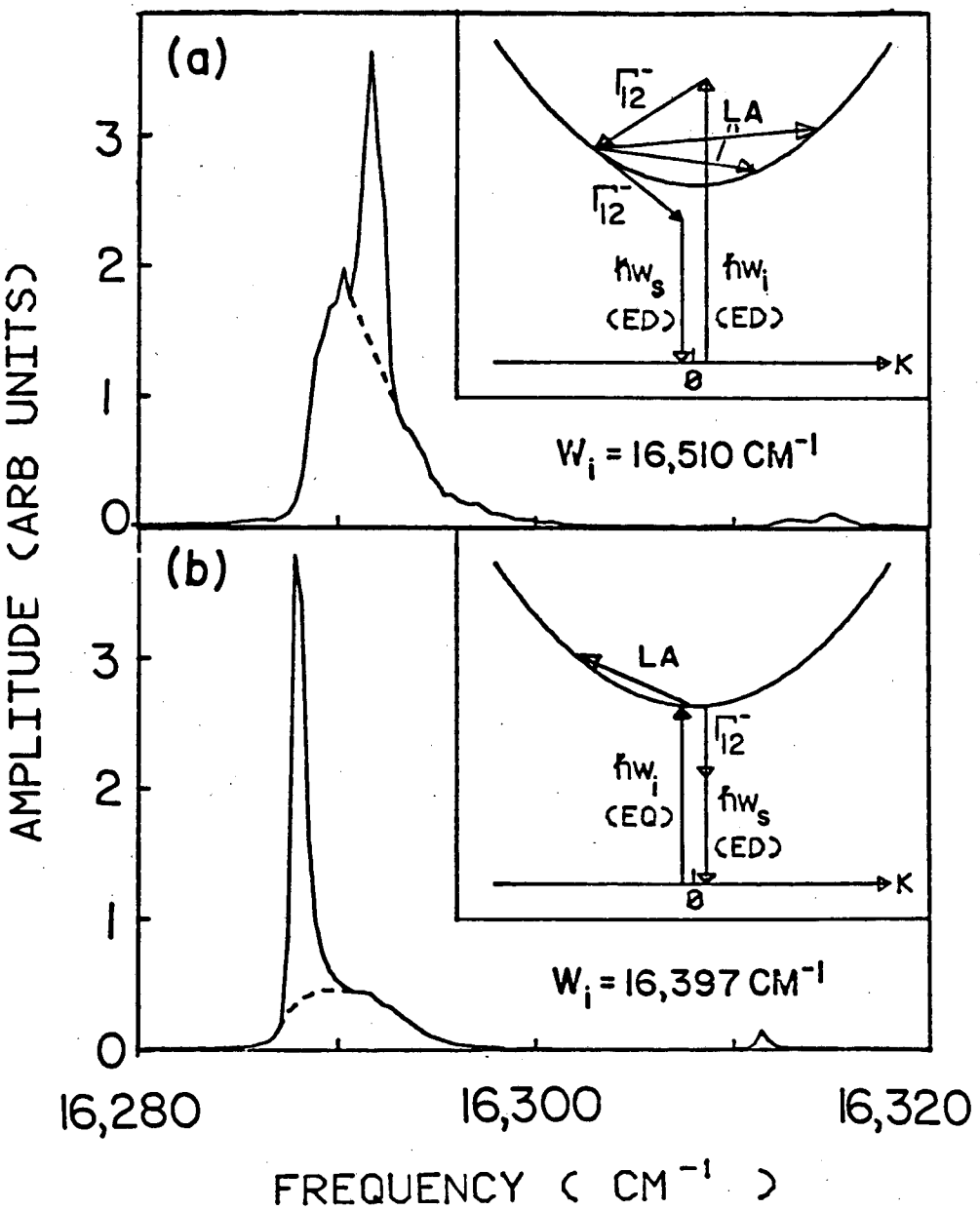
(a)
(b)
AMPLITUDE (ARB UNITS)
0
1
2
3
16,280
16,300
16,320
FREQUENCY (CM⁻¹)
Γ12⁻
LA
ħws
(ED)
ħwi
(ED)
K
0
Wi = 16,510 CM⁻¹
ħwi
(EQ)
ħws
(ED)
Wi = 16,397 CM⁻¹

Figure 7.1

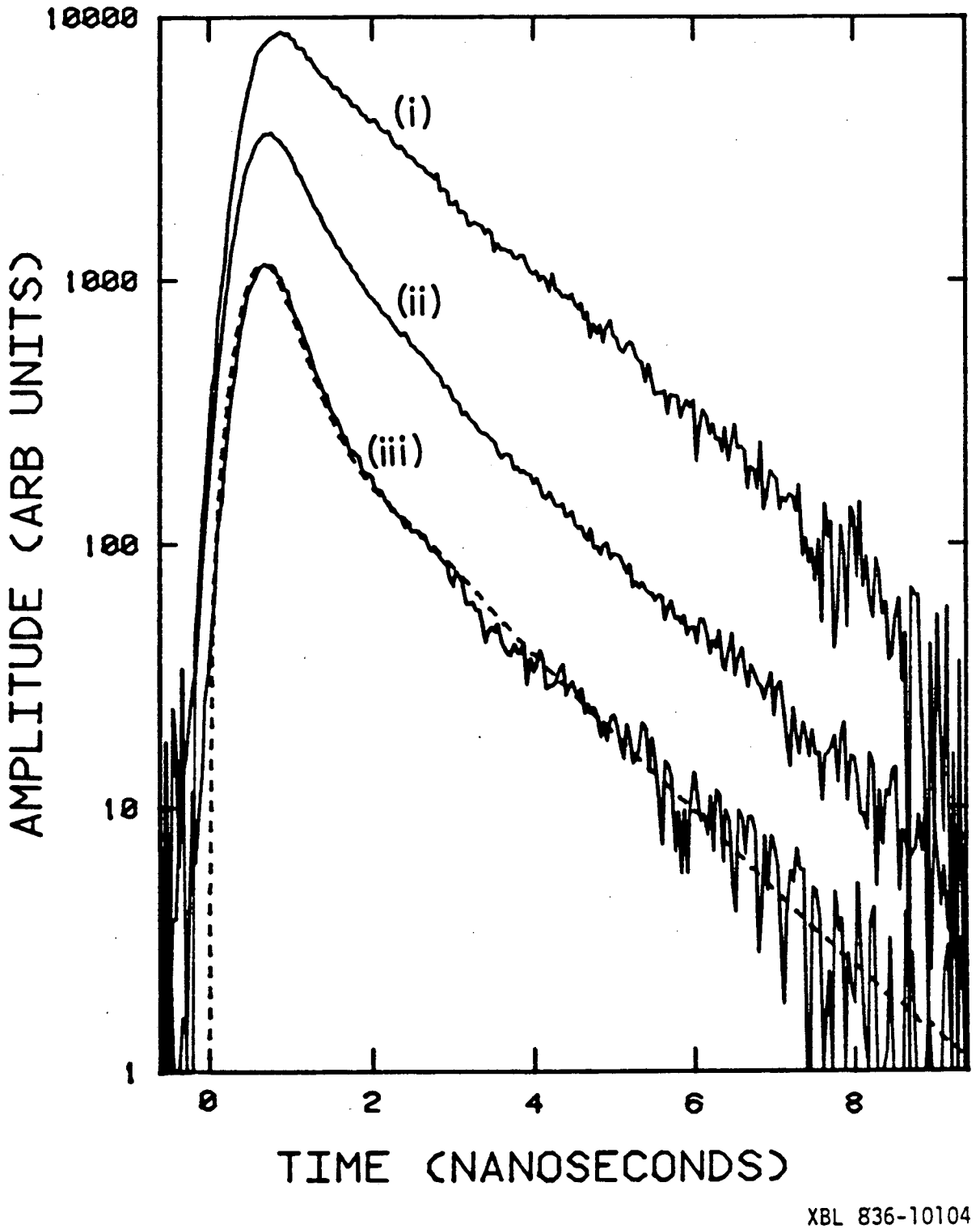
10000
1000
100
10
1
AMPLITUDE (ARB UNITS)
(i)
(ii)
(iii)
0
2
4
6
8
TIME (NANOSECONDS)
XBL 836-10104

Figure 7.2

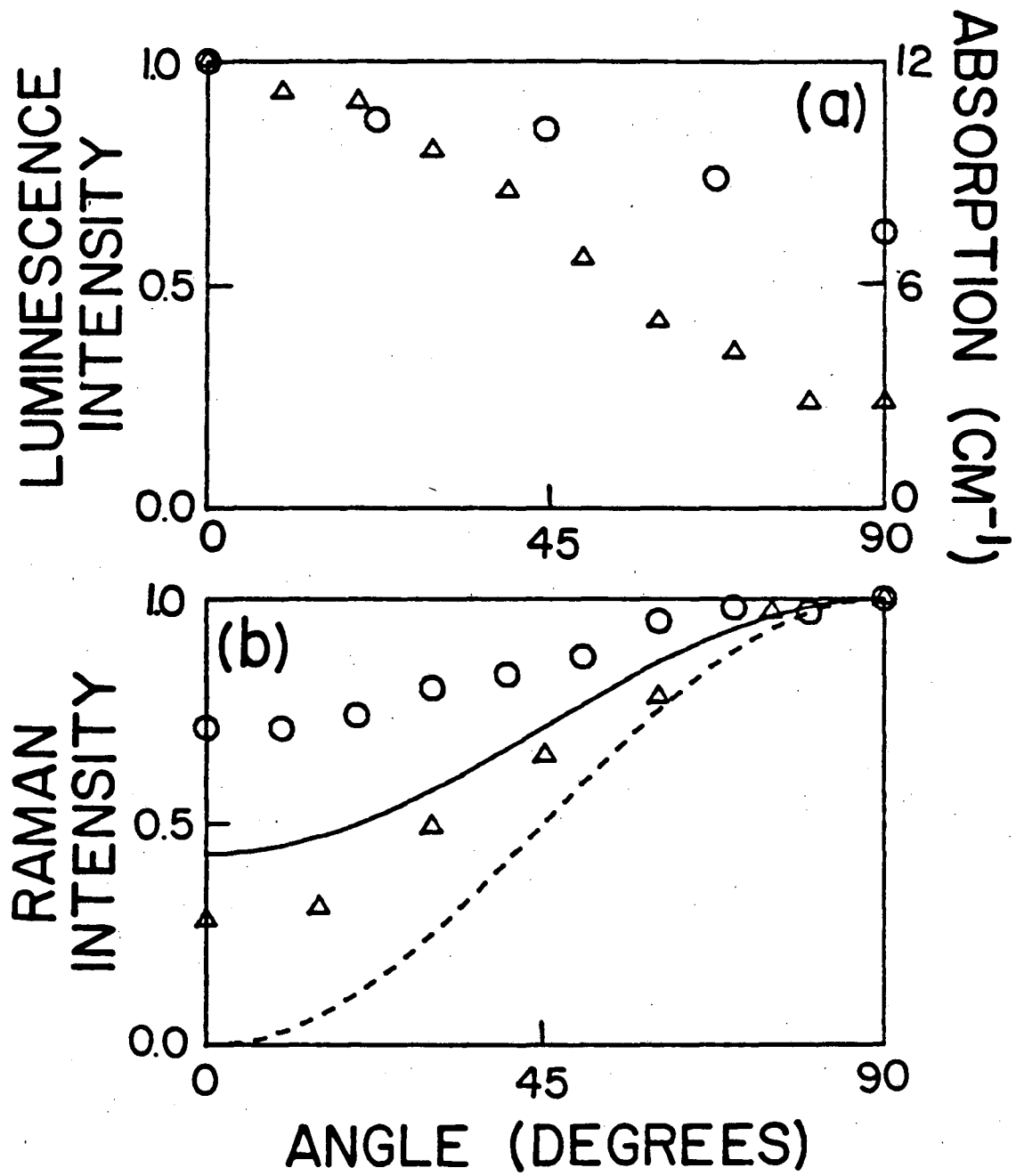
LUMINESCENCE INTENSITY
ABSORPTION (CM⁻¹)
(a)
1.0
0.5
0.0
12
6
0
0
45
90
(b)
RAMAN INTENSITY
1.0
0.5
0.0
0
45
90
ANGLE (DEGREES)

Figure 7.3

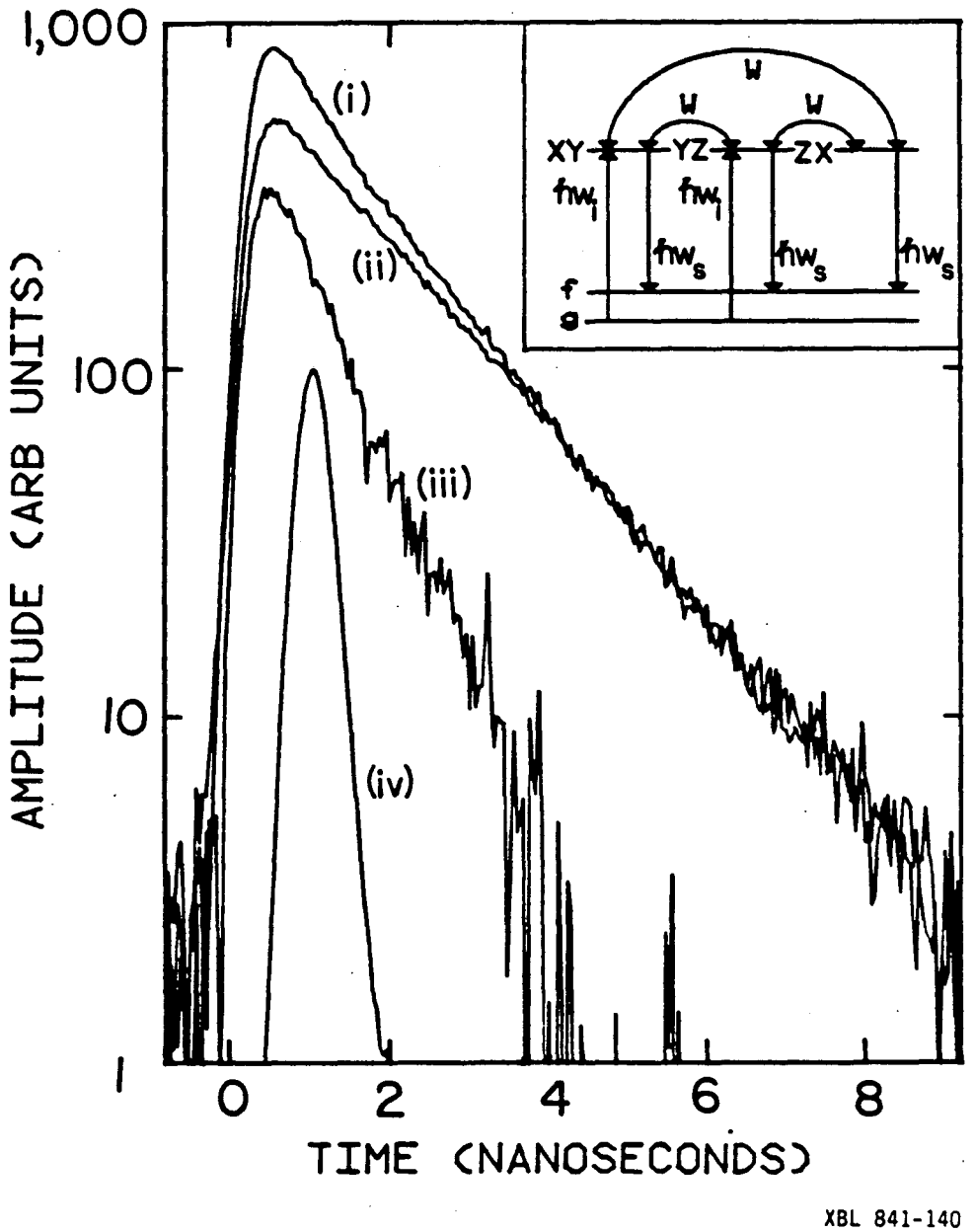
1,000
100
10
1
AMPLITUDE (ARB UNITS)
0
2
4
6
8
TIME (NANOSECONDS)
(i)
(ii)
(iii)
(iv)
W
W
W
XY
YZ
ZX
fw_f
fw_f
fw_s
fw_s
fw_s
f
g
XBL 841-140

Figure 7.4

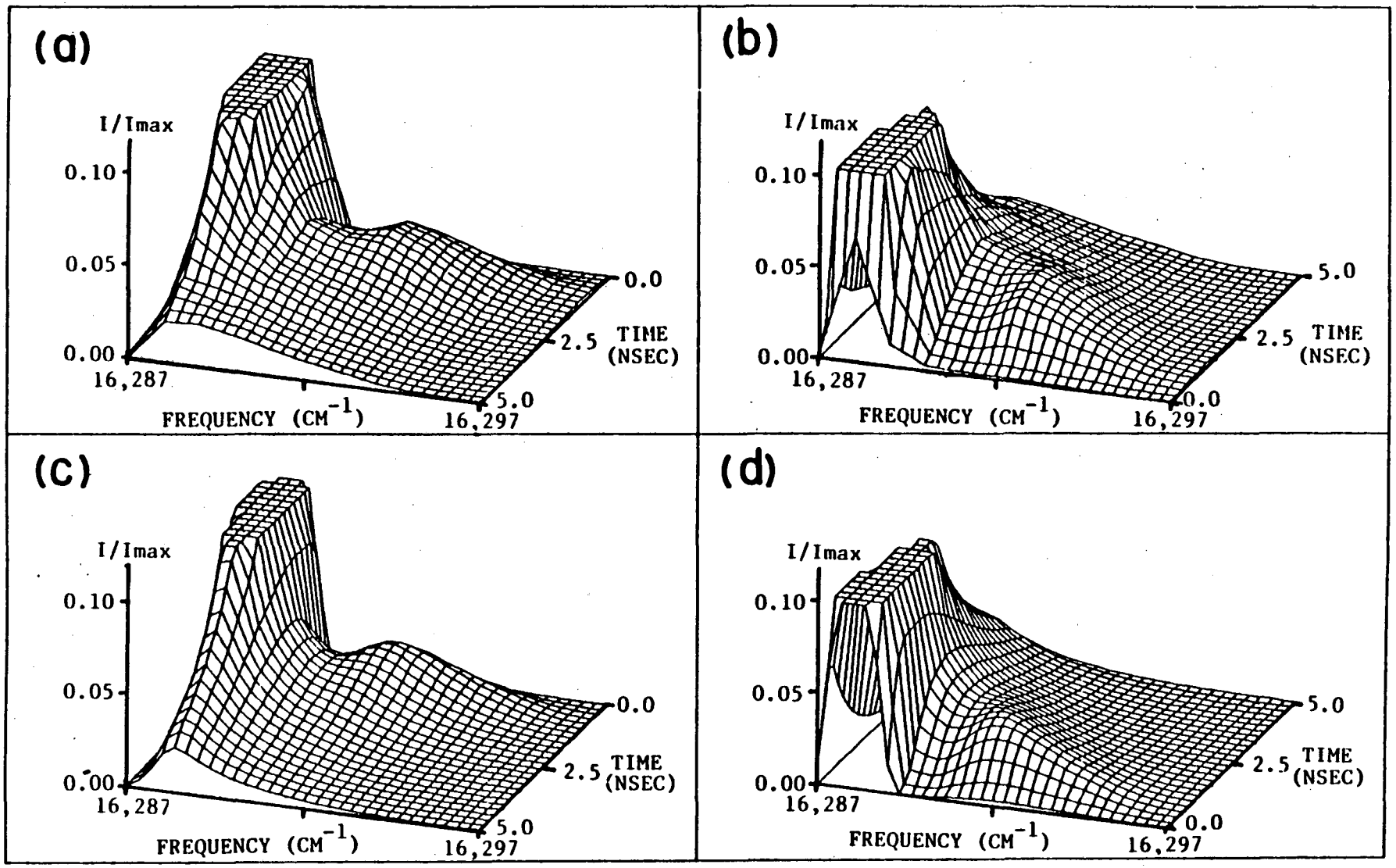

Figure 7.5

XBL 841-139

VIII. CONCLUSIONS

We have presented a series of studies of the dynamics of carrier relaxation in semiconductors. In GaAs we found that the large dynamic range of our time-delayed coincidence photon counting system allowed us to determine that the free carrier lifetime was dominated by bulk recombination.

We have been able to answer a number of questions concerning excitons in Cu_2O. We have been able to measure the lifetime of the ortho-exciton for the first time, and, by studying its temperature dependence have shown that the primary ortho-exciton decay channel is through conversion into the para-exciton.

We have quantitatively explained the nonthermalized luminescence spectra of certain Cu_2O samples by means of a model based on the scattering of the excitons by acoustic phonons. This model has only one adjustable parameter consisting of the exciton non-radiative lifetime and explains the lineshape of some resonant Raman peaks better than previous theories.

Our most important findings are on the nature of resonant light scattering in Cu_2O. We have found that hot luminescence provides a self-consistent explanation of all of the steady state and time-resolved measurements, and provides an explanation for the previously observed breakdown in the 'Raman' selection rules. More generally, we have shown that from time-dependent measurements it is possible to deduce information which is not available from cw measurements. For the case of Cu_2O, we have determined the cross relaxation rate, and, the intraband acoustic phonon scattering rate as a function of exciton kinetic energy.

This technique, we believe, is applicable to many materials besides Cu_2O.

APPENDIX. Derivation of the Exciton-Acoustic Phonon Scattering Rate

In this appendix we derive expressions for the exciton-acoustic phonon scattering rate in Cu_2O. We make the following assumptions, which are based on previous optical results:[1,2]

(i) The kinetic energy of the yellow ortho-exciton is given by $E = \hbar k^2/2m$ where m is its effective mass.

(ii) The scattering of excitons by transverse acoustic (TA) phonons is negligible compared to scattering by longitudinal acoustic (LA) phonons. This can be understood in the following way. An acoustic wave propagating through a crystal will cause the atoms to oscillate about their equilibrium positions. The resultant changes in lattice spacing will cause a perturbation in the energies of the valence and conduction bands which can scatter an exciton. However, a TA phonon produces a transverse strain in the crystal, which is to lowest order equivalent to a simple rotation of the crystal with no change in lattice spacing. Therefore, scattering of excitons by TA phonons is weak compared to scattering by LA phonons.

(iii) The LA phonon dispersion is isotropic and is given by $\omega_{LA} = vq$ where v is the LA phonon velocity and q is the magnitude of the phonon wavevector.

The matrix element for the exciton-LA phonon interaction has been derived by Toyazawa[3], and simplified for the case of Cu_2O by Yu and Shen.[1] The matrix element for scattering of an exciton with wavevector k by a phonon of wavevector q is given by:

$$H_{\vec{k}\pm\vec{q},\vec{k}} = gq^{1/2}(N_q + 0.5 \pm 0.5)^{1/2} \qquad (A.1)$$

where $g = (\hbar/(2r_1Vv))^{1/2} \times E_{ac}$. The upper and lower signs refer to scattering via absorption and emission of a phonon respectively. $N_q = (e^{\hbar vq/K_bT} - 1)^{-1}$ is the phonon occupation number; $r_1 = 6$ gm cm^{-3} is the density of Cu_2O; V is the volume of the crystal; $E_{ac} = 2/3 \times (C_c - C_v)$ is the acoustic phonon deformation potential. The right hand side of this last expression represents the notation originally used by Toyazawa.

From perturbation theory it can be shown that the rate at which excitons are scattered out of a state k by acoustic phonons is given by;

$$\left(\frac{\partial \rho_k(E)}{\partial t}\right)_{out} = \frac{2\pi}{\hbar}\sum_{\vec{q}}\left|H_{\vec{k}-\vec{q},\vec{k}}\right|^2\delta\left(\frac{\hbar}{2m}(|\vec{k}|^2-|\vec{k}-\vec{q}|^2)-vq\hbar\right)\rho_k(E) + \frac{2\pi}{\hbar}\sum_{\vec{q}}\left|H_{\vec{k}+\vec{q},\vec{k}}\right|^2\delta\left(\frac{\hbar}{2m}(|\vec{k}|^2-|\vec{k}+\vec{q}|^2)+vq\hbar\right)\rho_k(E) \qquad (A.2)$$

The two terms correspond to emission and absorption, respectively, of acoustic phonons. The summations are straightforward but tedious, and, have been described in detail in the books by Conwell[4] and Seeger,[5] so we will merely state the final expression, which is:

$$\left(\frac{\partial \rho_k(E)}{\partial t}\right)_{out} = \frac{mE_{ac}^2\rho_k(E)}{4\pi\hbar^2 r_1 vk}\left\{\int_{-2k+\frac{2mv}{\hbar}}^{2k+\frac{2mv}{\hbar}} N_q q\, dq + \int_0^{2k-\frac{2mv}{\hbar}} (N_q+1) q\, dq\right\} \qquad (A.3)$$

Similarly, the rate at which excitons are scattered into the state k by LA phonons is given by:

$$\left(\frac{\partial \rho_k(E)}{\partial t}\right)_{in} = \frac{mE_{ac}^2}{4\pi\hbar^2 r_1 vk}\left\{\int_0^{2k-\frac{2mv}{\hbar}} N_q q^2 \rho_{|\vec{k}+\vec{q}|}(E+vq\hbar)dq + \int_{-2k+\frac{2mv}{\hbar}}^{2k+\frac{2mv}{\hbar}} (N_q+1)q^2 \rho_{|\vec{k}-\vec{q}|}(E-vq\hbar)dq\right\} \tag{A.4}$$

Since q is a magnitude it cannot be negative, therefore, in equations (A.3) and (A.4) when a limit of an integral is less than zero, it must be replaced by zero. For instance, the second term in equation (A.3), which corresponds to scattering by emission of an acoustic phonon, will disappear for $k<mv/\hbar$. The physical explanation for this is that, for $k<mv/\hbar$ the slope of the LA phonon dispersion is steeper than that of the exciton dispersion, so momentum cannot be conserved and phonon emission is not allowed.

In order to convert to units of energy we make the following substitutions: $\varepsilon = \hbar vq$ $E = \hbar^2k^2/2m$. The rates take the form:

$$\left(\frac{\partial \rho_k(E)}{\partial t}\right)_{out} = \frac{m^{5/2}E_{ac}^2 \rho_k(E)}{\sqrt{2}\pi\hbar^4 r_1 d^2 E^{\frac{1}{2}}}\left[\int_{c-d}^{c+d} N(\varepsilon)\varepsilon^2 d\varepsilon + \int_0^{c-d} [N(\varepsilon)+1]\varepsilon^2 d\varepsilon\right] \tag{A.5}$$

$$\left(\frac{\partial \rho_k(E)}{\partial t}\right)_{in} = \frac{m^{5/2}E_{ac}^2}{\sqrt{2}\pi\hbar^4 r_1 d^2 E^{\frac{1}{2}}}\left[\int_0^{c-d} N(\varepsilon)\varepsilon^2 \rho_{|\vec{k}+\vec{q}|}(E+\varepsilon)d\varepsilon + \int_{-c-d}^{c+d} [N(\varepsilon)+1]\varepsilon^2 \rho_{|\vec{k}-\vec{q}|}(E-\varepsilon)d\varepsilon\right] \tag{A.6}$$

Where $c = \frac{2(Ed)^{\frac{1}{2}}}{\hbar}$ and $d = 2mv^2$.

REFERENCES

1. P.Y. Yu and Y.R. Shen, Phys. Rev. B 12, 1377 (1975).

2. See S. Nikitine, in Optical Properties of Solids, edited by S. Nudelman and S. S. Mitra (Plenum, New York, 1969).

3. Y. Toyazawa, Prog. Theor. Phys. 20, 53 (1958).

4. E. M. Conwell, Solid State Physics, Suppl. 9, edited by F. Seitz, D. Turnbull, and H. Ehrenreich (Academic Press, New York, 1967).

5. K. Seeger, Semiconductor Physics (Springer-Verlag, New York, 1973).

This report was done with support from the Department of Energy. Any conclusions or opinions expressed in this report represent solely those of the author(s) and not necessarily those of The Regents of the University of California, the Lawrence Berkeley Laboratory or the Department of Energy.

Reference to a company or product name does not imply approval or recommendation of the product by the University of California or the U.S. Department of Energy to the exclusion of others that may be suitable.

TECHNICAL INFORMATION DEPARTMENT
LAWRENCE BERKELEY LABORATORY
UNIVERSITY OF CALIFORNIA
BERKELEY, CALIFORNIA 94720